

https://dspace.org/

Processing and inferential methods to improve shaft-voltage-based condition monitoring of synchronous generators

Doorsamy, Wesley

2015-03-25
http://hdl.handle.net/10539/18564

Downloaded from a DSpace repository. https://dspace.org/

Processing and inferential methods to improve shaft-voltage-based condition monitoring of synchronous generators

Wesley Doorsamy

A thesis submitted to the Faculty of Engineering and the Built Environment, University of the Witwatersrand, Johannesburg, in fulfilment of the requirements for the degree of Doctor of Philosophy.

Johannesburg, 2015

Declaration

I declare that this thesis is my own, unaided work, other than where specifically acknowledged. It is being submitted for the degree of Doctor of Philosophy in the University of the Witwatersrand, Johannesburg. It has not been submitted before for any degree or examination in any other university.

Signed this _____ day of _____ 20 _____

_____

Wesley Doorsamy

Abstract

This thesis focuses on improving shaft-voltage-based condition monitoring of synchronous generators. The work presents theory for describing and modelling shaft voltages using fundamental electromagnetic principles. A modern framework is adopted in developing an online, automated and intelligent fault-diagnosis system. Novel processing and inferential methods are used by the system to provide accurate and reliable incipient-fault detection and diagnosis. The literature shows that shaft-voltage analysis is recognised as a technique with potential for use in condition monitoring. However, deficiencies in the fundamental theory and the inadequacy of methods for extracting useful information has limited its widespread application. This work extends the knowledge of shaft voltages, validates the merits of its use for fault diagnosis, and provides methods for practical application. Validation of the model is completed using an experimental synchronous generator, and results indicate that simulated shaft voltages compare well with the measurements - i.e. total average error of the model combined with experimental uncertainty is below 16%. The fault detection and diagnosis components are tested separately and together as a complete shaft-voltage-based condition-monitoring system in an experimental setting. Results indicate that the system can accurately diagnose faults and it represents a unique and valuable contribution to shaft-voltage-based condition monitoring. Additionally, techniques such as optimal measurement selection, multivariate model monitoring, and fault inference developed for the investigations and system presented in this thesis, will assist engineers and researchers working in the field of condition monitoring of electrical rotating machines.

To my Higher Power,

thank you for your gracious will.

Acknowledgements

I thank the staff of the School of Electrical and Information Engineering. I hereby acknowledge the financial support of the National Research Foundation of South Africa.

I would like to express my sincere thanks to my supervisor, Prof Willie Cronje, for his patience, guidance and willingness. I would like to thank Dr Ahmed Abdallh, Ghent University, for sharing his valuable knowledge of estimation theory and electromagnetics. I would also like to thank Dr Christian Röver, Universitätsmedizin Göttingen, for sharing his insght on Bayesian spectrum estimation.

Finally, I am very grateful to my wife, Lorinda. Her continuous support and encouragement made this work possible.

List of Publications

The author has contributed to the following publications, during candidature, with the conceptualisation of the ideas, data collection, analysis, design, and lead writing. The co-authors are acknowledged for contributing to the analysis and review of the work. Further acknowledgement is given to Dr Ahmed Abdallh, specifically for his assistance with the design of the CRLB-based technique for selection of optimal measurement modality. In reference to the parts of the copyrighted materials listed below which are used in this thesis, the applicable organisations do not endorse any of University of the Witwatersrand's products or services. Internal or personal use of this material is permitted.

1. W. Doorsamy, and W. A. Cronje, "A review of condition monitoring techniques and typical failure modes with regards to large rotating electrical machines", *South African Universities Power Engineering Conference, Potchefstroom*, South Africa, pp. 86 - 91, 2013.

2. W. Doorsamy, and W. A. Cronje, "Interpretation and significance of shaft voltages in rotating electrical machines", *South African Universities Power Engineering Conference*, Durban, South Africa, pp. 226 - 230, 2014.

3. W. Doorsamy, and W. A. Cronje,"A study on Bayesian spectrum estimation based diagnostics in electrical rotating machines", *IEEE International Conference on Industrial Technology*, Busan, South Korea, pp. 636 - 640, 2014.

4. W. Doorsamy, and W. A. Cronje, "An electromagnetic model for shaft voltages in synchronous generators", *IEEE International Conference on Industrial Technology, Busan, South Korea*, pp. 149 - 154, 2014.

5. W. Doorsamy, and W. A. Cronje, "Optimisation of shaft voltage based condition monitoring in generators using a Bayesian approach", *IET Power Electronics Machines and Drives*, Manchester, United Kingdom, pp. 1 - 6, 2014.

6. W. Doorsamy, and W. A. Cronje, "Semi-analytical method for predicting

shaft voltage in field-excited synchronous generators", *Journal of Power Electronics*, vol. 14, no. 5, pp. 859 - 865, 2014.

7. W. Doorsamy, A. Abdallh, W. A. Cronje, and L. Dupré, "An experimental design for static eccentricity detection in synchronous machines using a Cramér-Rao lower bound technique", *IEEE Transactions on Energy Conversion*, vol. PP, no. 99, pp. 1 - 8, 2014. *(Early Access)*

Contents

List of Figures **xi**

List of Tables **xvi**

Algorithm and Code Listings **xvii**

List of Symbols **xviii**

1 General Introduction **1**
- 1.1 Overview . . . 2
- 1.2 Problem Description . . . 2
- 1.3 Hypothesis . . . 4
- 1.4 Aims and Objectives . . . 4
- 1.5 Thesis Layout . . . 5
  - 1.5.1 Condition Monitoring of Electrical Rotating Machinery . . . 5
  - 1.5.2 Development of Theory for Shaft Voltages in Synchronous Generators . . . 6
  - 1.5.3 Uncertainty Analysis . . . 6
  - 1.5.4 Fault Detection with Principal Component Analysis . . . 6
  - 1.5.5 Bayesian Diagnostics . . . 7
  - 1.5.6 General Conclusions . . . 7
  - 1.5.7 Appendices . . . 7

2 Condition Monitoring of Electrical Rotating Machines **8**
- 2.1 Introduction . . . 9
- 2.2 Review of Condition-Monitoring Techniques . . . 10
  - 2.2.1 Chemical monitoring . . . 10
  - 2.2.2 Thermal monitoring . . . 10
  - 2.2.3 Mechanical monitoring . . . 11
  - 2.2.4 Electrical monitoring . . . 12
- 2.3 General Framework for Condition-Monitoring Systems . . . 13
  - 2.3.1 Asset Management and Maintenance Philosophy . . . 15
  - 2.3.2 Failure Mechanisms . . . 18
  - 2.3.3 System Architecture . . . 22

2.4 Shaft-Voltage-Based Condition Monitoring 25
2.4.1 Shaft-Voltage Origins 25
2.4.2 Historical Overview of Shaft Voltages 26
2.5 Conclusion 28

3 Development of Theory for Shaft Voltages in Synchronous Generators 29
3.1 Introduction 30
3.2 Physical Interpretation of Shaft Voltages 31
3.2.1 Shaft-Voltage Mitigation and Measurement 31
3.2.2 Conceptualisation of Shaft Voltages 33
3.3 Formulation of Predictive Model 34
3.4 Testing and Application of Predictive Model 40
3.4.1 Theoretical Substantiation 40
3.4.2 Experimental Validation of Predictive Model 41
3.4.3 Application in Fault Diagnostics 49
3.5 Conclusion 52

4 Uncertainty Analysis 53
4.1 Introduction 54
4.2 Measurement Modality Selection using Cramér-Rao Lower Bound Technique 54
4.2.1 Symptoms of Eccentricity Faults 55
4.2.2 Magnetic-Flux Monitoring 55
4.2.3 Methodology 56
4.2.3.1 Classical Cramér-Rao lower bound technique . . . 57
4.2.3.2 Adjusted Cramér-Rao lower bound technique . . . 58
4.2.3.3 Summary of methodology 59
4.2.3.4 Mathematical modelling 59
4.2.4 Numerical Results 62
4.2.4.1 Idealised model 62
4.2.4.2 Non-idealised model 64
4.2.5 Experimental Validation of CRLB Method 65
4.3 Uncertainty in Fault Diagnosis 70
4.3.1 Functional Requirements 70
4.3.2 Intelligence Component 71
4.4 Conclusion 73

5 Fault Detection with Principal Component Analysis 74
5.1 Introduction 75
5.2 Fault-Detection System 76
5.2.1 Background: Principal Component Analysis 76
5.2.2 Construction of Principal Component Model 77
5.2.2.1 Classical principal component analysis 77
5.2.2.2 Modified principal component analysis 78

5.2.3 T^2 and Q Statistics . . . 80
5.2.4 Numerical Results . . . 81
5.2.5 Experimental Validation . . . 86
5.3 Conclusion . . . 90

6 Bayesian Diagnostics **92**
6.1 Introduction . . . 93
6.2 Fundamentals of Bayesian Statistics . . . 93
6.3 Bayesian Spectrum Estimation . . . 95
6.3.1 Fault Diagnosis through Frequency Analysis . . . 95
6.3.2 Spectrum Estimation in Condition Monitoring . . . 97
6.3.2.1 Standard periodogram . . . 98
6.3.2.2 Welch method . . . 99
6.3.2.3 MUSIC method . . . 100
6.3.2.4 Bayesian method . . . 101
6.3.3 Performance of Techniques in Incipient Diagnosis . . . 105
6.3.3.1 Fault resolution . . . 105
6.3.3.2 Frequency estimation and spectral leakage . . . 106
6.3.3.3 Noise performance . . . 107
6.3.4 Evaluation . . . 108
6.4 Bayesian Fault Classification . . . 109
6.4.1 Probabilistic Classification using Bayes Theorem . . . 109
6.4.2 Fault-Classification System . . . 111
6.4.2.1 Algorithm overview . . . 111
6.4.2.2 Mathematical model of Naive-Bayes classifier . . . 112
6.4.2.3 Implementation and testing of classification algorithm . . . 115
6.5 Testing and Validation of System . . . 120
6.6 Conclusion . . . 124

7 General Conclusions **126**
7.1 Research Overview . . . 127
7.2 Conclusions and Significance of Research . . . 129
7.3 Further Research . . . 131
7.3.1 Extension of Presented Methodologies . . . 131
7.3.2 Industry Application . . . 132
7.3.3 Diversifying Application of Novel Methods . . . 133

References **134**

A Finite-Element Model **151**
A.1 Geometry and Physics . . . 152
A.2 Fault Modelling and Solution . . . 156

B Code listings **161**
B.1 Fault Detection 162
B.2 Fault Diagnosis 169
B.2.1 Bayesian Spectrum Estimation and Feature Extraction . . . 169
B.2.2 Fault Classification 180
B.2.3 Classifier Training Example and Output 187
B.3 Main Function for Online Monitoring 193

List of Figures

2.1 Flow diagram of major steps leading to the development of a modern condition-monitoring system for an electrical machine 14
2.2 General classification of maintenance strategies and philosophies according to system condition and process importance 15
2.3 Example graph of expected and modified failure rates over the life of an electrical rotating machine, with normalised axes 18
2.4 Example of the progression of faults and possible mechanisms to a failure mode in a synchronous generator 19
2.5 Mapping of common fault areas (see index given in table 2.1) on a generalised structure of an electrical rotating machine 20
2.6 Modern architecture for condition-monitoring systems used on electrical rotating machines 23
2.7 Basic timeline of shaft voltages and currents with regard to discovery and use in condition monitoring 27

3.1 Cross-sectional side view of 2-pole synchronous generator, illustrating physical location of shaft brushes used for measurement 33
3.2 Shaft-voltage measurement loop on a synchronous generator - i.e. across length 'ad' where point 'd' is grounded 34
3.3 Experimental setup with induction motor (prime mover) shaft brush and synchronous generator 36
3.4 Geometry and cross-sectional front-view of 2-D FE model of synchronous generator, illustrating path length "AB" 37
3.5 Numerical solution of magnetic flux densities, at various rotor positions over path "AB" (as shown in figure 3.4) 38
3.6 Process flow diagram describing methodology utilised for obtaining numerical solution of shaft voltage 38
3.7 Shaft voltage and corresponding flux waveforms under normal no-load conditions obtained using the predictive model 39
3.8 Experimental layout with instrumentation systems used to monitor and capture flux probe and shaft-voltage signals 42
3.9 Experimental and modelled shaft-voltage waveforms obtained under normal no-load conditions 43

3.10 Frequency content of the experimental and modelled shaft-voltage signals under normal no-load conditions and 25 A field excitation . 45
3.11 Comparison of third harmonic of FE model and experimental shaft voltages for different excitation currents on a synchronous generator 46
3.12 Rotor of the 2-pole synchronous generator depicting the end-winding configuration 48
3.13 Shaft-voltage waveform and corresponding frequency spectrum resulting from FE simulation of rotor end-windings only 49
3.14 Experimental generator with spacers used to adjust stator position relative to rotor thus inducing a static eccentric fault 50
3.15 Experimental and modelled shaft-voltage waveforms under no-load conditions with 0.5 mm static eccentricity fault 51
3.16 Frequency content of the experimental and modelled shaft-voltage signals under static eccentricity fault condition 51

4.1 Picture of flux probes on the inner surface of the stator of the experimental generator 56
4.2 Flowchart of methodology for measurement modality selection using the CLRB technique 60
4.3 Nonlinear $B-H$ curves of the rotor and stator core (mean values) 61
4.4 Normalised values of the simulated shaft and flux-probe voltage responses, for different eccentricity levels at no-load conditions . . . 63
4.5 Normalised waveforms for flux-probe voltages under normal conditions for the simulated FE model and experimental generator . . . 67
4.6 Normalised waveforms for shaft voltages, under normal conditions, for the simulated FE model and experimental generator 67
4.7 Bar chart indicating magnitudes of single-sided FFT of shaft voltages for different levels of eccentricity carried out in an experimental setting 69
4.8 Bar chart indicating magnitudes of single-sided FFT of flux-probe voltages for different levels of eccentricity carried out in an experimental setting 69
4.9 Machine-learning approach to approximating the mathematical target function of the fault-diagnosis subsystem 72

5.1 Flowchart with simplified illustration of stages for online condition monitoring on a synchronous generator 76
5.2 Overview of online fault-detection algorithm using PCA 82
5.3 Hotelling's T^2 statistic with occurrence of static eccentricity fault, under no-load conditions, evaluated using simulation data 83
5.4 Residual Q statistic with occurrence of static eccentricity fault, under no-load conditions, evaluated using simulation data 84
5.5 Hotelling T^2 statistic with occurrence of rotor winding inter-turn short-circuit fault, under no-load conditions, evaluated using simulation data 85

5.6 Residual Q statistic with occurrence of rotor winding inter-turn short-circuit fault, under no-load conditions, evaluated using simulation data 85
5.7 Hotelling's T^2 statistic with occurrence of static eccentricity fault, under no-load conditions, evaluated using experimental measurements 87
5.8 Residual Q statistic with occurrence of static eccentricity fault, under no-load conditions, evaluated using experimental measurements 87
5.9 Picture of experimental synchronous generator with inter-turn short-circuit fault on rotor overhangs 88
5.10 Hotelling T^2 statistic with occurrence of rotor winding inter-turn short-circuit fault, under no-load conditions, evaluated using experimental measurements 89
5.11 Residual Q statistic with occurrence of rotor winding inter-turn short-circuit fault, under no-load conditions, evaluated using experimental measurements 89
5.12 Hotelling T^2 statistics for occurrence of an eccentricity fault and for a change in load conditions - i.e. no-load to full-load condition - of the synchronous generator, evaluated using experimental measurements 91

6.1 Typical example of fault diagnosis on an electrical rotating machine using spectrum estimation 96
6.2 Comparison of percentage change in shaft-voltage harmonic, for two types of incipient fault increments, obtained using different spectrum-estimation techniques 106
6.3 Comparison of Welch and Bayesian spectrum estimations of a shaft-voltage signal for a $0.3\,mm$ static rotor eccentricity fault 107
6.4 Measure of relative error for spectral estimation technique, in identification of eccentricity affected harmonic, simulated under varying noise levels 108
6.5 Measure of variance for spectral-estimation techniques, in identifying an eccentricity fault, simulated under varying noise levels . . . 109
6.6 3-D Scatter plot, illustrating the relationship of the shaft-voltage harmonics under different conditions, with each point representing a shaft-voltage measurement on the experimental synchronous generator 110
6.7 Flowchart of fault-diagnosis algorithm for online classification of faults on a synchronous generator using shaft-voltage signals . . . 112
6.8 Scatter plot of simulated instances (without a load) illustrating relationship between the predicted class labels and posterior distribution of the shaft voltage's sixth harmonic feature only ("Jitter" is applied to Y-axis to reduce point concentration for presentation purposes). 117

6.9 Scatter plot of simulated instances (with a load) illustrating relationship between the predicted class labels and posterior distribution of the shaft voltage's sixth harmonic feature only ("Jitter" is applied to Y-axis to reduce point concentration) 117
6.10 Scatter plot of experimental instances (without a load) illustrating relationship between the predicted class labels and posterior distribution of the shaft voltage's sixth harmonic feature only ("Jitter" is applied to Y-axis to reduce point concentration) 119
6.11 Scatter plot of experimental instances (with a load) illustrating relationship between the predicted class labels and posterior distribution of the shaft voltage's sixth harmonic feature only ("Jitter" is applied to Y-axis to reduce point concentration) 119
6.12 Scatter plot of experimental instances (without a load) illustrating relationship between the predicted class labels and posterior distribution of the shaft voltage's second harmonic feature only ("Jitter" is applied to Y-axis to reduce point concentration) 120
6.13 Scatter plot of heterogeneous simulated instances (with and without a load) illustrating relationship between the predicted class labels and posterior distribution of the shaft voltage's sixth harmonic feature only ("Jitter" is applied to Y-axis to reduce point concentration) 122
6.14 Scatter plot of heterogeneous experimental instances (with and without a load) illustrating relationship between the predicted class labels and posterior distribution of the shaft voltage's sixth harmonic feature only ("Jitter" is applied to Y-axis to reduce point concentration) 122
6.15 Scatter plot of heterogeneous experimental instances (with and without a load) illustrating relationship between the predicted class labels and posterior distribution of the shaft voltage's third harmonic feature only ("Jitter" is applied to Y-axis to reduce point concentration) 123
6.16 Scatter plot of heterogeneous experimental instances (with and without a load) illustrating relationship between the predicted class labels and posterior distribution of the shaft voltage's tenth harmonic feature only ("Jitter" is applied to Y-axis to reduce point concentration) 123

A.1 FE model of synchronous generator indicating the different regions within the computation domain 154
A.2 FE model of synchronous generator, indicating only the winding regions 154
A.3 Circuit model for the physics component of FE model and external devices of the synchronous generator 157
A.4 Mesh of the computation domain of the FE model for the synchronous generator 159

A.5 Section of FE model geometry of synchronous generator with the mesh elements 159
A.6 Flux density along path AB of FE model of synchronous generator, under normal operating conditions, at different instances of time . 160

List of Tables

2.1 Index of failures and failure mechanisms corresponding to physical mapping on machine shown in figure 2.5 20

3.1 Shaft-voltage amplitude for diminished machine complexity and movement toward ideal conditions 40

4.1 Values of σ_δ for the two measurement modalities (no uncertain model parameters are considered) 64
4.2 Values of σ_δ for the two measurement modalities with uncertainty in the $B-H$ curve ($5\,\Omega$ load and $\delta = 0.6\,mm$) 65
4.3 Comparison between the values of σ_δ, for the two measurement modalities, as given by numerical and experimental results 68

5.1 $\Delta\mu_T$ and $\Delta\mu_Q$ evaluated using fault-detection algorithm on data obtained from various simulated conditions of synchronous generator 86
5.2 $\Delta\mu_T$ and $\Delta\mu_Q$ evaluated using fault-detection algorithm on data obtained from experimental measurements for various conditions of synchronous generator 90

6.1 Description of scenarios simulated with FE model to obtain shaft-voltage data for training the classifier 116
6.2 Probability distribution of test instances, obtained using the experimental generator with a load, over predicted classes 120

A.1 Geometrical parameters of the experimental synchronous generator 152

Algorithm and Code Listings

5.1 Main steps of online fault-detection algorithm using PCA 81
6.1 Algorithm for Bspec function used for Bayesian spectrum estimation 104
B.1 Implementation of PCA fault detection algorithm as a Matlab function 162
B.2 Matlab function for scripting of Bayesian spectrum-estimation function in an R run-time environment 169
B.3 Matlab function for saving an instance created in an R run-time environment 170
B.4 Function executed in R run-time environment - when called by Matlab script - to carry out Bayesian spectrum-estimation 172
B.5 Bayesian spectrum-estimation function of the Bspec package . . . 172
B.6 Matlab function used to extract harmonics from Bayesian spectrum estimate for use as features in the classifier 177
B.7 Validates the Java class path 180
B.8 Saves Java object to a data file 180
B.9 Loads data from file, into a Java object, for use by the classifier . . 181
B.10 Converts the input data to Java instances 182
B.11 Converts Java instances output from classifier, to a data file 183
B.12 Trains the classifier 185
B.13 Classifies the new instances, then returns the predictions and probability distributions 185
B.14 Calls and passes instances to training and/or classifier functions, and outputs fault diagnosis 186
B.15 Example of the training format for the classifier, using experimental data without a load 187
B.16 Example of an output from trained classifier 189
B.17 Main function 193

List of Symbols

$\mathbf{A}$	Availability
E_{AVE}	Average error of model
$\Delta\mu_T$	Change in the mean of Hotelling's test statistic T^2
$\Delta\mu_Q$	Change in the mean of sum of squares of residuals Q
C	Covariance matrix
J	Current density $[A/m^2]$
σ	Electrical conductivity $[\Omega^{-1}m^{-1}]$
E	Electric field intensity $[V/m]$
Φ_E	Electric scalar potential $[V]$
$\hat{\lambda}$	Empirical estimate of the failure rate of a machine
$\hat{\mu}$	Empirical estimate of the repair rate of a machine
$\hat{R}$	Estimate of autocorrelation sequence
$\hat{P}$	Estimate of signal spectrum/pseudospectrum
$EFIM$	Extended Fisher information matrix

ν	Feature of instance input to classifier
FIM	Fisher information matrix
T^2	Hotelling's test statistic
$\mathbf{I}$	Identity matrix
υ_i	Instance input to classifier
H	Magnetic field intensity $[A/m]$
ϕ	Magnetic flux $[Wb]$
B	Magnetic flux density $[T]$
μ	Magnetic permeability $[H/m]$
A	Magnetic scalar potential $[Vs/m]$
$\mathbf{M}$	Maintainability
Υ	Matrix of eigenvectors/coefficients matrix
$MTTF$	Mean time to failure
$MTTR$	Mean time to repair
$\Re$	Real number space
$\mathbf{R}$	Reliability
r_F	Residuals of principle components model
δ	Rotor eccentricity level
V_S	Shaft voltage [V]

Q	Sum of squares of residuals r_F
R	System Response
V	Total equivalent noise
E_T	Total error of model
S	Variance of noisy measured quantity
G	Variance of uncertain model parameter
$\mathbf{x}$	Vector of magnetic material parameters

Chapter 1

General Introduction

1.1 Overview

Condition-monitoring systems are essential for ensuring that generator units in power stations are operationally sound. These systems differ in complexity, cost and capability. Early detection of problems in machines is a sought-after capability and is the fundamental objective of predictive maintenance. The anticipation of incipient faults and replacement of problematic components - prior to further deterioration - eliminates the consequences of unexpected equipment failure.

Many condition-monitoring techniques have been found to exhibit capabilities for diagnosing incipient faults such as shaft-voltage-based methods used on synchronous generators [1]. Although the potential capabilities of shaft-voltage-based-methods are recognised, development of these capabilities for practical application has been subdued over the past decade. Advancement of this condition-monitoring technique is hindered due to complexities surrounding the processing and analysis of shaft voltage signals [2]. This is compounded by a lack of knowledge about physical interpretation and modelling of these induced voltages.

The research presented in this thesis aims to improve shaft-voltage-based condition monitoring of synchronous generators. In particular, it is focused on the development of processing and inferential methods for use with the shaft-voltage-based technique. A bottom-up approach is adopted for developing a system to provide early fault diagnosis on these machines. This is achieved through firstly constructing a framework for condition-monitoring system development. The shortcomings of shaft-voltage theory are then addressed with the conception of a predictive model. Thereafter, novel processing and inferential methods are used to design, implement and test an automated, intelligent and online fault diagnosis system.

1.2 Problem Description

Due to rapid growth of energy demands globally, emphasis has been placed on electricity providers in meeting projected load demands. This growth has led to increased stresses on generation systems, many of which comprise of ageing fleets.

The integrity of these generation systems is therefore crucial in providing efficient and reliable electricity supply. In general, the foremost motivations for predictive maintenance practice and increasing implementation of condition monitoring equipment in industry, are [3]:

- Progression of modern plants towards automation and hence less staffing and supervision.
- Avoidance of economic consequences as a result of unplanned shutdowns and undetected deterioration of equipment.
- Lack of redundancy in certain machine installations - especially where the machine is involved in a critical process.
- An increase in availability and a decline the in cost of advanced condition-monitoring technologies.

The aforementioned motivations are especially relevant to synchronous machines which are commonly utilised in power-generation schemes where the turbines are driven by fossil fuel, hydro or wind energy systems. These type of electrical rotating machines are critical components of power generation processes and it is therefore essential to ensure reliability through the discovery of problems well in advance [4]. The potential of using shaft voltages to diagnose faults on synchronous generators has been previously demonstrated. More recent works on the use of shaft-voltage techniques include [5], [6] and [7]. These publications deal with specific faults on electrical rotating machines and the effects thereof on shaft induced voltages. The most popular approach for identifying these effects is through analysing variations in the frequency components of the shaft-voltage signal. Furthermore, it has also been found that this technique has the potential to not only diagnose a specific fault, but also to do so when the fault is at an incipient level [8].

Although the establishment of these fault-frequency relationships has contributed to a better understanding of shaft voltages, there is still a significant lack of proficiency with the technique and suitability for practical application. The following were identified, through a review of previous work and correspondence with practi-

tioners, as the major obstacles preventing the progress and widespread application of shaft-voltage-based condition monitoring on synchronous generators:

- Uncertainty in terms of the physical interpretation and inception mechanisms of shaft voltages.
- Absence of a practical method for modelling shaft voltages.
- Insufficient qualitative and quantitative evidence of the merits of shaft-voltage-based fault diagnosis.
- Inadequate processing methods for extracting useful information from a shaft-voltage signal.
- Lack of inferential methods that can utilise shaft voltages for reliable fault diagnosis.

1.3 Hypothesis

"*Shaft voltage based condition monitoring of synchronous generators can be improved using a suitable model - together with processing and inferential techniques*".

In order to obtain clarity on "*improved"* and to avoid generalisation, the question, "*How is this condition monitoring technique improved?*", must be answered. The answer is directly related to the current problems with the technique and overcoming the aforementioned obstacles. Simply put, the shaft voltage is improved when there is a significant extension of fundamental knowledge, validation of the merits for its use in fault diagnosis, and suitable processing and inferential methods to optimise its practical application. These processing and inferential methods optimise shaft-voltage-based condition monitoring by increasing the reliability, efficiency and accuracy of the overall system.

1.4 Aims and Objectives

The research aims to address the aforementioned problems with the ultimate goal of improving shaft-voltage-based condition monitoring for practical application.

The major objectives of the research are to:

- Determine a modern framework for the development of a condition-monitoring system to be used in the presented work.
- Develop and test theory using basic electromagnetic principles and FE methods, which suitably describes and models shaft voltages in synchronous generators.
- Determine a method for qualitatively and quantitatively assessing shaft-voltage-based fault diagnosis, and in so doing investigate the limitations and merits associated with this diagnostic technique, in the form of a comparison to a widely used technique.
- Investigate optimum signal-processing techniques and determine a suitable candidate for use in shaft-voltage-based fault diagnosis.
- Design, implement and test inferential methods which provide automatic and intelligent fault diagnosis using shaft voltages.

Meeting these objectives will not only significantly improve shaft-voltage-based condition monitoring, but will also yield valuable contributions to the field of condition monitoring of electrical rotating machines. In other words, the forecasted contributions are not constrained to the aforementioned objectives, but are expected to be potentially useful for other applications in condition monitoring.

1.5 Thesis Layout

1.5.1 Condition Monitoring of Electrical Rotating Machinery

Chapter 2 presents a review of condition-monitoring techniques used on electrical rotating machines. This chapter also presents a framework for selection and development of a modern condition-monitoring system. The framework deals with the adoption of a maintenance strategy, investigation of common failure mechanisms, and issues relating to system architecture. Details of the history and current theory of shaft voltages are then presented. The shortcomings of previously proposed theory and models are also given.

1.5.2 Development of Theory for Shaft Voltages in Synchronous Generators

Chapter 3 presents the development of theory for shaft voltages in synchronous generators. A physical interpretation of shaft voltages is proposed - to address the theoretical shortcomings discussed in the previous chapter. Thereafter, a novel method for predicting shaft voltages is semi-analytically derived and implemented using an Finite Element (FE) model. Investigations are conducted on the behaviour of shaft voltages under varying machine complexities and operating conditions, in order to clarify previous uncertainties regarding shaft-voltage phenomena. The proposed theory and model are then experimentally validated. Performance of the model is also assessed for application in the diagnosis of an eccentricity fault.

1.5.3 Uncertainty Analysis

In Chapter 4, the uncertainties surrounding shaft-voltage-based monitoring are analysed. Firstly, the merits of using shaft voltages for condition monitoring are evaluated - both qualitatively and quantitatively. In order to perform such an evaluation, a method for optimal measurement modality selection - which uses the Cramér-Rao Lower Bound - is presented. This method is used to compare the shaft voltage with the flux-probe technique for diagnosis of static eccentricity.

Thereafter, the uncertainty in the diagnostic assessment which imposes limitations on the practical application of shaft-voltage-based condition monitoring, is analysed. A set of requirements are drawn from this analysis and are used to specify fault detection and fault diagnosis subsystems.

1.5.4 Fault Detection with Principal Component Analysis

Chapter 5 presents an online fault-detection subsystem which improves the overall efficiency and reliability of the presented shaft-voltage-based condition-monitoring system. Classical principal component analysis (PCA) is modified for use in the fault-detection algorithm. The algorithm is implemented and tested in an experimental setting.

1.5.5 Bayesian Diagnostics

In Chapter 6, the fault-diagnosis component of the condition-monitoring system is presented. Firstly, the performance of the Bayesian spectrum estimation technique is evaluated in the context of the application, and is compared to other modern signal-processing techniques. Thereafter, a fault classification algorithm is trained and validated. Finally, the complete system is experimentally validated.

1.5.6 General Conclusions

Chapter 7 gives concluding remarks and a summary of the work presented in this thesis. This is followed by suggestions for further research.

1.5.7 Appendices

Two Appendices are presented: Appendix A gives the details of the FE model of the synchronous generator used for the presented work. Appendix B lists code implementations of the various components of the shaft-voltage-based condition-monitoring system.

Chapter 2

Condition Monitoring of Electrical Rotating Machines

2.1 Introduction

Electric motor-driven systems are estimated to account for 43% to 46% of total global energy consumption [9]. The actual application of the motor consumes the vast majority of the electricity supplied to these systems. The total global energy demand is projected to grow by one-third from 2011 to 2035, as given by energy policies described in [10]. These facts indicate the significance of electric rotating machinery - from both a generation and demand side. Machines utilised in core processes in power generation can feature capacities exceeding $1\,GW$, whilst machines utilised in support processes in other industries can exceed $100\,MW$. Furthermore, the advancement of these machines has come about through an increase in demand for process optimisation and specialised requirements specific to the application. Given the sensitive nature and invested interest with respect to these applications, it is essential to have dedicated systems to monitor the machines involved. Furthermore, the area of condition monitoring has inherently followed this growth and advancement of machines - with new and progressive techniques being made available.

There are different types of methods used to prevent damage to equipment and unintended process shutdown. These methods correspond to different levels of security. For example, protection relays provide the interception of overcurrent faults and may initiate a sequence which results in the machine being disconnected. Although protection is essential in preventing catastrophic failure, in many cases it only provides action once the fault has reached an advanced stage. Condition monitoring differs as it exhibits proactive characteristics and may be established to provide predictive maintenance. This can prevent unplanned shutdowns and additional costs using methods which anticipate faults, failure and damage. This chapter focuses on the different aspects of condition-monitoring systems for electrical rotating machines. Section 2.2 briefly reviews available techniques before a general framework is presented in section 2.3. The framework considers the various aspects and subcomponents of a condition-monitoring system, i.e. overall maintenance strategy, failure modes, and system architecture. Section 2.4 presents background information on shaft voltages.

2.2 Review of Condition-Monitoring Techniques

Traditionally, condition-monitoring techniques are classified into four broad categories: chemical, thermal, mechanical and electrical.

2.2.1 Chemical monitoring

Insulation and lubrication are compound organic materials that can release a number of products upon degradation. Chemical techniques employ detection of matter or gases such as carbon monoxide and other hydrocarbons to determine early signs of insulation wear and excessive heating. Thermal degradation of insulation material occurs after exceeding a maximum allowable temperature, and gives off vapours or gases of certain chemicals used during manufacture. This thermochemical decomposition of organic material is termed pyrolysis [11].

Oil-analysis techniques are also used to diagnose wear on equipment. Chemical properties of the lubricant such as viscosity, solids content, water content, acid number and base number can be used to diagnose different types of wear - e.g. abrasive wear, cavitation, adhesive wear, and fatigue [12]. An example of a specialised instrument used to collect decomposition products in generator coolants to diagnose wear, is the ion-chamber detector or 'core monitor' [13]. Other techniques which use chemical indicators to detect wear are ferrographic [14] and X-ray analysis [15].

2.2.2 Thermal monitoring

Thermal monitoring of a machine consists of temperature measurements and/or thermal modelling. Localised temperature monitoring uses thermocouples, resistance, or embedded temperature detectors. These are usually embedded in the stator winding, stator core, or bearings [16]. A drawback here is that metal type detectors require electrical isolation and must therefore be positioned a secure distance away from the windings or any electrically conductive components. Heat-flow equations can then be used to determine a more accurate estimate of the actual winding temperatures. Bulk monitoring is a method which utilises internal and external coolant temperatures to determine the thermal state of a machine.

Advancements in this area have seen the development of non-contact methods that utilise infrared-sensors or infrared-cameras to measure rotor temperatures as given in [17], [18] and [19].

Thermal modelling uses finite element-based models or lumped parameter models [20]. Finite element method (FEM) and finite difference method (FDM) tools are tradionally used to optimise performance during the design stage of a machine. This is because these methods require significant computational effort - especially for complex geometries and non-homogenous bodies. However, components of the machine, e.g. rotor or stator, may be separately modelled quite accurately. Lumped parameter models require less computational effort and can determine temperature changes in different components of the machine [21]. Dynamic lumped parameter models can also use online information such as voltage, current and surface temperature to non-invasively determine the internal thermal state of the machine [18]. However, lumped parameter modelling is not feasible for all applications, as parameter extraction requires either extensive temperature measurement or comprehensive knowledge of the machine's construction and dimensions [22].

2.2.3 Mechanical monitoring

Vibration, accoustic emissions, torque and shock pulses are commonly monitored symptoms. Vibration faults can originate from two types of sources, i.e. mechanical and electromagnetic sources [23]. Examples are bearing faults, non-even air gap, asymmetrical power supply, structural resonance, winding damage, magnetic asymmetries, and imbalances in the driven load. Vibration monitoring is a widely used technique because of versatility - i.e. it can be used on virtually any machine, is used online and has achieved much success in practice. Some techniques may compare vibration levels according to specific standards for fault detection, while others may process vibration signals to determine fault severity and origin. Different types of accelerometers are available for measuring vibration, such as standard piezoelectric accelerometers or more specialised non-conductive fibre-optic accelerometers [24]. Accoustic emission techniques measure and analyse the noise signal

emitted by the machine, are particularly useful for detecting eccentricity and bearing faults [25]. Torque fluctuations can also be used to diagnose air-gap eccentricity and damaged bearings or couplings [26]. An estimation of the torque is obtained using a model and then is compared to actual measurements. Shock-pulse monitoring is similar to vibration monitoring, but detects higher frequency shock waves caused by rolling elements in bearings [27].

2.2.4 Electrical monitoring

Faults on a machine usually result in perturbations in the electrical quantities of a machine, such as the current, voltage and power. Disturbances in these electrical quantities also cause variations in the magnetic fields that may be detected. These electrical quantities are usually compared to measurements obtained under healthy machine conditions. High-frequency signal injection can also be used for fault detection [28], but is limited to specific applications due to hardware requirements and invasiveness.

Online partial discharge monitoring has been found to be a reliable method of diagnosing most high-voltage stator winding insulation failure processes [29]. Numerous methods are available for the early detection of partial discharge activity in this context. Some examples are earth-loop transient, capacitive coupling and RF coupling methods - as presented in [30] and [31]. Another method which has been reported to be successful in diagnosing stator winding, rotor bar and end-ring faults - is transient analysis of the stator current. This method diagnoses faults through measurement and analysis of current imbalances [32]. An extended version of this method is the power decomposition technique (PDT) which derives positive and negative sequence voltages and currents for fault detection [33]. Motor current signature analysis (MCSA) uses current frequency spectra to diagnose faults and is popular because it is online, non-invasive and does not require advanced sensors [34].

Axial flux techniques utilise externally mounted search coils or Hall probes as sensors to detect leakage/stray flux [35]. These techniques identify faults such as

inter-turn, broken rotor bar and eccentricity faults by examining variations in the spectral components of the flux [36]. A similar technique to the axial-flux method uses shaft voltages to detect faults. Early measures to ground shaft currents which cause bearing damage - primarily used in large turbo-generators - have evolved into a method of diagnosing faults on a machine through analysis of these signals. This technique utilises specialised brushes on either side of the rotor shaft to measure induced voltages along the length of the machine, as described in [1], [37] and [38], and is the primary focus of the presented research.

The use of artificial intelligence (AI) techniques has extended from control into the field of condition monitoring. Techniques include expert systems, artificial neural networks (ANNs), fuzzy logic, and genetic algorithms (GAs). These systems have been developed to automate the interpretation stage and precisely indicate fault conditions by tracing the possible root causes, as described in [39]. Examples of application of these techniques are given in [40] and [41]. Furthermore, recent advancements in computational intelligence, signal processing, and statistical methods have enabled development of condition-monitoring systems beyond measurement techniques. Modern systems may consist of supplementary components to improve overall reliability, efficiency and functionality. Hence, the selection or development of a suitable condition-monitoring system requires a more detailed understanding of underlying issues specific to the application. The following section presents a general framework to assist with the understanding, development and optimisation of modern condition-monitoring systems.

2.3 General Framework for Condition-Monitoring Systems

The overall effectiveness of a system that consists of multiple components in series, depends on the individual effectiveness of each component. For example, consider a condition-monitoring system that uses spectrum analysis of a voltage signal to diagnose faults. The system could use an accurate sensor and advanced signal preconditioning equipment, but if the actual spectrum estimation tech-

nique is inaccurate, the final diagnosis will be incorrect and will render the entire condition-monitoring system ineffective. Development of a condition-monitoring system therefore requires careful consideration of each component or subsystem.

Furthermore, the condition-monitoring system may not always require advanced techniques or expensive sensors depending on the application. The application requirements and maintenance specifications must therefore be determined before a suitable system can be selected or developed. Figure 2.1 (below) shows a simple flow diagram of the steps proposed by the framework, leading to the selection or development of a modern condition-monitoring system.

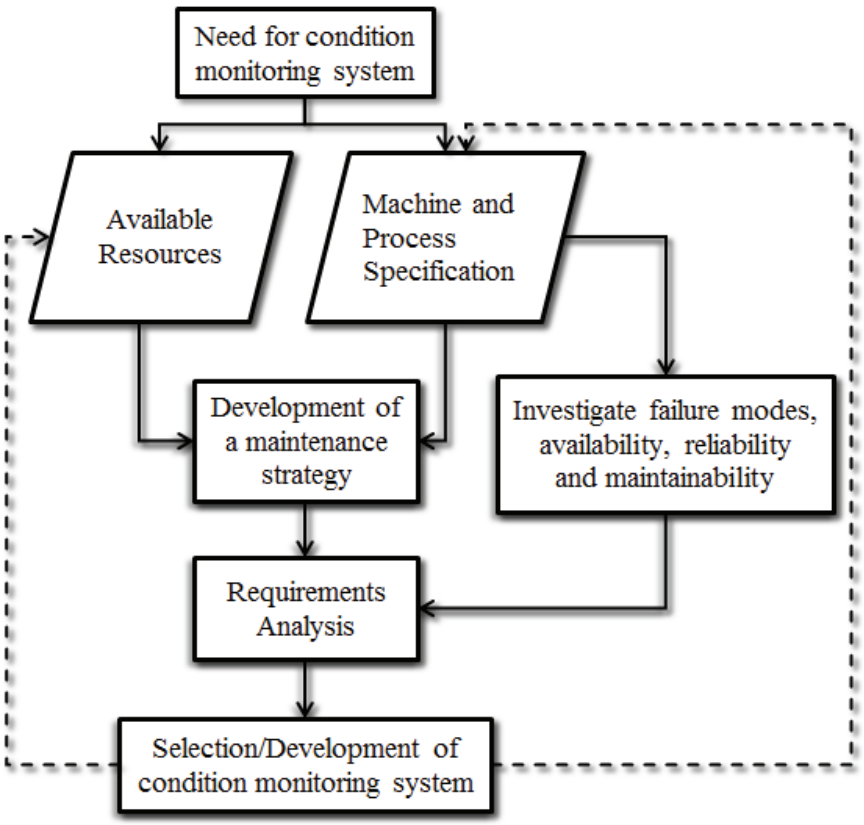


Figure 2.1: Flow diagram of major steps leading to the development of a modern condition-monitoring system for an electrical machine

2.3.1 Asset Management and Maintenance Philosophy

Best practices in asset management usually employ condition-monitoring systems within a broader maintenance strategy. Development of a strategy and adoption of a maintenance philosophy depends on the value of the asset and the importance of the process [42]. In other words, the type of maintenance strategy selected depends on the priority of the machine within the process.

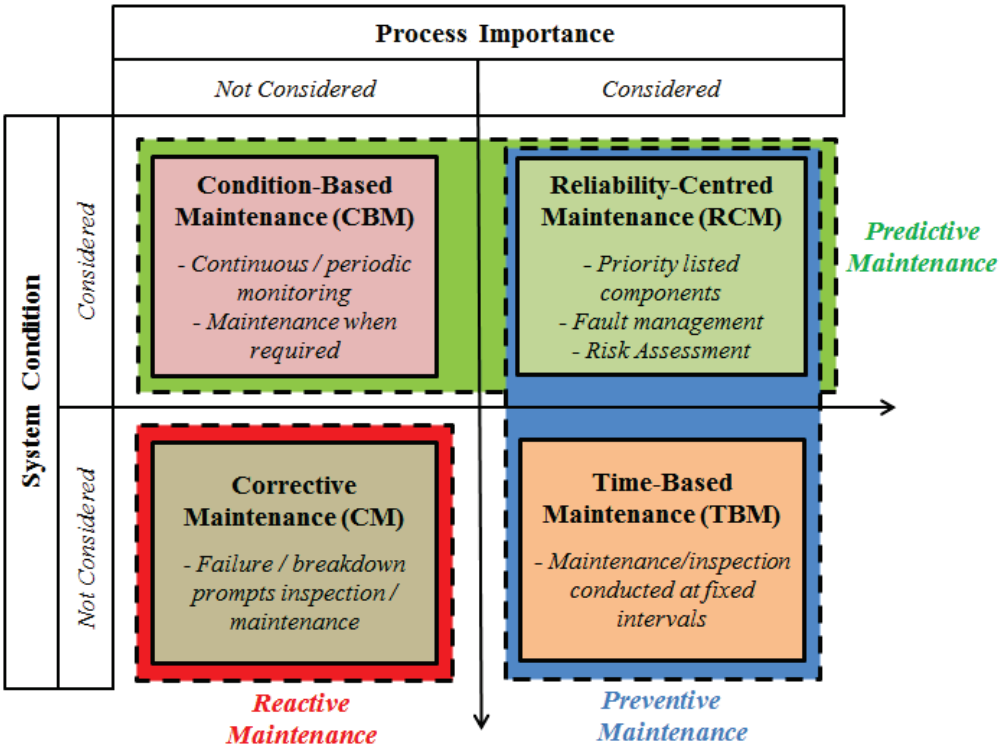


Figure 2.2: General classification of maintenance strategies and philosophies according to system condition and process importance

A general classification of maintenance strategies and how these fit into the different maintenance philosophies, is illustrated in figure 2.2 (above). There are four types of maintenance strategies, which are classified according to two major aspects of asset management: importance of the process and condition of the machine. For example, a condition-based maintenance (CBM) strategy consists of maintenance procedures and policies based on the condition of the machine and does not focus

on the actual importance of the machine within the overall process. In contrast to this, a time-based maintenance (TBM) strategy would rely on process importance to schedule maintenance for a machine - regardless of its current condition.

Figure 2.2 also indicates how each strategy relates to general maintenance philosophy. A corrective maintenance (CM) strategy can be described as a reactive maintenance philosophy, whereas reliability-centred maintenance (RCM) employs both preventive and predictive measures. Predictive maintenance practice is utilised for critical processes and usually requires advanced monitoring techniques. For example, this strategy would be used for generator maintenance at a power station, since both the system condition and process importance need to be considered. The condition of a generator is important because redundancy is not feasible due to the high costs associated with these machines. Generators are also critical components of a power station and serve a key function in the overall process.

Reliability, availability, maintainability and safety of the machine must also be considered when selecting a maintenance strategy. Reliability (**R**) is defined as the ability of a machine to perform the required function over a specified time [43]. This characteristic may be measured as the mean time to failure ($MTTF$), which is given by,

$$\mathbf{R} = MTTF = \frac{1}{\hat{\lambda}} \tag{2.1}$$

where $\hat{\lambda}$ is an empirical estimate of the failure rate of the machine. The maintainability (**M**) is defined as the ability of the machine to be restored to satisfactory function after a failure has occurred. The characteristic is measured using the mean time to repair ($MTTR$) and may be expressed as:

$$\mathbf{M} = MTTR = \frac{1}{\hat{\mu}} \tag{2.2}$$

where $\hat{\mu}$ is an empirical estimate of the repair rate of the machine. The availability (**A**) is defined as the probability that the machine will operate adequately at any

period of time. This characteristic may be expressed using the $MTTF$, and the $MTTR$ as given by equation 2.3 [44]:

$$\mathbf{A} = \frac{MTTF}{MTTR + MTTF} \tag{2.3}$$

Safety is the ability of the machine to avoid causing harm to persons, equipment or the environment - when a fault or failure occurs. This characteristic is usually assigned a status rather than a quantity, determined by analysing the risk of the machine. Hence, the machine will be considered as "safe" when the risk of harm to people, equipment or the environment is below a predefined threshold. The risk associated with a machine can be reduced by using protective equipment - e.g. protection relays. However, the addition of components can reduce the overall reliability of the system.

Although protection is essential for safety and can assist in preventing catastrophic failure, it does not necessarily improve the reliability of the system. For example, a generator protection relay can provide overcurrent protection on a machine, but cannot detect and prevent the internal fault which induced the overcurrent.

A well designed condition-monitoring system can provide predictive maintenance and improve the reliability of a machine. This is achieved by reducing the number of failures over the life of the machine. A graph of the expected number of failures over the life of a machine is presented in figure 2.3 (below). The magnitude of the graph's axes are normalised as actual life expectancy and number of failures will vary according to the machine and application. 𝔸 is the early failure stage, 𝔹 is the useful-life, and ℂ is the ageing/wear out period.

A condition-monitoring system can improve reliability of the machine by effectively "modifying" the expected number of failures of a machine in each of these three stages. For example, early diagnosis of a fault on an ageing unit enables pre-emptive repair or replacement of the problematic components - thereby extending the life of the machine.

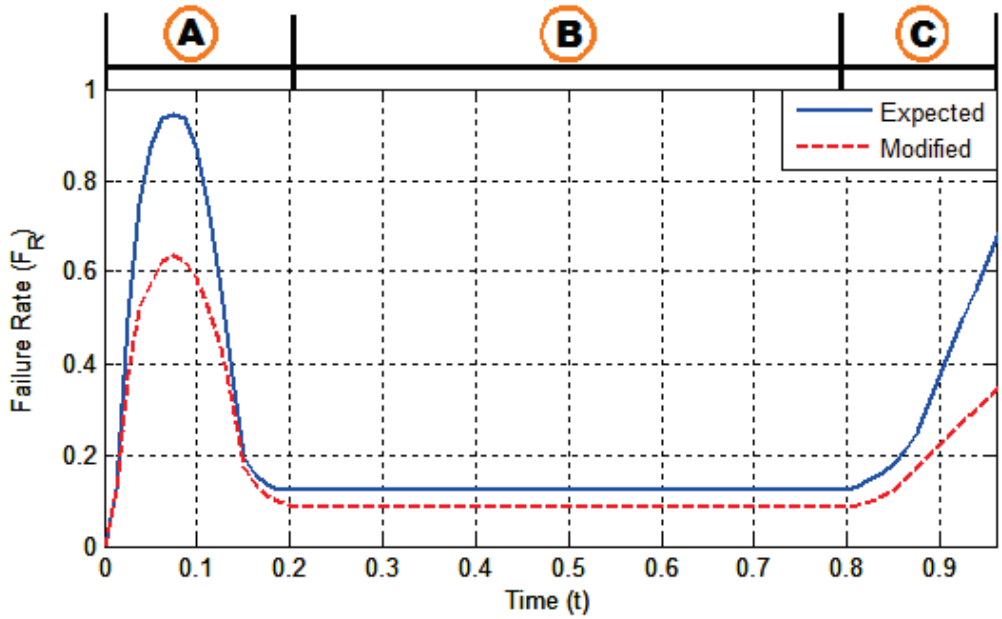


Figure 2.3: Example graph of expected and modified failure rates over the life of an electrical rotating machine, with normalised axes

2.3.2 Failure Mechanisms

Most typical failures in machines result from a process of successive faults. These faults tend to develop from abnormalities and may therefore be considered to be symptoms of a root cause or an incipient fault. The failure is therefore a result of the progression of an incipient fault through a cascading effect. For example, the rotor windings on a synchronous generator are subjected to high centrifugal forces during normal operation, and this can result in insulation degradation and may eventually lead to inter-turn faults on the windings. Excessive currents created by the short-circuited windings cause localised heating which can lead to thermal bending of the rotor and rotor eccentricity. Eccentricity can lead to vibration and eventually bearing failure. This example of progression from an incipient fault to a typical failure mode is illustrated in figure 2.4 (below). It should be noted that - in practice - bearing failure and vibration can be caused by a number of different fault mechanisms.

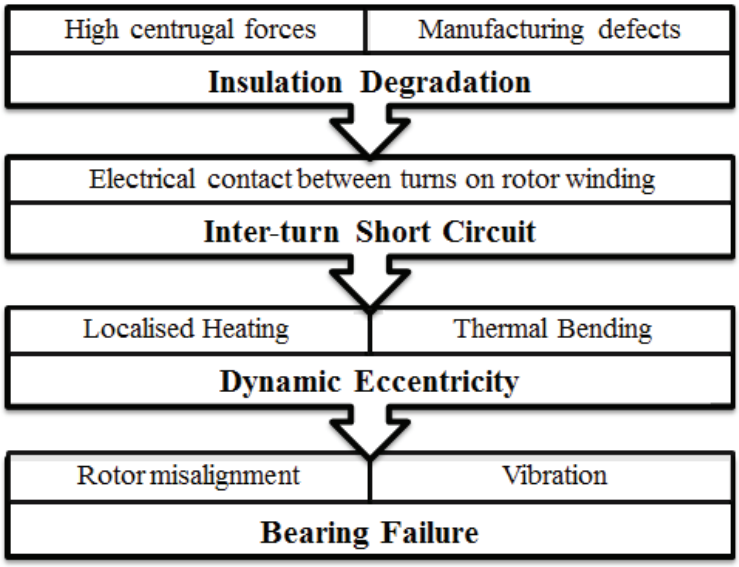


Figure 2.4: Example of the progression of faults and possible mechanisms to a failure mode in a synchronous generator

Figure 2.5 (below) depicts the general structure of an electrical rotating machine, with a physical mapping of common failures and failure mechanisms listed in table 2.1. The following faults on electrical rotating machines are commonly experienced in industry [45, 46]:

- Stator winding faults
- Rotor winding faults
- Air-gap faults (static and dynamic eccentricity)
- Broken rotor bars and cracked end-rings
- Slip ring or brush failure
- Core or lamination damage
- Circulating currents and earth faults
- Failure of peripheral equipment such as bearings, gearbox, cooling system, bushings and electrical connections

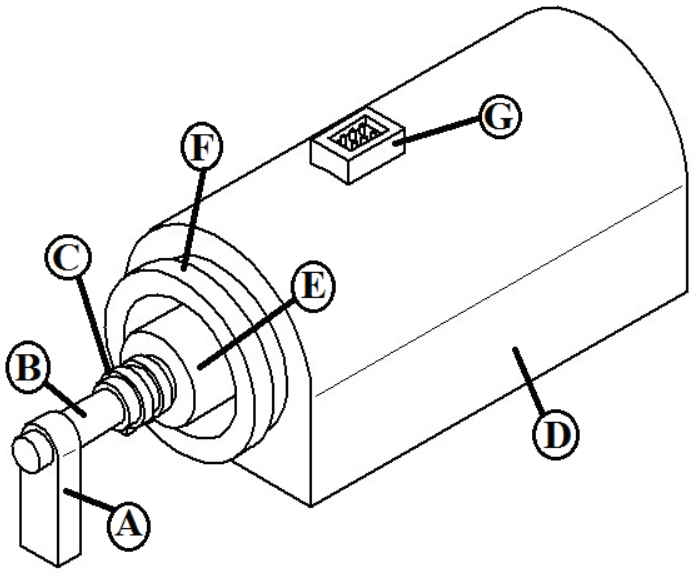


Figure 2.5: Mapping of common fault areas (see index given in table 2.1) on a generalised structure of an electrical rotating machine

Table 2.1: Index of failures and failure mechanisms corresponding to physical mapping on machine shown in figure 2.5

Area	Failure Mechanisms
A	Bearing failure
B	Shaft eccentricity
C	Slip ring or brush failure
D	Stator core damage or circulating currents
E	Rotor core, winding or end-ring damage
F	Stator winding, end-winding or core damage
G	External electrical faults

Insulation faults on stator and rotor windings are major contributors to failures in rotating machines. In industrial applications, machines are exposed to adverse environmental conditions, electrical stresses, and mechanical stresses which degrade

the insulation over time. Excessive voltage levels can lead to partial discharges between adjacent wires which erode wire enamel and cause electrical ageing of the insulation [47]. Other stresses which cause accelerated ageing of insulation are mechanical vibration, high ambient temperatures, moisture, and the presence of corrosive materials [48]. Insulation faults usually result in inter-turn winding short-circuits on the stator and rotor - as described in [40], [49] and [50]. Inter-turn faults on rotor windings are a common problem in generators and can lead to vibration, increased shaft voltages, winding burn-out, and loss of excitation [51].

Electrical connection faults are more common in machines operating at higher voltages where there is increased dielectric stress on bushings and larger forces on conductors. Bushing failure may occur due to mechanical vibration or electrical tracking due to debris deposited on exposed surfaces. Partial discharge activity is an indicator of this condition [45]. A core fault is usually limited to large turbine-driven machines where laminated cores bear excessive magnetic and electrical loads. Insulation failure and foreign bodies between core plates cause electrical connections that create circulating currents. The circulating currents, coupled with the main flux, cause excessive heating of the plates and can lead to additional weakening of the core. Eventually, the stator core may succumb to buckling, melting, cavity formation and earth faults, as described in [52], [53] and [53].

Defects also occur during the manufacturing process - such as casting defects in die-cast rotors and poor joints in brazed or welded end-rings. These factors are found to be the primary causes of broken rotor bars and cracked end-rings [54, 55]. Current migration due to skin effect can also result in uneven heating and expansion of rotor bars, which can result in separation from the end rings [56]. Problems with slip rings can also cause severe damage to machines. Furthermore, current imbalances in external resistors or circuit-connected slip rings can result in overheating of the rotor. Threading and grooving of rings occur over time, while arcing can occur on rings due to loss of brush contact [57, 58]. This can result in brush gear failure, earth faults, and damage to the rotor windings.

An air-gap eccentricity fault is unequal positioning of the rotor relative to the stator, and is categorised into three forms: static, dynamic or mixed. In static eccentricity, the symmetrical axis of the rotor coincides with the rotor rotating axis, but is displaced with respect to the stator symmetrical axis. This means that the air-gap distribution is non-uniform, but the minimum air-gap angular position is fixed. In dynamic eccentricity, only the rotor symmetrical axis is displaced with respect to the rotor rotation axis, which coincides with the stator symmetrical axis [59]. This is a common fault which can occur through a number of different mechanisms - such as bearing wear, shaft deflection, and thermal bending. Eccentricity in a machine can result in critical damage due to mechanical rubbing between stator and rotor, bearing failure, vibration and asymmetric magnetic fields [60]. Bearing failure can also occur gradually under normal operating conditions. Sources of this failure include corrosion due to contaminants (abrasive particles), heating due to incorrect lubrication, and indentation or brinelling due to improper installation or shaft alignment [61].

2.3.3 System Architecture

A suitable condition-monitoring system may be specified once a maintenance strategy is selected and information regarding the machine is gathered. The maintenance strategy will prescribe the level of monitoring such as an automated early fault detection system, and supplementary information on typical failure mechanisms will assist in selection of the type of monitoring - e.g. bearing temperature monitoring. Figure 2.6 (below) illustrates the architecture of a condition-monitoring system, with examples of each subsystem. The measurement modality component illustrated in this figure refers to the quantity, parameter or signal that is used in a condition-monitoring system. This component is the primary source of information used to make an inference about the state of an electrical machine.

A single condition-monitoring system may use a combination of different types of measurements - e.g. one system may use both vibration and temperature measurements to infer the condition of a bearing. The usefulness of a specific measurement modality depends on the information required. The following questions are per-

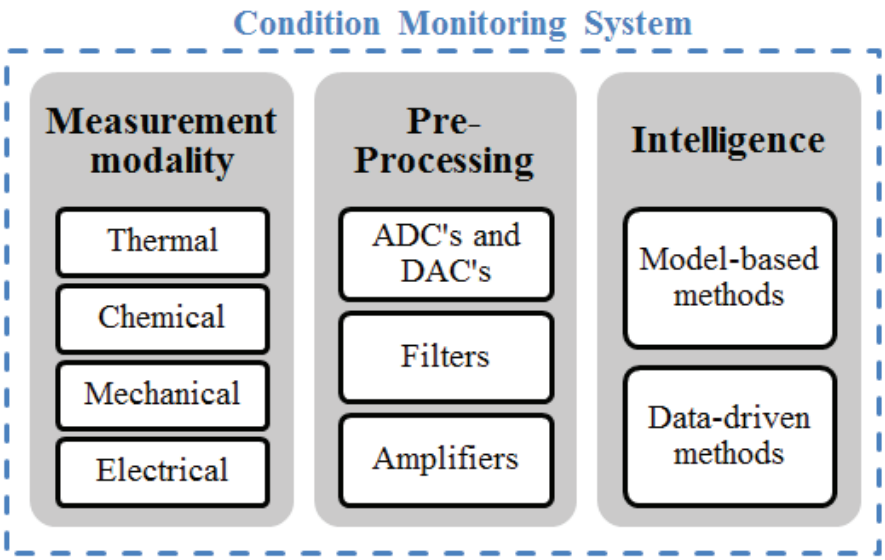


Figure 2.6: Modern architecture for condition-monitoring systems used on electrical rotating machines

tinent regarding the suitability of the measurement:

- Can the measurement modality be used to infer the status of the component of interest?
- Is the measurement modality adequately sensitive to the expected failure mechanism?
- Is the measurement done online or offline?

Solutions to these questions are not always obvious, and can vary in complexity depending on the machine and application. For example, localised heating on a rotor - as a result of an inter-turn short-circuit fault - will not necessarily be detected by a bearing temperature sensor. Specifying a maintenance strategy and investigating typical failure mechanisms, assists in answering the second question. The sensitivity of a measurement modality to a failure mechanism determines the early fault-detection capability of a condition monitoring system. Currently, there is no definitive method for assessing the early failure-detection capabilities of a measurement modality. Issues regarding the selection of a suitable measurement modality are addressed in greater detail in chapter 4.

The pre-processing subsystem shown in figure 2.6 is responsible for pre-conditioning and data acquisition. Pre-processing equipment can vary depending on the availability of resources and the selected measurement modality. However, most systems use standard pre-conditioning devices such as amplifiers, anti-aliasing filters, analogue-to-digital convertors, and digital-to-analogue converters. More advanced systems may use smart data acquisition with multiplexers, microcontrollers, and digital signal processors [62]. Specification, design and implementation of a pre-processing subsystem are well-defined practices in the field of instrumentation and are therefore not considered any further in this thesis.

The third major component of a modern condition-monitoring system is the intelligence - which refers to detection, inference and classification techniques. This is perhaps the most dynamic aspect of current condition monitoring systems, due to the ever-changing fields of statistics and computational intelligence. Since a wide variety of techniques are available, it is more suitable to formulate two broad categories according to function: fault detection and fault diagnosis. Fault detection refers to the capability of a system to determine if a fault has occurred. This capability is extended in the case of fault diagnosis, which provides more information such as the type and location of the fault.

The following are examples of fault-detection methods used in condition monitoring of electrical rotating machines:

- Threshold checking [63].
- Signal model-based techniques such as correlation, wavelet and spectrum estimation [64].
- Statistical techniques such as univariate and multivariate analysis [65, 66].

Fault-detection methods are used to obtain quantitative information from raw data. However, the major drawback is that human experts are still required to provide qualitative information. This manual assessment of a machine is vulnerable to human error and therefore is not suitable for critical applications. Additionally, large-scale applications will generate several monitored values, which can overbur-

den operators and complicate fault diagnosis. The following methods are used in modern condition-monitoring systems to provide automated fault diagnosis:

- Classification methods such as neural net classifiers, fuzzy classifiers, and decision trees/tables [67, 68].
- Inference and reasoning techniques such as predicate logic, neural networks and fuzzy logic [68, 69].

Diagnostic techniques can provide automatic assessments of the machine's condition, but do not offer complete replacement of fault-detection techniques. In fact, most modern systems use a combination of these techniques to optimise overall performance and efficiency. Chapters 5 and 6 present techniques for fault detection and fault diagnosis, respectively, which are used to develop and optimise the shaft-voltage-based condition-monitoring system.

2.4 Shaft-Voltage-Based Condition Monitoring

The presented research focuses on the application of shaft voltages as a measurement modality. As mentioned previously, development of a suitable condition-monitoring system requires a detailed understanding the measurement modality. The following sections present the history of shaft voltages and previous research.

2.4.1 Shaft-Voltage Origins

In a generator, the stray voltage observed across the rotating shaft - or the voltage difference between the shaft and ground plane - is termed the shaft voltage [70]. External electromagnetic interference does induce some effects, however the significant causes of shaft voltages can be classified into a three general types:

- Electromagnetic
- External Voltage Sources
- Electrostatic

The sources of shaft-induced voltages - under the category of electromagnetic - are residual magnetism, magnetic asymmetries, axial shaft flux, and homopolar flux.

A low-reluctance magnetic circuit coupled with sources of high residual magnetism such as the rotor, bearings and housing - can generate shaft voltages. Magnetic asymmetries, arising from acceptable manufacturing limitations and defects, commonly result in magnetic-flux linkage - which creates a shaft potential. Examples of these manufacturing imperfections are segmented cores and nominal static eccentricity. Other examples may include weld recesses and key ways on the stator core of the machine. Asymmetrical winding connections also create an axial/homopolar flux along the shaft - thereby inducing current flow [71].

External voltage sources supplied through excitation equipment can also induce currents in the shaft via capacitive coupling. Harmonics in these voltages sources - e.g. rectifier circuit output - are also transferred through this mechanism and impact the frequency characteristics of the shaft voltage. Electrostatic sources are common in power-generation applications and originate from capacitive charges which generate high voltages. A shaft potential is created by the separation of charge when wet steam flows through the turbine blades [72]. A detailed physical interpretation of shaft voltages is given in the next chapter.

2.4.2 Historical Overview of Shaft Voltages

Shaft voltages were initially discovered as a major root cause of bearing failure (one example of the earliest reports was published in 1907 by a manufacturer in [73]). This scenario prompted extensive research and development effort to mitigate the aforementioned effects - as early as 1910 [74]. Efforts to control and eliminate the problems caused by shaft voltages endured with notable works such as [75, 76]. Recognition of shaft voltages in turbine generators was illustrated in the early 1970s through the publication of guidelines that initiated an increasingly standard utilisation of techniques to mitigate shaft voltages such as insulated bearings and grounding brushes [77].

In the late 1980s, widespread use of solid-state drives on electric machines resulted in a parallel increase in bearing failures. Previously, shaft voltages and bearing currents at $50\,Hz$ and $60\,Hz$ operation were recognised as a problem, but with

increased usage of step-like voltage sources and high $\frac{dv}{dt}'s$ - higher shaft voltages and bearing currents were induced. In the early 1990s, shaft voltages were discovered to be potentially useful for detecting faults and monitoring the health of electrical rotating machines - as presented in [78] and [79]. This was inferred from evidence that shaft voltages are created via magnetic mechanisms and knowledge that most faults cause magnetic field perturbations. The development of shaft-voltage monitoring systems for turbine generators commenced shortly afterwards - approximately a decade ago [1, 80]. Figure 2.7 illustrates a timeline consisting of research and development milestones in the area of shaft voltages.

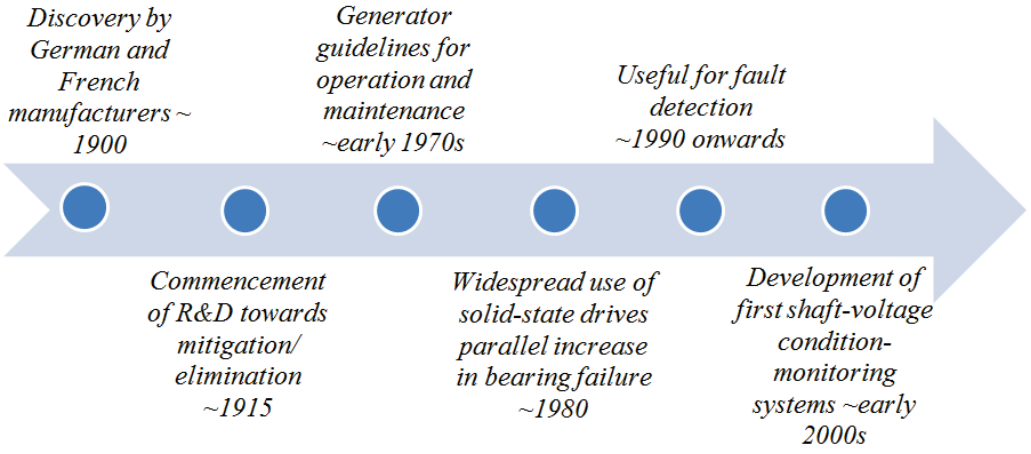


Figure 2.7: Basic timeline of shaft voltages and currents with regard to discovery and use in condition monitoring

During this period, reasons for the behaviour of shaft voltages were offered - along with different models to characterise the observed phenomena. Examples of these models - which utilise capacitive coupling and other effects such as non-ideal DC field excitation or three-phase rectifiers - are provided in [72] and [81]. Circuit models have also been used to characterise shaft voltages and currents, such as the model presented in [78]. These earlier models do not account for several characteristics of shaft voltages, such as different constituent harmonics. Therefore, physical interpretation of these induced voltages depends entirely on heuristic knowledge or experimental data.

2.5 Conclusion

In this chapter, some fundamentals of condition monitoring of electrical rotating machines are presented. This information is intended to help the reader to understand the purpose of the research and the results presented in the chapters to come.

The condition-monitoring techniques traditionally categorised as chemical, thermal, mechanical and electrical, are reviewed. Modern condition-monitoring systems have advanced beyond these traditional techniques due to progression in the fields of computational intelligence, statistical methods, and signal processing. Furthermore, there is a growing need for automated condition-monitoring systems as predictive maintenance tools.

A framework for modern condition-monitoring systems is also presented and provides a systematic approach to specifying and developing a modern condition-monitoring system. System architecture is one of the major components of the framework and consists of measurement modality, processing and intelligence sub-components. Background information is given on shaft voltages - which is the measurement modality of the condition-monitoring system presented in this thesis.

Chapter 3

Development of Theory for Shaft Voltages in Synchronous Generators

3.1 Introduction

The phenomena of shaft voltages in electrical rotating machines were initially observed more than a century ago. The scope of research and development in this area has subsequently ranged from protection strategies (shaft-voltage mitigation) in generators and machines with variable frequency drives (VFDs) to condition-monitoring applications in generators. Although many interpretations of shaft voltages have been offered during this period, no clear theoretical description is available that accounts for the numerous characteristics of these phenomena. These theoretical shortcomings are particularly evident in the case of synchronous machines, wherein the origins and influential parameters of shaft voltages are uncertain. Shaft voltages in generators are significant from both protection and condition monitoring perspectives [1, 80]. Previous works have indicated that for protection purposes, predicting the induced voltage levels as early as the design stage, is useful. With condition monitoring and predictive maintenance, in particular, accurately relating minor variations in shaft voltages to specific machine parameters is advantageous. However, an adequate theoretical framework for modelling shaft voltages has not yet been proposed.

This chapter aims to address the aforementioned shortcomings, specifically with regards to synchronous generators, which are widely used in power stations worldwide. The conventional 2-pole machine uses a field winding with static DC excitation and a solid cylindrical rotor. A method for predicting shaft voltages in synchronous generators is derived from fundamental electromagnetic theory by using a semi-analytical approach. A detailed deliberation of the construction and implementation of the finite element (FE) model is given. Additionally, a systematic validation is provided through theoretical substantiation and accuracy estimation via an experimental system. The presented shaft-voltage model is also tested for application in fault diagnosis.

3.2 Physical Interpretation of Shaft Voltages

In general, an engineering problem may have many sources of uncertainty and it is therefore suitable to categorise these accordingly. Uncertainty can be broadly classified into 2 types, according to the source, namely aleatory and epistemic uncertainty [82]. Aleatory uncertainty is due to intrinsic randomness, and epistemic uncertainty originates directly from a lack of knowledge. Uncertainty with the measurement modality and fault diagnosis is discussed in greater detail in the next chapter, but it is highlighted here in order to explicate the significance of the work presented in this section. The purpose of this section is to reduce epistemic uncertainty with regards to shaft voltages in synchronous generators by extending current theory and developing a new model.

Although extensive work - as described in section 2.4 - has been conducted over the years, there is still no definitive physical interpretation of shaft voltages in synchronous generators. Therefore, deficiency in the theory is addressed before deriving a model to predict shaft voltages in 2-pole synchronous generators. A semi-analytical approach is used to model shaft voltages by applying fundamental electromagnetic theory to derive a theoretical model from a conceptual model. A physical interpretation or conceptualisation of shaft voltages in synchronous generators is thus a prerequisite for the presented analytical methodology. The measurement concept for the phenomena is considered in order to obtain a physical interpretation of shaft voltages.

3.2.1 Shaft-Voltage Mitigation and Measurement

Initially, shaft voltages and circulating currents were found to negatively impact machines and this prompted development of methods to mitigate these effects. Examples of these methods, which are still used today, are insulated bearings and grounding brushes on the machine. When the shaft potential reaches a certain level, electrical discharge occurs across the smaller spaces to ground. Therefore, components with reduced clearances from the shaft are most susceptible to damage as a result of these discharges. Hence, this mechanism is more prevalent in modern machines which are designed and manufactured with smaller clearances.

There are no counter-measures to completely eliminate such voltages. However, there are effective methods to diminish negative effects through techniques such as increasing stability and reliability of the ground grid. Proper bonding of all components to the ground grid is essential whilst maintaining a reliable grounding brush installation.

There are various types of shaft brushes available but not all are suitable for accurate shaft signal acquisition. The following are some examples of different shaft brushes [82]:

- Metal fibre brushes with silver-alloy composite for shaft grounding and bearing protection.
- Conductive carbon microfibre rings for shaft grounding and bearing protection.
- Copper-composite braids for shaft grounding and bearing protection.
- Silver-gold composite shaft-riding brushes for shaft grounding, bearing protection and measurement of shaft voltages [83].

Accurate measurement of shaft-grounding current and shaft voltages is quite challenging due to accessibility to shaft sections and a reliable ground grid. The recommended practice for shaft-voltage measurement is the placement of the brushes on either side of the shaft extension - i.e. outboard-side (excitation end) and inboard-side (driven end or turbine-side in power plants) [84]. Applications which do not have reliable ground grids may use an additional brush, on the inboard-side, connected to ground through a shunt resistor. In this case, a differential voltage is obtained using the voltages measured across the resistor and across the brushes on either side of the shaft.

Figure 3.1 is an illustration of the cross-sectional side view of the generator used in this investigation and indicates where the shaft voltage is measured. The brushes are placed on the stator-side of the insulated bearings on either side of the shaft - i.e. inboard and outboard.

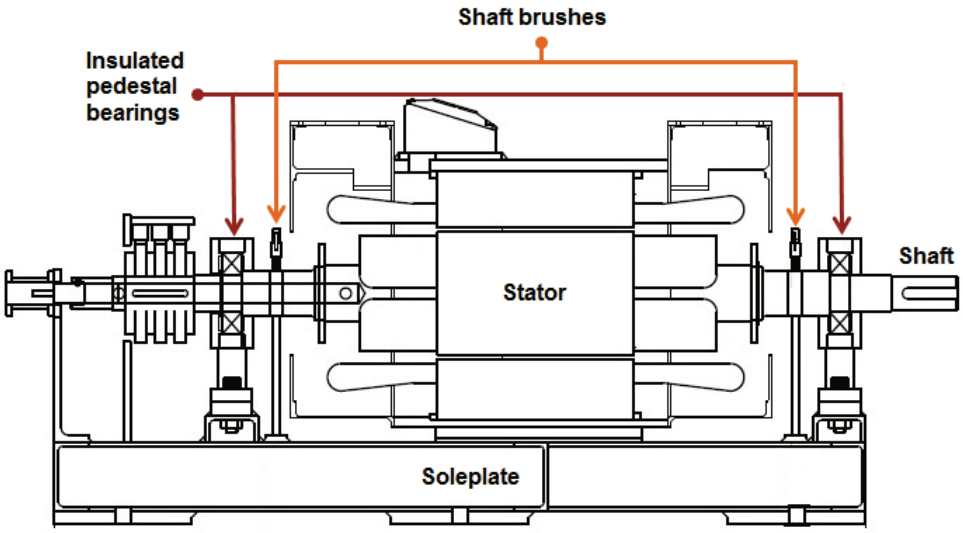


Figure 3.1: Cross-sectional side view of 2-pole synchronous generator, illustrating physical location of shaft brushes used for measurement

3.2.2 Conceptualisation of Shaft Voltages

In figure 3.2, the shaft voltage is measured as the potential across "a" and "d", where point "a" is typically the outboard or static excitation end, and point "d" is the inboard or driven end. When the shaft is under the action of a prime mover and the rotor windings are supplied with DC excitation, a rotating magnetomotive force (MMF) that is spatially sinusoidal under ideal conditions, is generated. The net flux (through the measurement loop shown in figure 3.2) remains constant over time for a constant shaft speed under ideal conditions. High-frequency components arise because of the slots on the stator and rotor core in a practical machine. The net flux through the loop also fluctuates with varying magnetic fields (rotating excitation fields) under non-ideal conditions - such as non-ideal DC source, field, and machine asymmetries.

This condition results in a time-varying net flux through loop "abcd" (surface on loop plane), and thus induces a voltage across the shaft. An example of a variation in the net flux over time occurs in the case of a non-uniform air gap. A traveling MMF wave is subjected to varying air-gap permeances, and results in an asymmetrical flux. The time-varying net flux through the area of the loop

induces a current in the loop, and thus a voltage is induced across "ad." The return path "bc" consists of a shaft-voltage sensor that measures the voltage across "a" (excitation end) and "d" (grounded-driven end) in the case of experimental measurement.

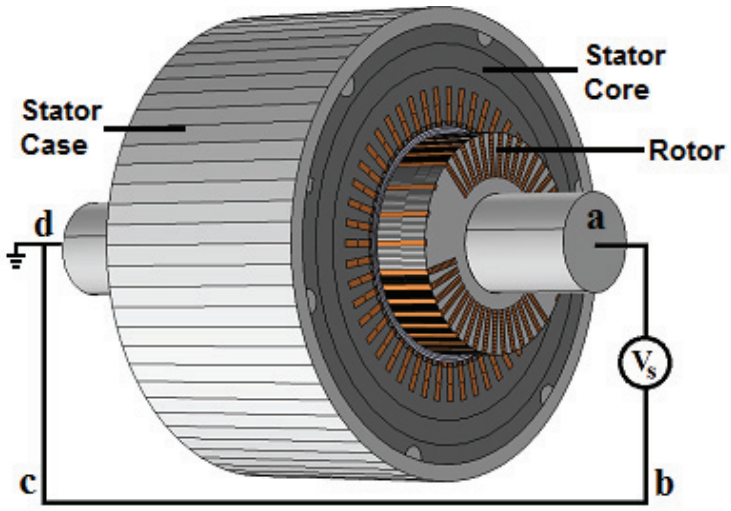


Figure 3.2: Shaft-voltage measurement loop on a synchronous generator - i.e. across length 'ad' where point 'd' is grounded

The presented concept for shaft voltages can be summarised analytically to simply imply the following:

$$V_S > 0 \; when \; \Delta\phi_{abcd} \neq 0 \; for \; \omega, \; I_f = constant \tag{3.1}$$

where ω and I_f are the angular speed and field-winding current of the machine, respectively. This concept is used to construct and implement a predictive model by employing FE methods.

3.3 Formulation of Predictive Model

An FE model of the experimental generator (figure 3.3, below) is constructed for this investigation. The model is designed for both transient and steady-state magnetic applications and enables coupling with an external electric circuit. The induced currents - along with the skin and proximity effects in conducting regions

- can be accommodated as necessary. Only the steady-state solution is considered for the purpose of the present investigation. The solution to the magnetic problem is obtained by using Maxwell's equations combined with the constitutive formulae for the matter.

The governing electromagnetic field equations used for the model (where state variables are time dependent) are listed as follows [85]:

$$\nabla \times \vec{E} = -\frac{\partial}{\partial t}\vec{B} \tag{3.2}$$

$$\nabla . \vec{B} = 0 \tag{3.3}$$

$$\nabla \times \vec{H} = \vec{J} \tag{3.4}$$

where E is the electric field intensity (V/m), B is the magnetic flux density (T), H is the magnetic field intensity (A/m), and J is the current density (A/m^2). The constitutive laws are also given by equations 3.5 and 3.6 as follows:

$$\vec{J} = \sigma \vec{E} \tag{3.5}$$

$$\vec{B} = \mu \vec{H} \tag{3.6}$$

where σ and μ are the electrical conductivity $(\Omega^{-1}m^{-1})$ and the magnetic permeability (H/m) of the material, respectively. The given Maxwell-Faraday relation, which may be represented by equation 3.7, implies the presence of an electric scalar potential Φ_E and, in this case, the unknown magnetic vector potential A.

$$\vec{E} = -\frac{\partial}{\partial t}\vec{A} - \nabla . \Phi_E \tag{3.7}$$

A 2D plane model is suitable for this investigation. However, certain assumptions for the 2D FE are intrinsic, such as magnetic field direction, current flow, and equal

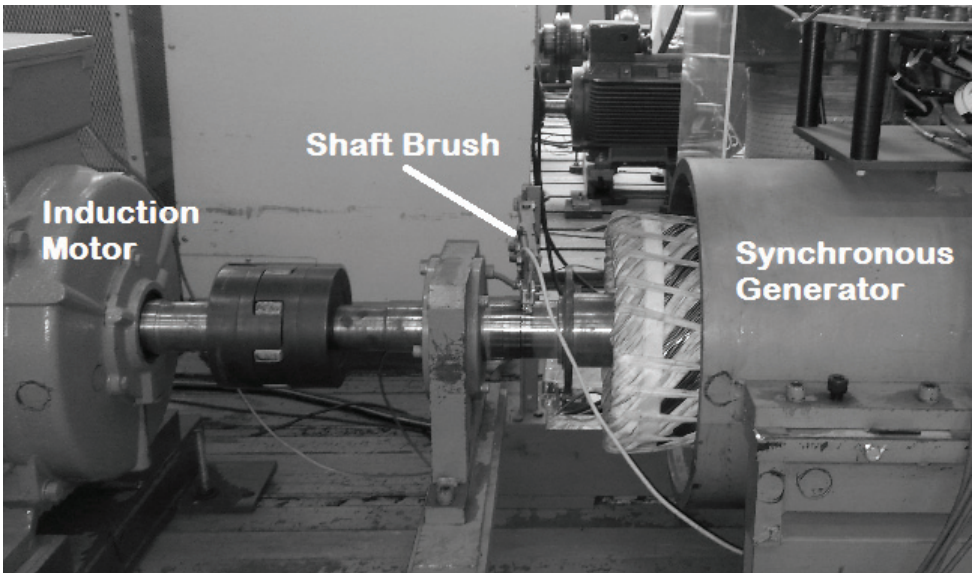


Figure 3.3: Experimental setup with induction motor (prime mover) shaft brush and synchronous generator

length of the stator and rotor cores. The geometrical parameters are given in table A.1 in Appendix A - which includes additional details of the FE model such as the geometry and mesh. Figure 3.4 (below) shows the modelled 2D geometry, which illustrates the flux path at rotor position $\theta = 0°$ - of the generator used in this investigation. The magnetic flux travels through the rotor, air gap, and stator. The first step in obtaining the time-varying net flux is to consider path "AB", which corresponds to path "ab" shown in figure 3.2. The 2D case assumes that the machine is axially uniform, which inherently implies that the surface created by the loop is uniform along the length of the machine for an instant.

This condition allows the calculation of the net flux across a surface "ABCD" as an approximation of the actual loop "abcd" - by considering the flux density over path "AB" and applying this throughout the length of the machine - that is, axial symmetry. Considering path "AB", the net instantaneous flux (Wb/m) may be computed by integrating the flux density (normal to the path) from points "A" to "B", as shown in equation 3.8. Figure 3.5 (below) shows the flux density along path "AB".

$$\phi_{AB} = \int_{A}^{B} \vec{B}_{\perp} dx \tag{3.8}$$

The magnetic flux densities shown in figure 3.5 are recorded under normal conditions at $3000\,rpm$ - with an excitation current of $40\,A$. The integral given in equation 3.8 is simply multiplied by the length (L) of the machine given in equation 3.9, to obtain the actual net flux (Wb) through the surface corresponding to the 2D path "AB". Figure 3.6 (below) illustrates the complete process for shaft-voltage computation.

$$\phi_{ABCD} = L \int_{A}^{B} \vec{B}_{\perp} dx \tag{3.9}$$

The net-flux integral is expected to be constant over time for an ideal machine. However, the net flux given by this integral does not remain constant over time for a practical machine with a slotted stator and rotor. The instantaneous net flux is calculated at $1\,ms$ intervals with a rotor displacement of approximately 18° over a certain period, by using the process shown in figure 3.6.

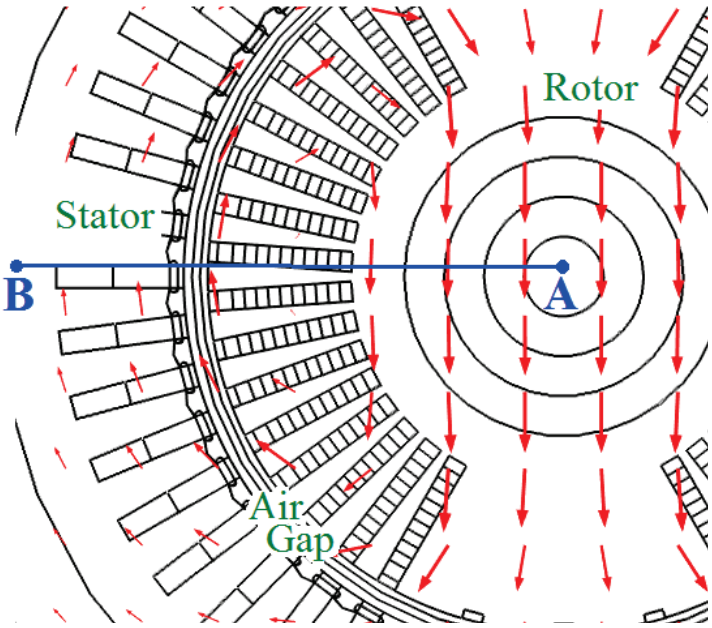


Figure 3.4: Geometry and cross-sectional front-view of 2-D FE model of synchronous generator, illustrating path length "AB"

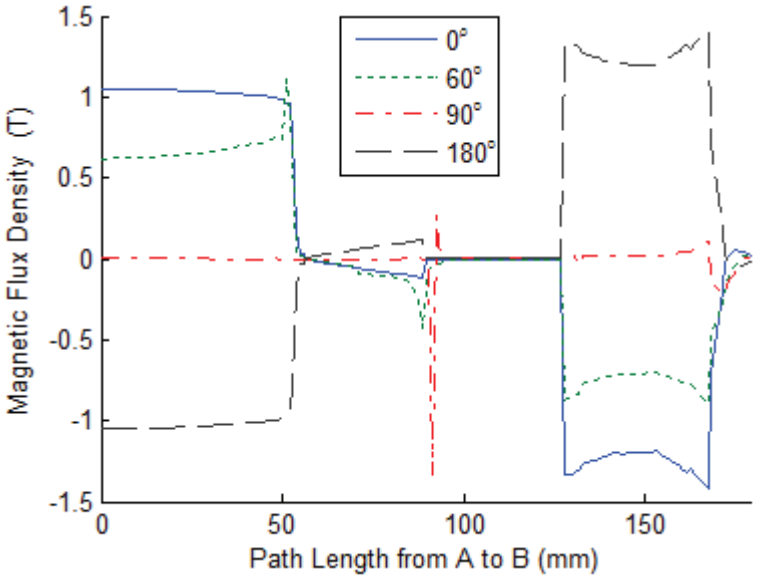


Figure 3.5: Numerical solution of magnetic flux densities, at various rotor positions over path "AB" (as shown in figure 3.4)

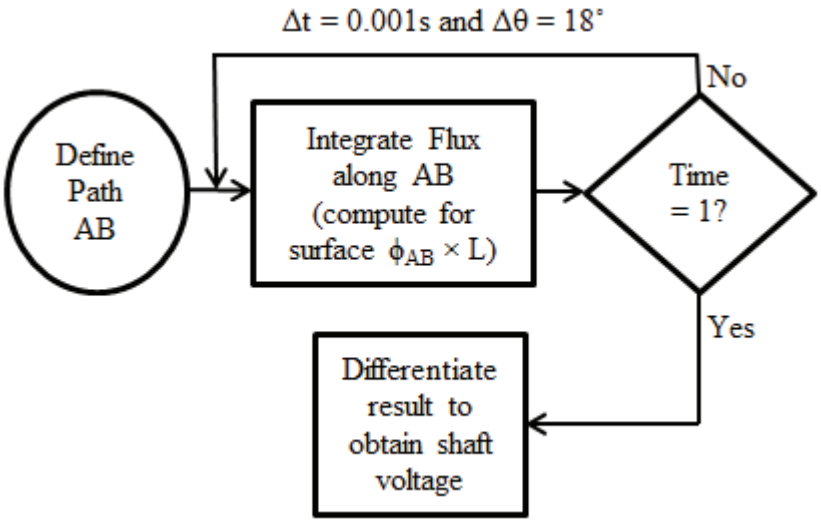


Figure 3.6: Process flow diagram describing methodology utilised for obtaining numerical solution of shaft voltage

This condition allows for a steady-state stepped computation of the instantaneous net flux. The peak flux density is $1.39\,T$, as shown in figure 3.5, and the total flux is computed by iterating this process several times (for example, a waveform of a $1\,s$ interval length will require 1000 iterations).

Equation 3.1 describes how the change in this resultant flux over the observation period is essentially the expected shaft voltage. The voltage induced within the loop "ABCD" is obtained by simply computing the flux linkage and its time derivative as provided by Faraday's law in equations 3.10 and 3.11, as follows:

$$\Phi_{ABCD} = N\phi_{ABCD} \tag{3.10}$$

$$V_S = -\frac{d}{dt}\Phi_{ABCD} \tag{3.11}$$

N is defined as the relevant number of turns and indicates unity in the case of a solid shaft in the expression given in equation 3.10. The net instantaneous flux and shaft-voltage waveforms obtained by using the presented numerical method under normal operating conditions, without a load, are shown in figure 3.7 (below).

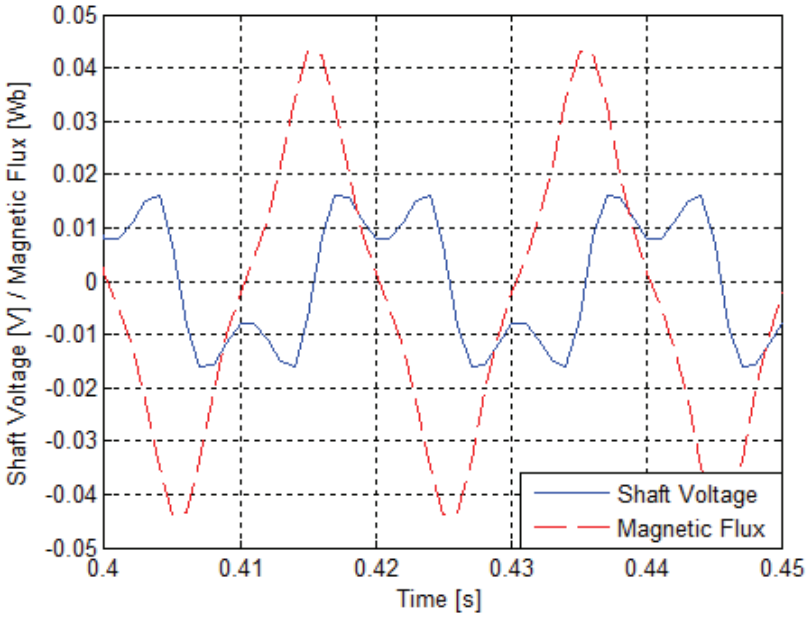


Figure 3.7: Shaft voltage and corresponding flux waveforms under normal no-load conditions obtained using the predictive model

3.4 Testing and Application of Predictive Model

3.4.1 Theoretical Substantiation

The validity of the presented model is first investigated by verifying if model behaviour complies with theoretical conceptualisation. The primary assumption that the shaft voltage is approximately zero under ideal conditions, must be investigated. This implies that the instantaneous net flux through the stipulated surface should be approximately zero, and thus that it remains constant over time. This assumption is verified by examination of the net flux behaviour over path "AB" (figure 3.4) - by eliminating individual non-ideal components of the model. The shaft voltage is obtained by using the presented methodology for different scenarios to diminish the complexity of the machine and to move toward an ideal machine scenario (that is, no voltage is induced on the shaft).

Table 3.1 (below) shows the results of this investigation. The first scenario models a practical machine with a non-uniform air gap (that is, static eccentricity with a positive vertical displacement of 5 % with respect to the air gap). Each scenario then removes a significant feature of the machine - such as stator case key way and weld recesses which introduce machine asymmetries. The final scenario has no slots on the rotor and stator. A linear permanent magnet rotor with unidirectional magnetisation is used to generate an ideal rotational field and to provide excitation.

Table 3.1: Shaft-voltage amplitude for diminished machine complexity and movement toward ideal conditions

Scenario Description	Shaft Voltage (mV)
All Features with static eccentricity	230
All Features of practical machine	160
No key way and weld recesses	130
Stator slots, key way and weld recesses removed	80
Key way, stator slots and rotor slots removed	30

The results indicate that a decreasing shaft voltage is removed as a practical feature of the machine, as expected in the presented model. The effects of diminishing

practical features are also not confined to a simple increase in the shaft-voltage amplitude but also affect the frequency characteristics of the signal. The shaft voltage recorded for the last scenario exhibits substantially lower levels and significantly reduced higher frequency harmonics than the practical machine scenario. The harmonics of the shaft voltage for each of the abovementioned scenario also show a definite trend for the $3rd$, $5th$, and $7th$ harmonics.

These high-frequency harmonics tend to decrease in magnitude as practical features of the machine are removed (that is, from the first to the final scenario). Static eccentricity exhibits a 19 % increase in the $6th$ harmonic relative to the practical machine scenario. Removing most practical machine features (that is, no key way, weld recesses as well as rotor and stator slots) affects the harmonics and results in decreases of 56 %, 81 %, and 79 % (relative to the second scenario or practical machine scenario) in the $3rd$, $5th$, and $7th$ harmonics, respectively. These results are significant for resolving some of the physical interpretation uncertainties with regard to variations in harmonics. The investigation also confirms that the model complies with the theoretical proposition for the origins of shaft voltages in synchronous generators.

3.4.2 Experimental Validation of Predictive Model

For protection purposes, prediction of the expected shaft-voltages levels is advantageous. However, with more frequent use of shaft voltages for machine health diagnostics, information on harmonic content of the phenomena is essential. This requires good accuracy for the modelled shaft voltage when compared to the experimental measurements. Hence, an analysis of the numerical results is conducted under laboratory conditions for this purpose. An experimental miniature generator (as shown in figure 3.3), and designed to mimic large turbo-generators, is used. The generator is a synchronous 2-pole machine rated at $20\,kVA$ and $3000\,rpm$ for an operational frequency of $50\,Hz$.

The experimental setup is fitted with flux probe and shaft voltage monitoring systems with the necessary preconditioning systems to eliminate noise and to cap-

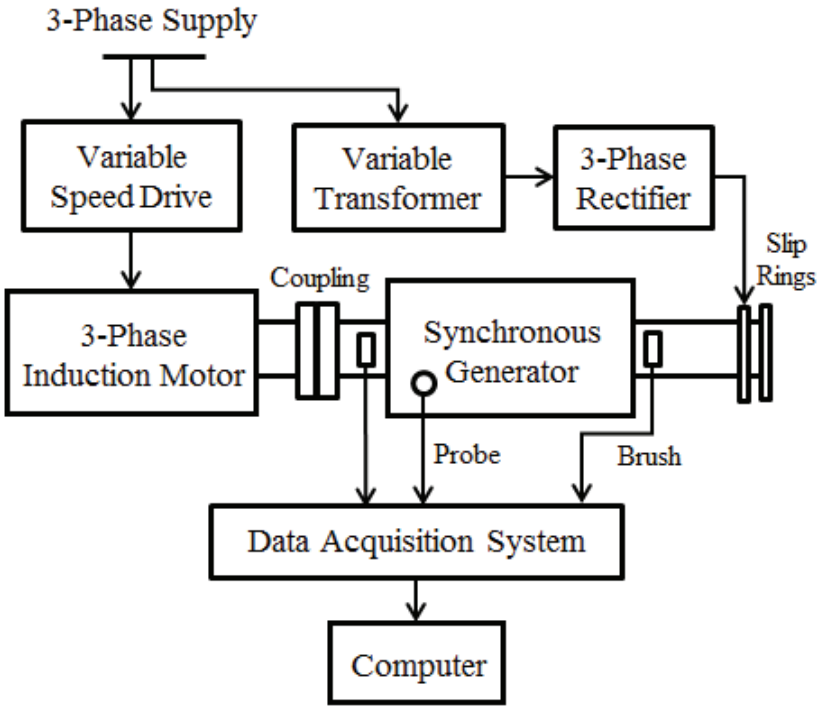


Figure 3.8: Experimental layout with instrumentation systems used to monitor and capture flux probe and shaft-voltage signals

ture signals. The flux probes are used in an investigation presented in chapter 4, where further details of this device are given.

The actual instrumentation used to monitor and capture shaft voltages consists of a data-acquisition system that is linked to the sensors of the pre-conditioning systems. Specialised silver-gold alloy brushes are placed on the finished landings on either side of the rotor shaft. The output of the brush device is fitted with anti-aliasing filters and connected to the analogue-to-digital inputs of the data-acquisition system. An overview of the experimental layout used during the investigation is shown in figure 3.8 (above). The experimental and simulated shaft voltages are shown in 3.9 (below).

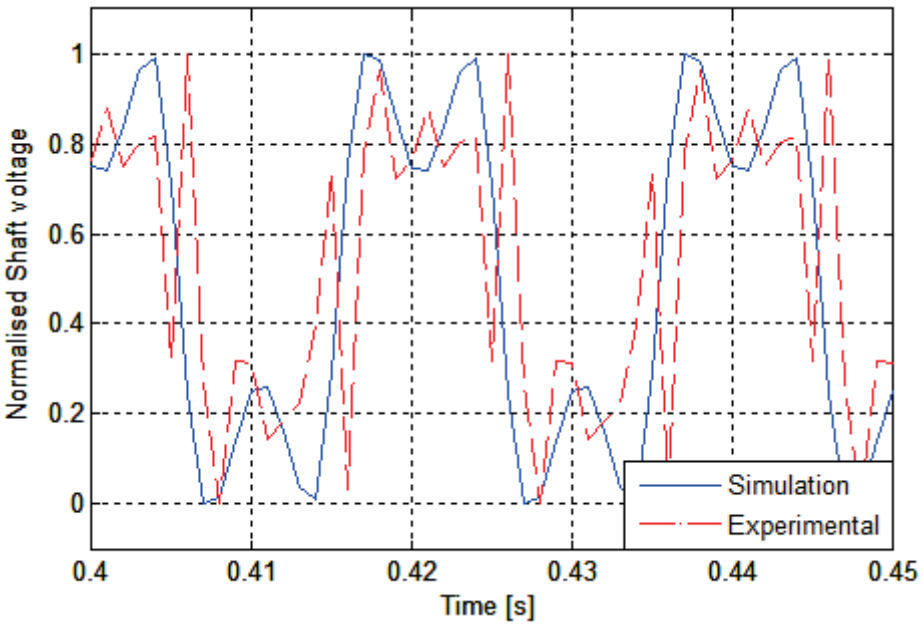


Figure 3.9: Experimental and modelled shaft-voltage waveforms obtained under normal no-load conditions

These waveforms are obtained under normal operating conditions ($50\,Hz$ at $3000\,rpm$) and $40\,A$ excitation current without load. Each signal is normalised by using the following relation for comparison:

$$Y(t) = \frac{Y - min(Y)}{max(Y) - min(Y)} \tag{3.12}$$

where Y is some arbitrary discrete set of real values. The signal is a periodic voltage with a fundamental frequency that corresponds to the expected machine speed. The peaks represent the rotor poles, and the ripples are caused by the rotor teeth/slots. The error (that is, the difference between the model and the experimental results) is estimated to validate the accuracy of the FE model. Total model error (E_T)for a particular number of samples (N), is given by the following:

$$E_T = ||X_S - X_E||^2 \tag{3.13}$$

where X_S and X_E are the simulated and measurement vectors, respectively. The average percentage error (E_{AVE}) of the model may be calculated as follows by

using the result from 3.13:

$$E_{AVE} = \left[\frac{E_T/N}{max(V_S) - min(V_S)}\right] \tag{3.14}$$

This equation yields a value of 15.95%. This value may be viewed as the sum total of the percentage error of the model and experimental uncertainty. The sources of this error are not precisely known, and are largely attributed to the unquantifiable physical characteristics of the machine and the measurement loop. However, the modelled signal content is mostly similar to that of the experimental content with regard to synchronism and predominant odd harmonics. Some minor differences are observed when comparing the harmonic content of the modelled and experimental signals (see figure 3.10, below). These differences occur because:

- Manufacturing tolerances of the experimental machine, such as core imperfections and rotor alignment, introduce relatively high nominal values - particularly for the $5th$ and $6th$ harmonics.
- The experimental $3rd$ harmonic is significantly high relative to its fundamental counterpart. This condition is mainly attributed to the peak-to-peak ripple on the rectified excitation source.
- The non-linearity of the magnetic material is more evident at higher currents than at lower currents due to saturation.
- The experimental $3rd$ harmonic is relatively higher than the modelled signal, because the model does not account for non-ideal DC excitation. The $3rd$ harmonic of the shaft voltage is attributed to the ripple produced by the three-phase rectifier. Moreover, it is inherently contained in the flux density wave of a practical machine [86].
- Rotor end windings and a mush-wound stator can also contribute to differences in the modelled shaft voltage, because these features are not part of the FE model.

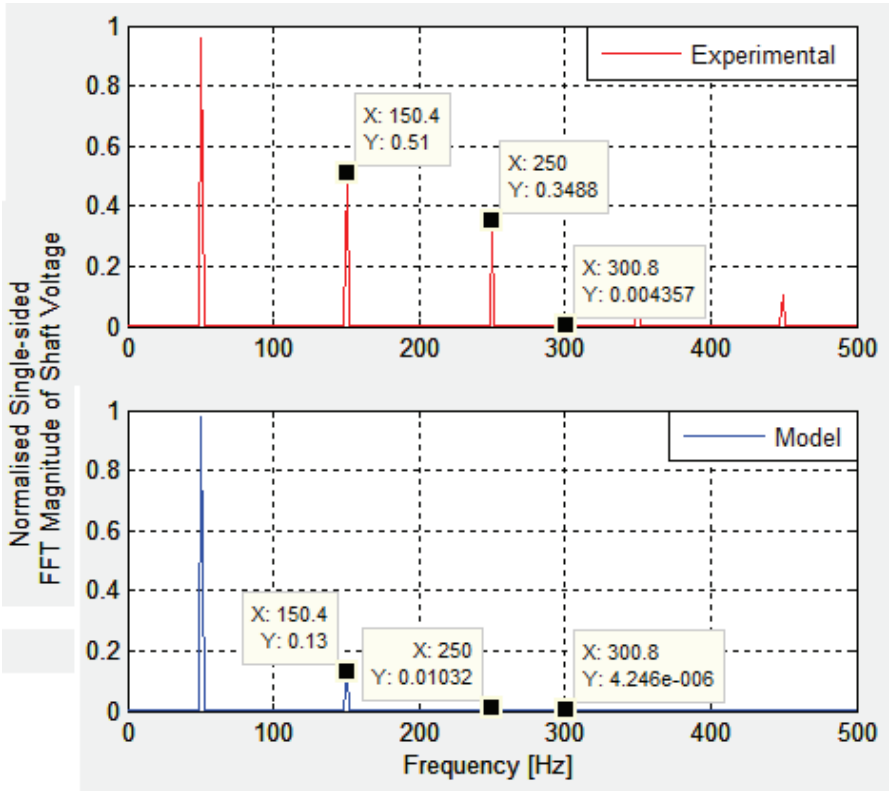


Figure 3.10: Frequency content of the experimental and modelled shaft-voltage signals under normal no-load conditions and 25 A field excitation

Non-linearity and the Third Harmonic:

The third harmonic of the shaft voltage is attributed to the ripple produced by the three-phase rectifier, and is also inherently contained in the flux-density wave of a practical machine [86]. Although anticipatory design of pitch and breadth factors of coils, and rotor slotting may reduce the third harmonic [87], other factors like magnetic non-linearity and operating regions of the machine influence the third harmonic. Experimental and modelled shaft voltages were obtained at various increments of excitation current. The resulting levels of the third harmonic for each scenario are given in figure 3.11.

These results show a similar growth rate for the third harmonic of both the experimental and modelled shaft voltages. Levels of this harmonic indicate a pattern inversely related to the material's magnetic flux density characteristics - i.e.

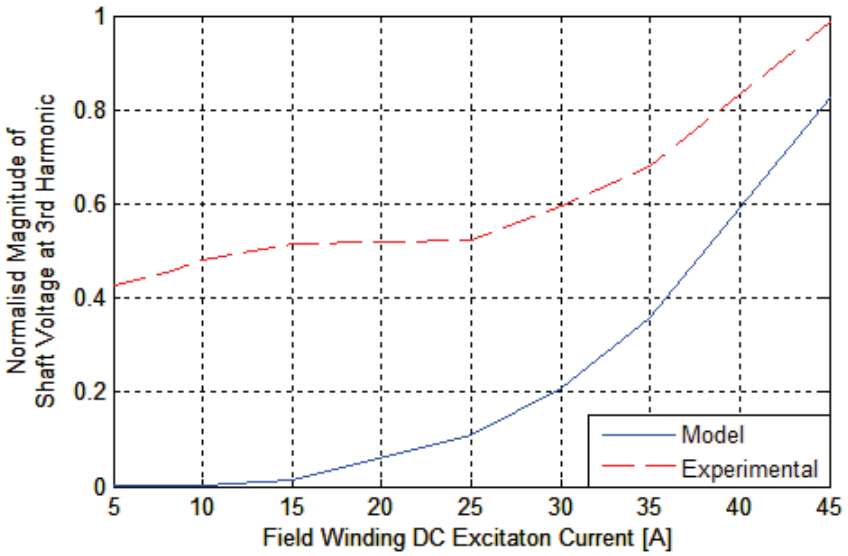


Figure 3.11: Comparison of third harmonic of FE model and experimental shaft voltages for different excitation currents on a synchronous generator

slower growth rate at lower currents and higher growth rate at higher currents. With the fundamental of the MMF, the well-known relationship is that given by a $B-H$ curve and has steadily increasing amplitude to the point of non-linearity and eventually saturation. The behaviour indicated here shows that the movement of machine operation into higher excitation currents and increased loads will cause an increase in the third harmonic of the shaft voltage. This behaviour corresponds to work conducted on induction machines [88], which showed an increase in the third harmonic of the MMF under saturation conditions. Physically, this result implies that at higher excitation currents the power begins to be transferred to the third harmonic and the fundamental's growth rate thus diminishes. The following information is inferred from this shaft-voltage characteristic:

- Observations on the relationship between the shaft voltage and MMF are enforced and validated.
- An initially higher third harmonic level of the experimental shaft voltage confirms the aforementioned influence of the rectifier peak-to-peak ripple and inherent tolerances on a practical machine.

In industrial applications, synchronous generators are subjected to fairly high loads. Fluctuations in the third harmonic of the resulting shaft voltages are therefore expected, especially under operation in non-linear regions.

End-Windings

The experimental generator consists of mush-wound stator windings and may contribute to the minor differences in the higher frequency harmonics between the modelled and experimental signal. Although the presented concept for shaft voltages includes the effects of end-windings, the 2D FE model does not account for such features. Typically, an industrial machine does not utilise mush-wound stator windings and is usually fitted with formed coils. Thus, the model does not require further examination of this feature. The rotor end-windings are a typical feature of industrial machines and are therefore investigated. The end-windings are situ-wound copper windings on the rotor core, which are used for field excitation. These windings are depicted in figure 3.12, where each loop represents 10 concentric windings which are stacked about the shaft and form overhangs. The end-windings lie within the loop "abcd" (shown in figure 3.2). However, these overhangs are not enclosed by the stator core and case. A large air-gap surrounds the end-windings and the overhangs are typically protected by a cowl. Simulation of a 2D FE model of the end-windings is carried out in order to investigate the effect of the resulting rotating field in the loop "abcd". The FE model consists of a cross-section which models the axial portion of the end-windings, surrounded by air and placed symmetrically about the rotor shaft. The shaft voltage - induced by the end-windings only - is determined using equations 3.9, 3.10 and 3.11, in the same process followed in the machine core volume. In this case, the axial length of the machine is replaced by the axial length of the end-windings.

The shaft-voltage waveform resulting from this simulation yields a peak amplitude of $1.56\,mV$ and is less than $1\,\%$ of the shaft-voltage amplitude produced by simulation of the core volume of the practical machine - i.e. $160\,mV$ as given in table 3.1 . This indicates that the end-windings account for a negligible percentage of the total voltage induced across the shaft. It should be noted this result

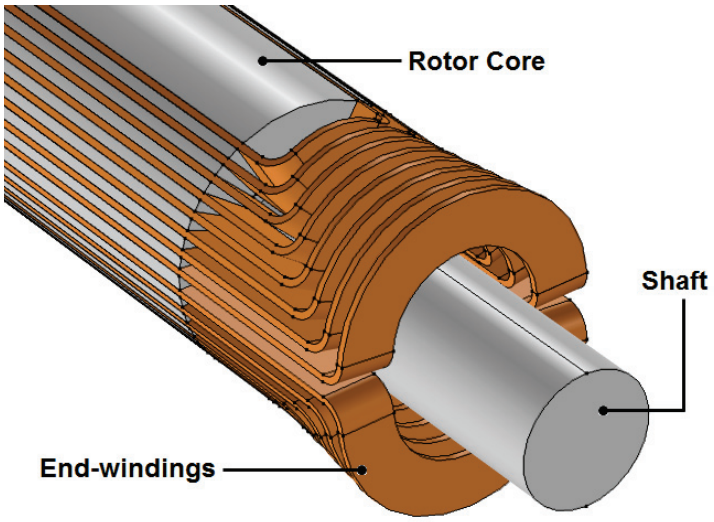


Figure 3.12: Rotor of the 2-pole synchronous generator depicting the end-winding configuration

cannot be added to the shaft voltage resulting from the main flux to improve overall accuracy because the principle of superposition does not hold here. However, the result does give a good approximation of the influence of the end-windings on the total shaft voltage. The signal waveform and harmonic content for the shaft voltage which results from specifically the end-windings of the machine are shown in figure 3.13 (below).

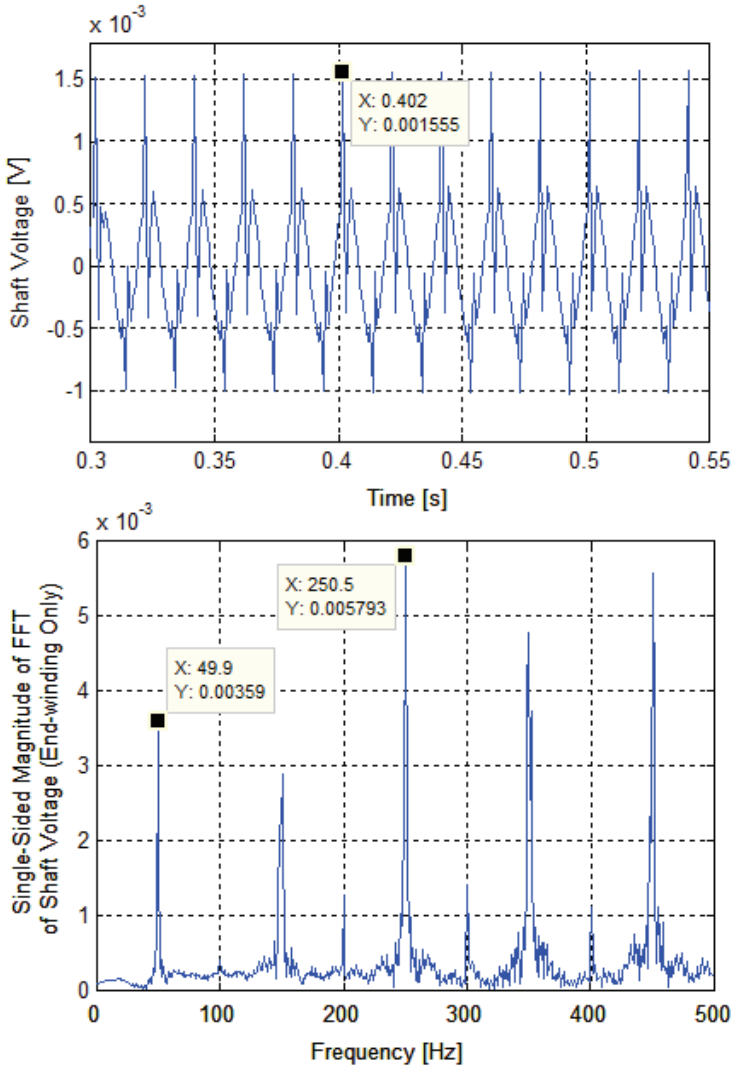


Figure 3.13: Shaft-voltage waveform and corresponding frequency spectrum resulting from FE simulation of rotor end-windings only

3.4.3 Application in Fault Diagnostics

Further testing of the predictive model is conducted in the context of an application. Model performance in this case is assessed for application in incipient fault diagnosis. The previously described experimental generator is also designed to accommodate eccentricity faults under controlled conditions. The stator is specifically designed to be repositioned relative to the rotor - which is placed on pedestal bearings - and thus allows implementation of static eccentricity.

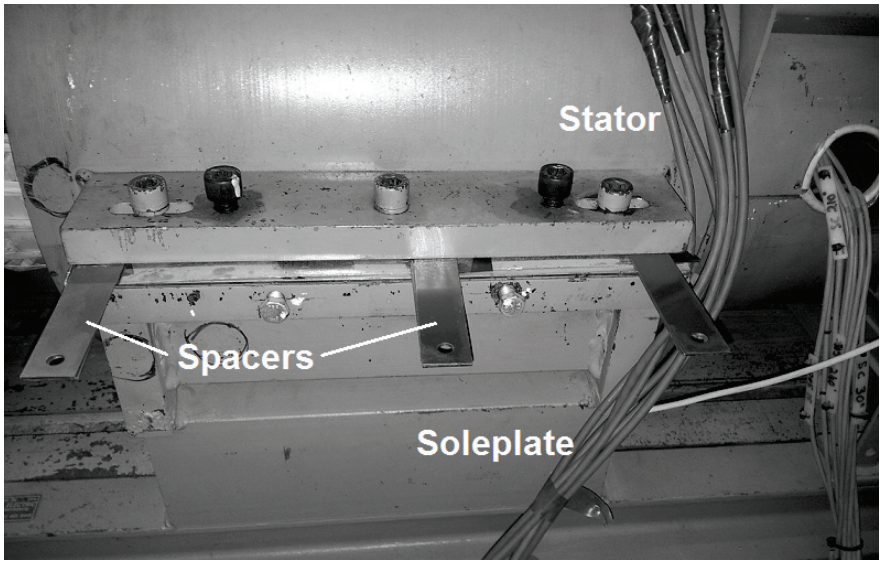


Figure 3.14: Experimental generator with spacers used to adjust stator position relative to rotor thus inducing a static eccentric fault

The machine stator is raised and $0.5\,mm$-thick spacers are used to fix the stator at the modified position to obtain a precise level - as shown in figure 3.14. This fault is also implemented on the predictive model, as described in Appendix A. The waveforms and corresponding FFTs obtained for the shaft voltage from the experimental measurements and model - under no load with an eccentricity fault of $0.5\,mm$ - are given in figures 3.15 and 3.16 (below). Some minor discrepancies are found mainly in the harmonic content, which is similar to the previous comparison of the normal operating model and the experimental signals. However, a substantially increased $6th$ harmonic is evident in both the modelled and experimental signals. The $6th$ harmonic ($300\,Hz$) is the frequency used to diagnose eccentricity faults with shaft voltages. This condition demonstrates the accuracy with which the model can predict the behaviour of the shaft voltage under fault conditions. The average percentage error (E_{AVE}) for the case of the aforementioned fault is calculated as $10.49\,\%$ through equations 3.13 and 3.14. Model performance is improved under fault conditions because the experimental generator has a default eccentricity level resulting from manufacturing and commissioning tolerances.

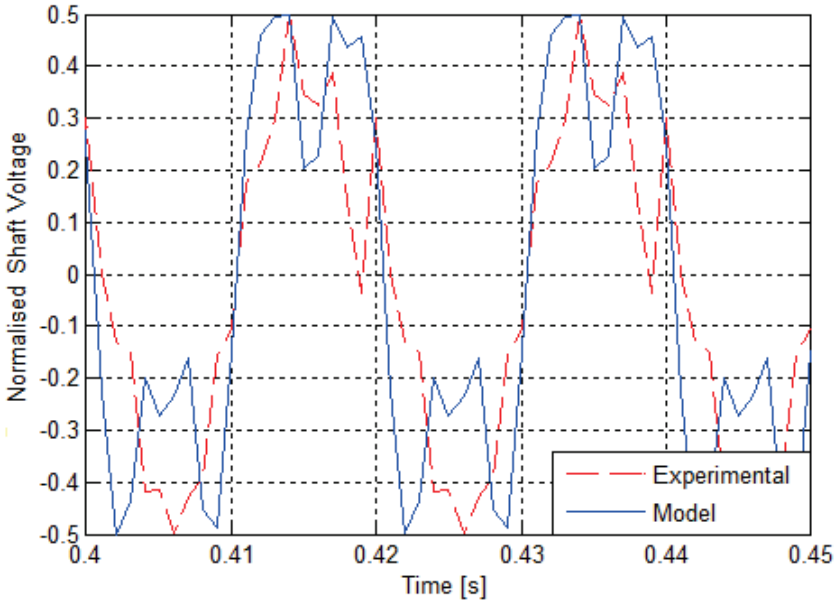


Figure 3.15: Experimental and modelled shaft-voltage waveforms under no-load conditions with 0.5 mm static eccentricity fault

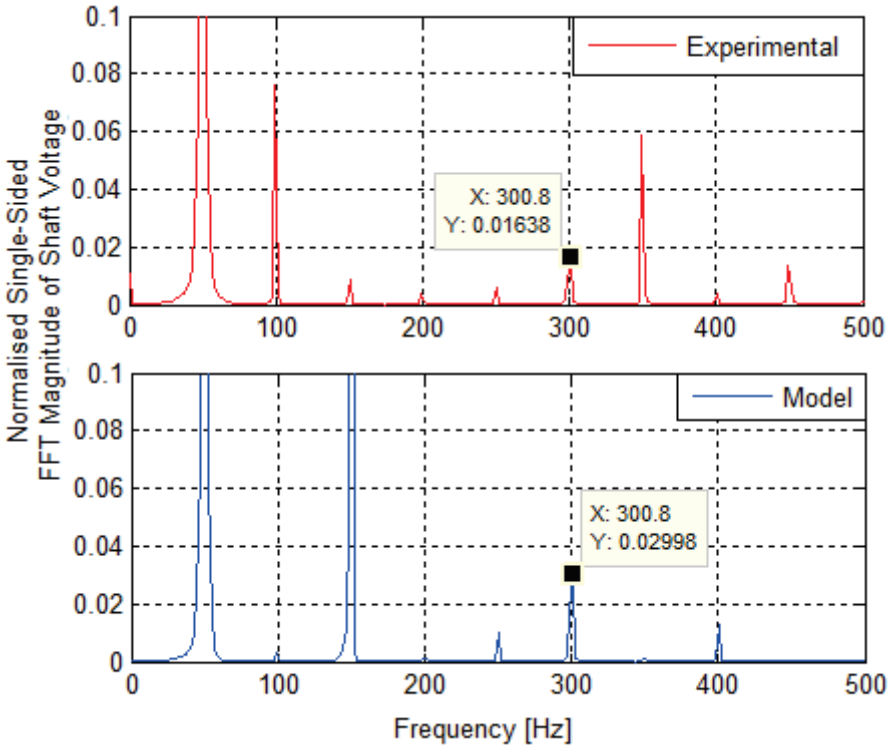


Figure 3.16: Frequency content of the experimental and modelled shaft-voltage signals under static eccentricity fault condition

3.5 Conclusion

In this chapter, a predictive model for shaft voltages in a synchronous generator is presented. An extensive investigation into previous models indicates that a suitable physical interpretation of this phenomenon is required. The availability of an accurate shaft-voltage model is significant from both protection and condition-monitoring perspectives. The model is derived by applying a semi-analytical approach and the shaft voltage is identified as a rate of change of the net flux through the specified loop and surface. Construction and implementation of the model is carried out using 2D FE methods.

An analysis of the model under varying degrees of machine complexity validates the theoretical model and physical interpretation of shaft-induced voltages. Testing the numerical solution for the shaft voltage under normal operating conditions, indicates good correlation with measurements obtained from an experimental generator. There are minor differences between the predicted and experimental waveforms which are attributed to specific insufficiencies inherent to the 2D FE model, and uncertainty in the experimental measurements. Results of further investigations indicate that the contribution of end-windings - in comparison to the core structure of the machine - to shaft voltages, is negligible. The model achieves good accuracy in predicting an incipient eccentricity fault. This demonstrates the suitability of the presented method for application in condition monitoring in synchronous generators. The model is thus considered valuable in describing previously uncertain characteristics and accurately predicting shaft voltages. Moreover, the model is suitable for testing and validating methods proposed in the chapters that follow.

Chapter 4

Uncertainty Analysis

4.1 Introduction

In chapter 2, a framework for developing condition-monitoring systems was presented. Within this framework, the main components of a modern system architecture were identified as the measurement modality, processing, and intelligence. In chapter 3, a model of the shaft voltages was developed, tested and validated. The framework and model are put into practice in the following chapters. In particular, in this chapter, the measurement modality is validated, and the processing and intelligence components are also specified.

The following section presents a method for selecting the optimal measurement modality. This selection method is used to qualitatively and quantitatively describe the merits of shaft voltage as a measurement modality. Thereafter, the uncertainty in fault diagnosis using shaft voltages is assessed to identify the requirements of a suitable intelligence subsystem.

4.2 Measurement Modality Selection using Cramér-Rao Lower Bound Technique

In chapter 2 it was described how condition-monitoring systems consist of a measurement modality. For example, numerous methods are available for the diagnosis of an eccentricity fault in rotating machines [89, 90, 91]. Each technique is based on measurements which have an associated accuracy and resolution. For diagnosis of an early eccentricity fault in a synchronous machine, some well-known techniques such as shaft voltage and magnetic flux measurements are available [45].

In practice, the identification process is critically dependent on the measurements used [92]. Therefore, the selection of the optimal measurement will ensure the accuracy of the eccentricity fault detection. This section aims at selecting the best measurement modality for diagnosis of static eccentricity fault - as described in section 2.3.2 of chapter 2 - in a synchronous generator. The Cramér-Rao lower bound (CRLB) technique is adopted to estimate the error on the identification of the eccentricity fault associated with shaft voltage and magnetic flux-based measure-

ment techniques. This method takes into account the effect of the measurement noise, as well as the uncertainty in some model parameters. First, a numerical analysis is performed and thereafter the results are validated experimentally by carrying out real measurements on a synchronous generator.

This investigation not only provides a method for selecting an optimal measurement modality, but more significantly allows for qualitative and quantitative evaluation of using shaft voltage as a measurement modality.

4.2.1 Symptoms of Eccentricity Faults

An eccentricity fault, in a cylindrical rotor synchronous machine, occurs due to a deviation in the rotor position relative to the stator and results in an asymmetrical air-gap. In synchronous generators, unbalanced magnetic pull occurs due to higher flux densities as pole centres pass the smaller air-gap. The altered flux distribution induces circulating currents in the rotor windings - resulting in higher losses. Additionally, an asymmetrical air gap can also produce a considerable increase in end fringing-flux, resulting in irregular local temperatures [93]. Several methods are available to detect eccentricity in synchronous generators. Some of these methods measure the resulting symptoms - e.g. vibration and circulating currents. Examples of other methods are shaft-voltage and magnetic-flux monitoring, which have been found to have exceptional fault diagnostic capabilities [8, 94] and are selected for the presented investigation.

4.2.2 Magnetic-Flux Monitoring

Numerous modern technologies which allow for online monitoring of the magnetic flux in the air gap. One of the earliest and most common methods is the use of a search coil/flux probe (hereafter referred to as flux probe). The method utilises a stationary coil fitted in the air gap of the machine - as first described in [95]. The actual coil is fitted in the air gap of the machine, fixed to the stator, and detects the radial or circumferential component of the magnetic flux (see figure 4.1 below). Some examples of the manner in which the technique is applied to fault diagnosis are:

- Capturing of differential voltages when more than one coil is used.
- Analysis of the variations of the coil voltage amplitude.
- Calculation and analysis of the flux directly from the measured voltage.
- Analysis of the signal harmonics in the frequency domain (also utilised in the presented research).

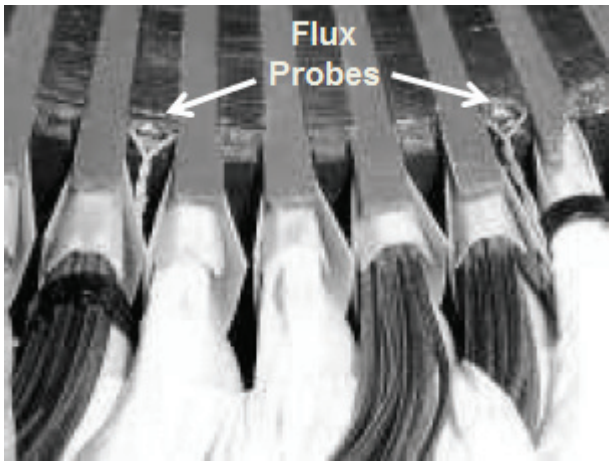


Figure 4.1: Picture of flux probes on the inner surface of the stator of the experimental generator

4.2.3 Methodology

The rotor eccentricity in rotating electrical machines can be identified by interpreting well-defined measurements via a mathematical model of the machine [96]. The accuracy of the identification process depends on the measured quantity being used. On the one hand, the measurement noise may largely influence the results. On the other hand, the sensitivity of the measured quantity on the eccentricity level may have a large impact on the identification results. Therefore, it is proposed that the Cramér-Rao lower bound (CRLB) stochastic technique - which is widely used in signal processing [97] and heat transfer applications [98] - be used here.

This technique has been recently used for estimating the error in the inverse

problem solution of magnetic material characterisation in different electromagnetic devices [99, 100]. In addition to the effect of the measurement noise, the identification procedure is significantly influenced by the ambiguous knowledge of some model parameters [101]. In rotating electrical machines, one of the most uncertain parameters is the one related to the magnetic material properties. The material properties of the magnetic core of rotating electrical machines are classically obtained by performing some standard measurements - e.g. Epstein frame measurements - on a separate electrical steel sheet of the material used inside the machine [102]. However, these standard measurements may not reflect the actual properties of the material that exists in the machine. In practice, the electrical steels are modified by mechanical and thermal stresses during the manufacturing process due to, *inter alia*, cutting, clamping, welding, and shrink fitting. These mechanical and thermal stresses often deteriorate the material behaviour [103].

Therefore, knowledge of the real magnetic material properties located in the machine are uncertain. The effect of such uncertainties on the accuracy of the eccentricity identification process needs to be estimated, and this can be done by adapting the classical CRLB approach. In the following subsection, the classical CRLB technique is briefly described. Thereafter, the adjusted CRLB technique is outlined in order to take the effect of uncertain model parameters - i.e. magnetic material characteristics - into account.

4.2.3.1 Classical Cramér-Rao lower bound technique

In the classical CRLB technique, it is assumed that the identification procedure is only affected by the accuracy of the measurements, while the machine model is assumed to be perfect - i.e. all physical phenomena are well described in the model. In other words, the uncertainty in magnetic material properties is not considered in this classical approach. In fact, the classical CRLB can be seen to be a kind of sensitivity analysis of the system response R to the sought-after parameter δ - which is the rotor eccentricity level in this investigation. Since the air-gap uncertainty level in not known in advance, the CRLB technique is used here as an *a priori* qualitative error estimation based on predefined values

for the *unknown* parameters. According to the Cramér-Rao inequality theorem, the covariance matrix of the lowest difference between the estimated and actual "predefined" parameter, is bounded by the inverse of the Fisher information matrix [104]. In other words, the lower bound of the variance of the unknown parameter σ_δ^2 is given by [105]:

$$\sigma_\delta^2 \geq FIM^{-1} \tag{4.1}$$

where FIM is the Fisher information matrix, which reduces to a scalar for one *unknown* parameter, and can be simplified as follows:

$$FIM = \frac{\partial R}{\partial \delta}^T S^{-1} \frac{\partial R}{\partial \delta} \tag{4.2}$$

where $\frac{\partial R}{\partial \delta}$ is the sensitivity of the model response R to the unknown parameter δ, and S is the variance of the noisy measured quantity, which is assumed to be Gaussian white distributed, with zero mean and a standard deviation of σ_n.

4.2.3.2 Adjusted Cramér-Rao lower bound technique

In order to study the effect of the uncertainties in some model parameters on the accuracy of the detected eccentricity level, the classical CRLB is modified. The adjusted CRLB technique calculates the extended Fisher information matrix ($EFIM$), by incorporating the total equivalent noise of the experiment - i.e. combined measurement and numerical noise, instead of the measurement noise in equation 4.2:

$$EFIM = \frac{\partial R}{\partial \delta}^T V^{-1} \mid \delta = const \frac{\partial R}{\partial \delta} \tag{4.3}$$

where V is the total equivalent noise of the experiment [106]:

$$V = \frac{\partial R}{\partial x}^T G \frac{\partial R}{\partial x} + S \tag{4.4}$$

where G is the variance of the uncertain model parameter, which is assumed to be normally distributed with mean value of μ_x, and a variance of σ_x^2. $\frac{\partial R}{\partial x}$ is the sensitivity of the model response R to the uncertain model parameter x. V needs to be calculated for a predefined value of the unknown parameter δ. Similarly, the lower bound of the variance of the unknown parameter σ_δ^2 in the adjusted CRLB approach is given in [107]:

$$\sigma_\delta^2 \geq EFIM^{-1} \tag{4.5}$$

4.2.3.3 Summary of methodology

Figure 4.2 (below) depicts the flowchart of the proposed methodology. In general, the proposed methodology is a combined experimental-numerical approach. The main part of the approach - in the case of the idealised model - is to calculate the sensitivity of the numerical model response that corresponds to the measurement modality of the unknown parameter - i.e. the eccentricity level $\frac{\partial R}{\partial \delta}$. Based on the measurement noise S, the lower bound of the variance of the recovered parameter σ_δ^2 can be computed. In the case of the uncertainty existence, the extended FIM needs to be calculated using $\frac{\partial R}{\partial \delta}$, $\frac{\partial R}{\partial x}$, and the total noise G to obtain σ_δ^2. The measurement modality with the lowest σ_δ is the best candidate for the static eccentricity diagnosis.

4.2.3.4 Mathematical modelling

The FE model - constructed in section 3.3 of chapter 3 - of the experimental generator is used for this investigation. For the shaft voltage, the flux path passes through the centre of the rotor core and encircles the stator frame. However, the flux probe loop encircles a stator tooth and therefore runs along the length of the machine. $N = 1$ is used for both cases, when calculating the induced voltage using Faraday's law (refer to equations 3.10 and 3.11).

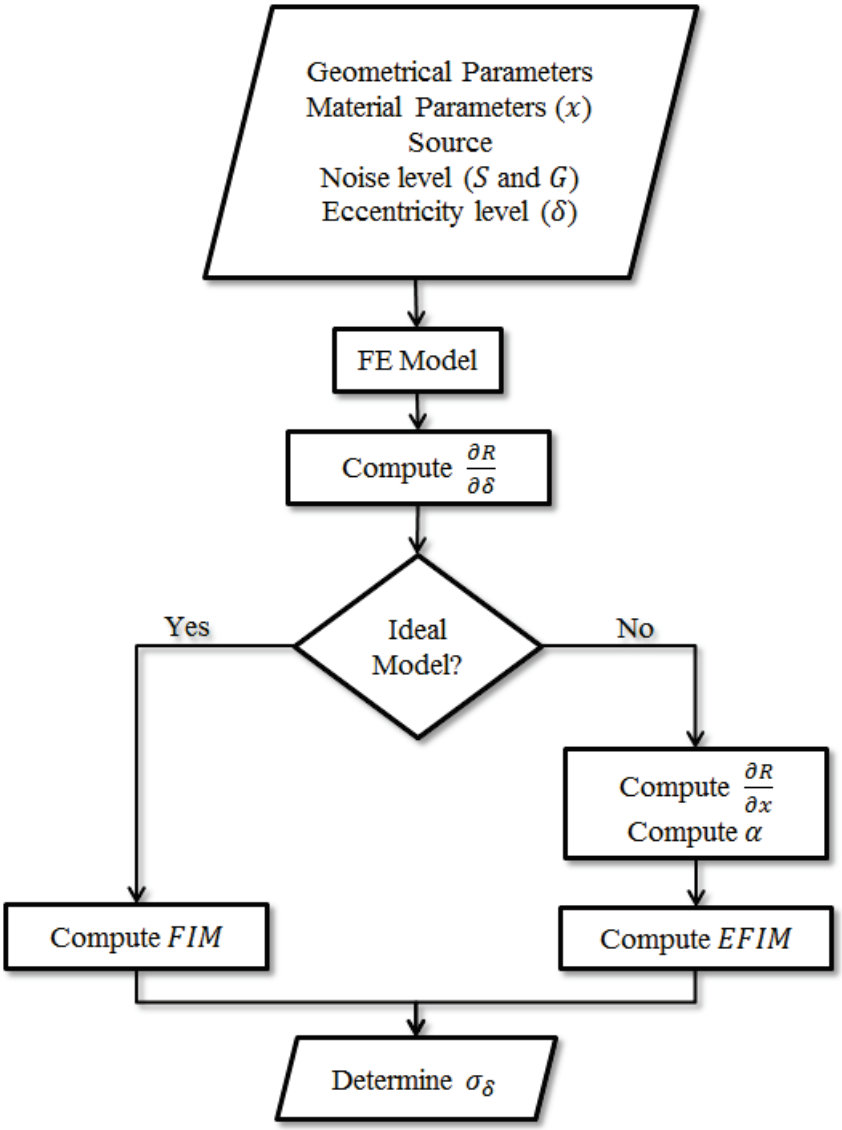


Figure 4.2: Flowchart of methodology for measurement modality selection using the CLRB technique

The magnetic properties - i.e. the single-valued nonlinear $B-H$ curve of the core material - which defines the magnetic permeability in equation 3.6, is modelled using the relation given by equation 4.6 [99]:

$$\frac{H}{H_0} = \frac{B}{B_0} + \left(\frac{B}{B_0}\right)^{\gamma} \tag{4.6}$$

where $\boldsymbol{x} = [H_0,\ B_0,\ \gamma]$ is the vector of magnetic material parameters. The initial magnetic permeability, and consequently the linear part of the nonlinear $B - H$ curve, is determined by the first two parameters. However, the latter parameter controls the slope of the saturation part. In fact, the machine used here has two magnetic materials. The first belongs to the stator core which is made of non-oriented laminated electrical steel sheets, and the other belongs to the rotor core, which is a non-laminated steel - i.e. machined from a solid bar.

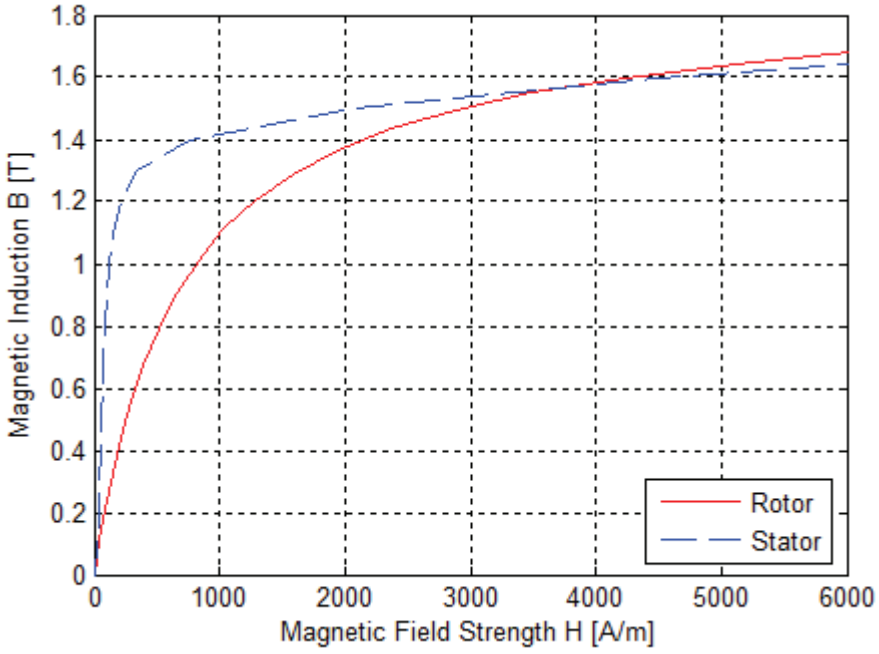


Figure 4.3: Nonlinear $B - H$ curves of the rotor and stator core (mean values)

The magnetic parameters of the magnetic core of the rotor are $\boldsymbol{x} = [406,\ 0.97,\ 3.8]$. Accurate knowledge of these parameters is not essential, since the rotor core constitutes a relatively small length of the magnetic circuit in comparison to the stator core. Moreover, the magnetic material parameters of the stator core are uncertain - with mean values $\mu_x = [170\,A/m,\ 1.3\,T,\ 16]$ and a standard deviation of $\sigma_x = [0,\ 0.2,\ 2]$. The effect of this uncertainty on the identification procedure is investigated in the following section. Figure 4.3 shows the $B - H$ curves of the stator (mean values) and rotor core materials.

4.2.4 Numerical Results

4.2.4.1 Idealised model

In this section, the uncertainty about the magnetic material parameters is not considered, and μ_x is utilised. Hence, the expected variance σ_δ^2 of the unknown parameter is calculated using equation 4.1, while $\frac{\partial R}{\partial \delta}$ in equation 4.2 is calculated using the finite-difference technique:

$$\frac{\partial R}{\partial \delta} = \frac{R(\delta + \triangle\delta) - R(\delta - \triangle\delta)}{2\triangle\delta} \tag{4.7}$$

Here, δ is the predefined value of the unknown air-gap eccentricity level, i.e. $0.6\,mm$, and $\triangle\delta$ is the step size which is chosen as 0.3. R is the simulated response using the 2D FE model presented in section 3.3, which corresponds to the shaft voltage and flux-probe voltage, respectively. $\frac{\partial R}{\partial \delta}$ does not depend on the value of δ and $\triangle\delta$ due to the linear dependence of the simulated response on the eccentricity in the considered region. Furthermore, it has been found that both measurements have a limited and approximately equal amount of noise. Therefore, in the following numerical results, the same value of the standard deviation of the measurement noise is assumed in both measurements - i.e. $\sigma_n = 0.1$.

Four numerical case studies have been performed. The first is related to no-load conditions, while the other case studies are done for different levels of a resistive loading - i.e. 4, 5, $6\,\Omega$ (or 0.7, 0.9, $1.07\,p.u.\,(\Omega)$, respectively). Figure 4.4 depicts the dependence of the shaft voltage and flux-probe voltage on various levels of the rotor eccentricity, at no-load conditions, for an excitation current of $40\,A$. For comparison, the shaft and flux-probe signals are normalised using equation 3.12.

Table 4.1 shows the values of σ_δ for the aforementioned case studies. Here, R is considered as the time-variant simulated quantity (samples). However, a similar trend is also observed when the sixth harmonic - i.e. $300\,Hz$ - is only considered in this computation, and which is discussed later in section 4.2.5. It is clear from the results shown in this table that the shaft voltage is a much more suitable measurement modality to detect the rotor eccentricity fault than the flux-probe voltage -

for the same measurement noise. In general, the error in the fault identification at load conditions is slightly higher than the one in the no-load condition.

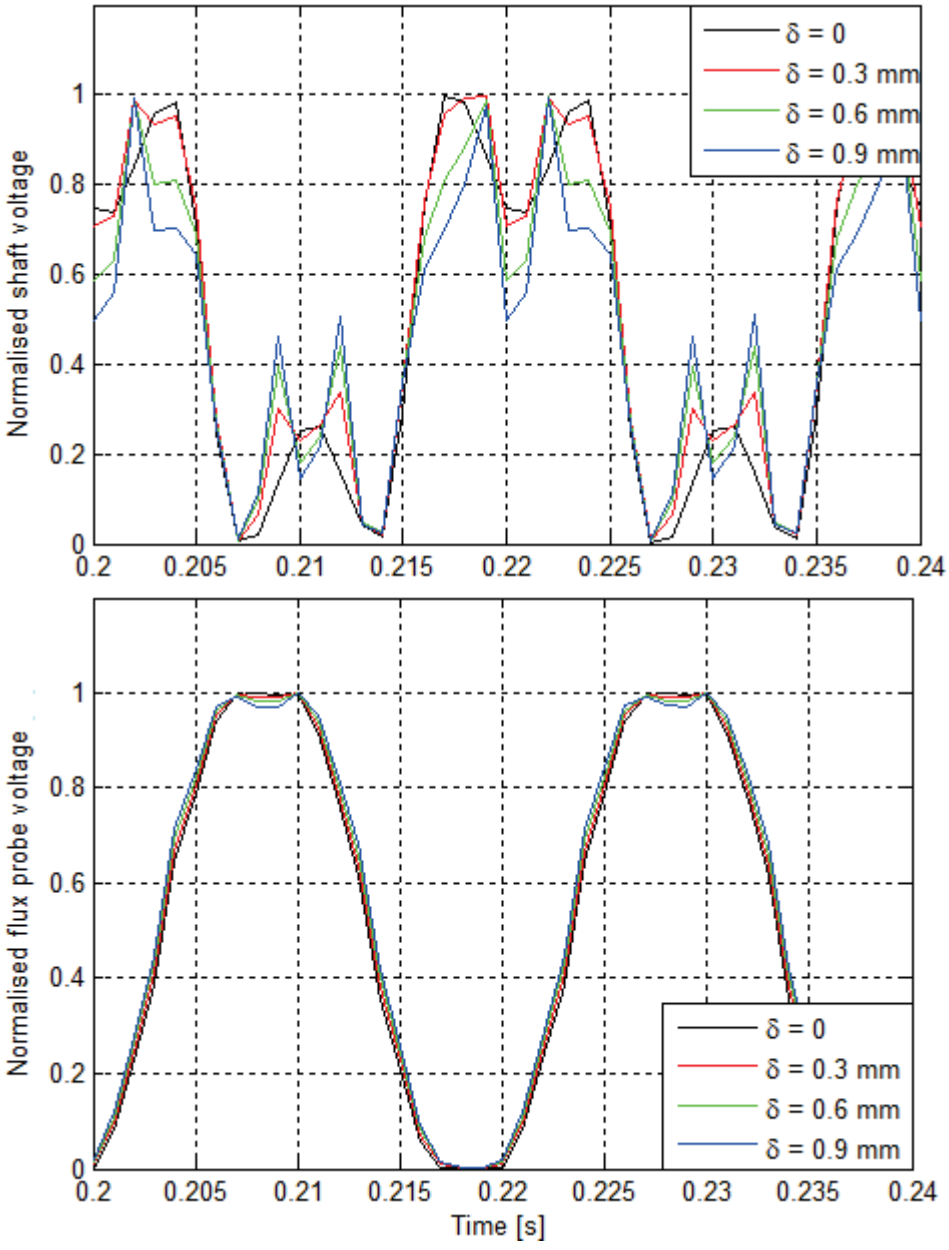


Figure 4.4: Normalised values of the simulated shaft and flux-probe voltage responses, for different eccentricity levels at no-load conditions

Table 4.1: Values of σ_δ for the two measurement modalities (no uncertain model parameters are considered)

	Shaft Voltage	Flux Probe Voltage
No-load	0.0907	0.4996
4Ω	0.1522	0.5558
5Ω	0.1398	0.5593
6Ω	0.1301	0.5614

4.2.4.2 Non-idealised model

In this section, the uncertainty in the magnetic material parameters is considered. Therefore, the expected variance of the unknown parameter σ_δ is calculated using equation 4.1. $\frac{\partial R}{\partial \delta}$ in equation 4.2, is calculated using the finite-difference technique - as shown in equation 4.7 - for a specific property of the magnetic material. Similarly, $\frac{\partial R}{\partial x}$ is calculated for a fixed eccentricity level as follows:

$$\frac{\partial R}{\partial x} = \frac{R(x + \triangle x) - R(x - \triangle x)}{2 \triangle x} \mid_{\delta - const} \tag{4.8}$$

Here, $\triangle x$ is chosen to be equal to σ_x. For simplicity, the numerical results are obtained for only one load condition - i.e. $5\,\Omega$, and one eccentricity level - i.e. $\delta = 0.6\,mm$. The effect of the uncertainty in the linear and saturation part is studied separately. The results of the effect of the uncertain magnetic material properties on the eccentricity identification, are given in Table 4.2.

These results indicate that there is no noticeable effect of the material uncertainties on the identification of rotor eccentricity with regard to the flux-probe measurement. In the case of the shaft voltage measurement, the identification error increases with the magnetic material uncertainties. The value of the identification error depends on the region of uncertainty in the $B - H$ curve, and can be approximately three times larger when the uncertainty originates at the linear part - i.e. uncertainty in parameter B_0. At saturation, the increase of the identification error becomes negligible. These results still show the superiority of the shaft voltage measurement modality over the flux-probe voltage - even with the uncer-

Table 4.2: Values of σ_δ for the two measurement modalities with uncertainty in the $B-H$ curve ($5\,\Omega$ load and $\delta = 0.6\,mm$)

	Shaft Voltage	Flux-Probe Voltage
No Uncertainty in $B-H$ Curve	0.1398	0.5593
Uncertainty in $B-H$ Curve (Linear Part)	0.4754	0.5651
Uncertainty in $B-H$ Curve (Saturation Part)	0.1427	0.5593

tainty in the $B-H$ curve. The fact that identification error becomes negligible for the shaft-voltage measurement at saturation conditions, is an important outcome of this analysis. This means that accurate knowledge of the saturation state of the magnetic material of the stator core will not affect the identification results. However, accurate knowledge of the initial permeability is required in order to obtain reliable results. These numerical results can be explained by considering the nature and origins of each of the measurement modes. Indeed, it is expected that the shaft voltage is more sensitive than the flux probe to variations in the magnetic properties of the stator. This is because the shaft-voltage loop holds the magnetic variations of the entire machine - i.e. including stator - while the probe is located in the air gap on the inner surface of the stator core.

4.2.5 Experimental Validation of CRLB Method

The experimental generator described in section 3.4.2 is used here to validate the presented modality selection method. For this specific investigation, two different levels of static eccentricity were selected. In order to obtain precisely these levels, the stator of the machine is raised and spacers (thickness $0.5\,mm$ and $1\,mm$) are then used to fix the stator at each of the modified positions - as previously shown in figure 3.14 in chapter 3. The instrumentation described in chapter 3 is used to capture both the shaft-voltage and flux-probe signals. The shaft-voltage sensors consist of the same specialised brushes and the probe contains a single turn copper conductor which is wound around a stator tooth.

The flux-probe signal is a periodic voltage with a fundamental frequency which corresponds to the speed of the machine as expected (see figure 4.5, below). The peaks represent the rotor poles and the ripples are due to the rotor teeth/slots. The experimental waveform of the flux probe is given with the simulated waveform, in order to validate the accuracy of the FE model in predicting the flux-probe voltage. The same procedure is repeated for the shaft voltage and is shown in figure 4.6 (below). Both measurements were conducted without a load. This comparison further validates the accuracy of the 2D FE model in simulating the shaft voltages and flux probe voltages of the experimental machine - but some differences appear. In relation to the reasons given in chapter 3, these differences can be explained for the following reasons:

- The asymmetries - due to manufacturing and commissioning tolerances - in the real machine are larger than those of the simulated machine, which is constructed with a high numerical accuracy.
- Small air-gap dynamic and static eccentricities are present in the real machine, in addition to the induced static eccentricities [108].
- It is impossible to simulate perfectly some manufacturing features, such as weld recesses and key ways.
- End effects are ignored in the 2D FE model.
- In addition to the above points, the peaks shown in the experimental wave shape exhibit larger odd harmonics because, experimentally, the machine does not use a pure DC source for the excitation. A three-phase rectifier is used to supply a DC voltage to the field windings and it is expected that the ripple in the supply also contributes to these harmonics.

The accuracy of the model can be increased through the use of a 3D FE model, although this is a very expensive alternative. Even so, the level of details provided by the simulation model can never match the experimental machine due to the aforementioned tolerances. However, it is emphasised that the purpose of the model is to provide 'qualitative' and 'quantitative' information to select the most appropriate measurement technique to identify static eccentricity, and it is not used

to quantify the actual eccentricity level. Details about the effect of the numerical model accuracy on the results of the presented identification method can be found in [109].

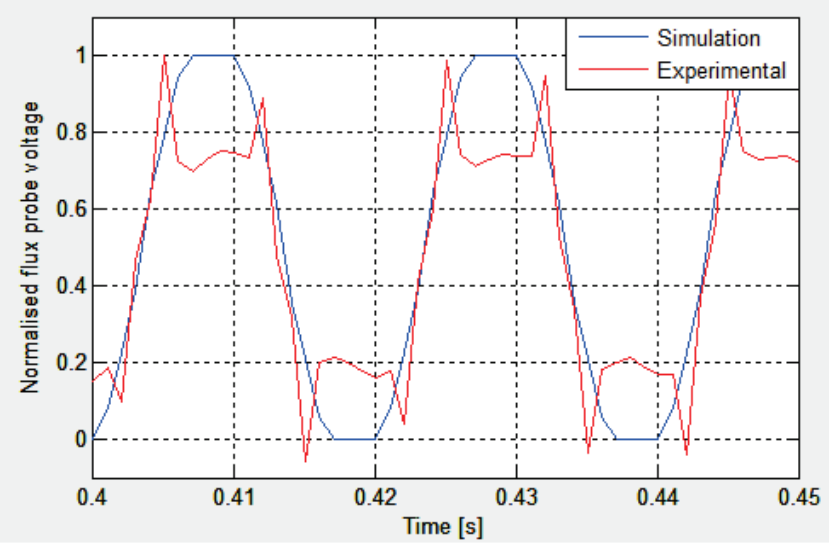


Figure 4.5: Normalised waveforms for flux-probe voltages under normal conditions for the simulated FE model and experimental generator

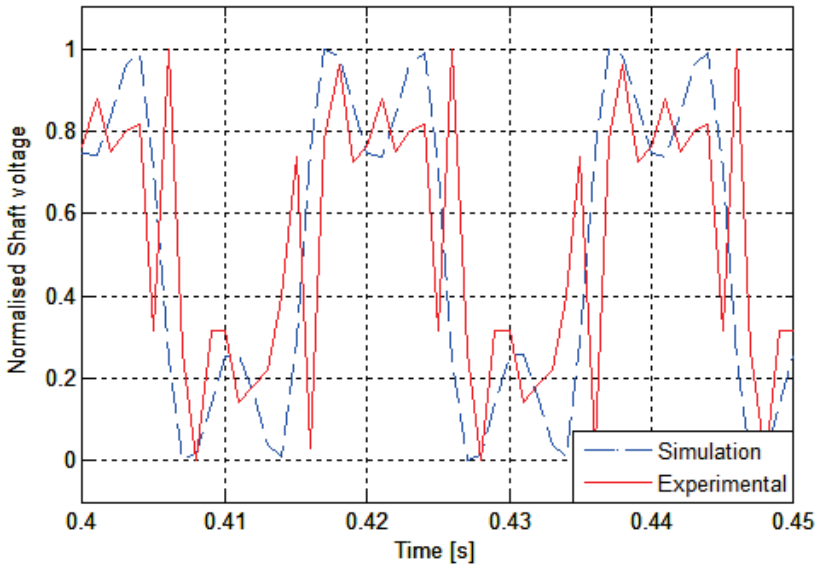


Figure 4.6: Normalised waveforms for shaft voltages, under normal conditions, for the simulated FE model and experimental generator

In order to validate the numerical results, the CRLB technique is performed using the experimental results at no-load and 5 Ω load conditions (see table 4.3). Here, only the sixth harmonic of the time-variant measured quantity is used in the CRLB calculation. The experimental cases of both the flux probe and shaft voltages are shown in figures 4.7 and 4.8 (below) - to indicate the influential frequencies. It is clear from these figures that there are several harmonic orders which exhibit significant changes due to the eccentricity variation.

Additionally, it is found that the $4th$ and $6th$ harmonic orders, in the case of the probe voltage, have monotonic variations that correspond to the increment in the eccentricity levels (see figure 4.8). However, for the shaft-voltage case, there are several harmonic orders that show such monotonic variation, such as $5th$, $6th$, and $8th$ harmonic orders (see figure 4.7). For the purpose of the comparison, the $6th$ harmonic order is used. Figure 4.7 shows that the amplitude of the shaft-voltage signal's $6th$ harmonic is more responsive than the flux-probe signal shown in figure 4.8, for increasing eccentricity levels. Results from the presented technique confirm this trend - both qualitatively and quantitatively.

Table 4.3: Comparison between the values of σ_δ, for the two measurement modalities, as given by numerical and experimental results

	Shaft Voltage	Flux-Probe Voltage
NL (numerical)	0.0001	0.1937
5 Ω (numerical)	0.0002	0.7831
NL (experimental)	0.0001	0.0047
5 Ω (experimental)	0.0004	0.7071

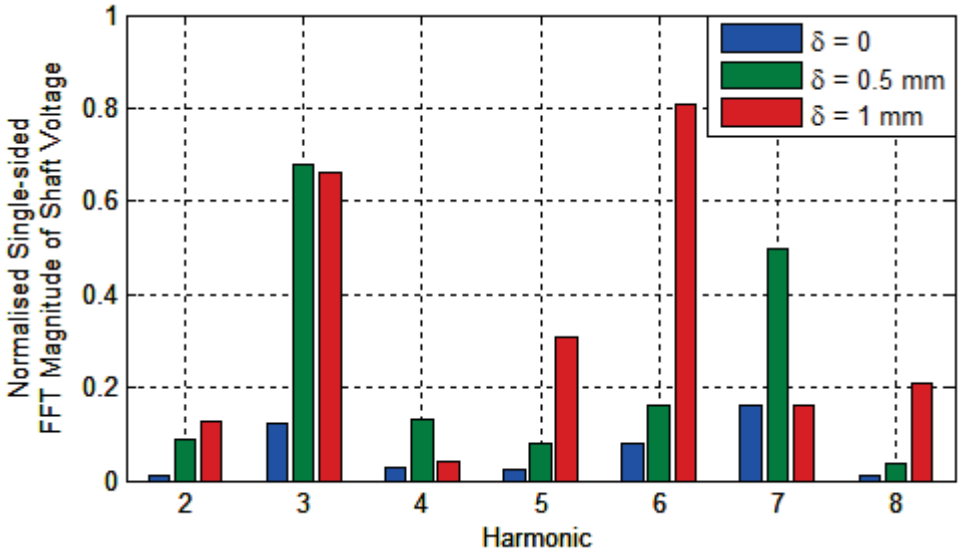


Figure 4.7: Bar chart indicating magnitudes of single-sided FFT of shaft voltages for different levels of eccentricity carried out in an experimental setting

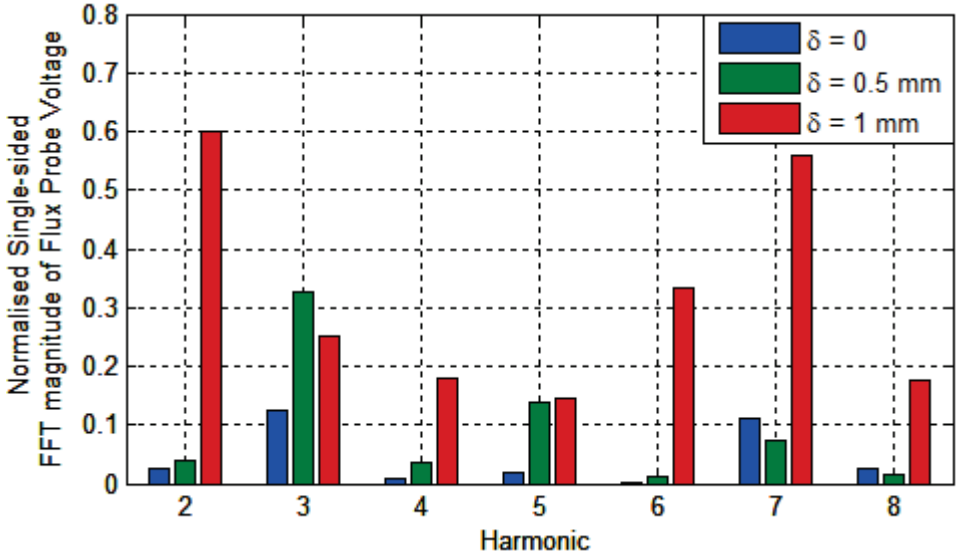


Figure 4.8: Bar chart indicating magnitudes of single-sided FFT of flux-probe voltages for different levels of eccentricity carried out in an experimental setting

4.3 Uncertainty in Fault Diagnosis

The presented CRLB technique and investigation of measurement modality confirms that shaft voltage is a good candidate for incipient fault diagnosis. However, there is an inherent uncertainty in the actual diagnostic method - which imposes limitations on the practical application of shaft-voltage-based condition monitoring. The uncertain elements and limiting factors are summarised as follows:

- While the periodogram of the shaft voltage is an effective diagnostic method, it may not be optimal with more advanced digital signal processing techniques which are now available.
- Interpretation of the data must be carried out manually by a specialist and is based completely on expert knowledge.
- Fault diagnosis on a machine depends on extensive expert experience and is therefore vulnerable to human error. Furthermore, the human expert must have extensive experience on the specific machine. In practice, operating conditions and shaft-voltage behaviour will vary from machine to machine.
- Large discrepancies in the signal spectrum of the shaft voltage, as shown by analysis of the monotonic variations in the previous section, can be used to assess the machine's health. More subtle variations and patterns in the data - caused by incipient faults - cannot be identified by a human being which renders the diagnosis non-optimal.
- Although shaft voltages are measured online, interpretation of the data and fault diagnosis can only be done offline. This process is inefficient and impractical in most plants, with a large number of machines in constant operation.

From the abovementioned points, a set of requirements are determined for developing a suitable fault-diagnosis subsystem.

4.3.1 Functional Requirements

The requirements of a fault diagnosis subsystem needed to improve the shaft-voltage-based condition-monitoring system, as follows:

- The subsystem must constantly work online and automatically diagnose faults.
- Optimum signal-processing techniques must be employed for best fault resolution, given the constraints of the measurement modality.
- Outputs must be suitably simplistic for non-expert users/operators to interpret.
- False alarms must be avoided.
- Must be adaptable for use on different 2-pole synchronous generators.
- The overall solution must be relatively inexpensive and easy to maintain. This affects the functional requirements as it excludes the use of ancillary equipment such as expensive instrumentation, mass storage devices and specialised modelling software.
- The physical subsystem must be non-invasive and retro-fittable. This allows for any supplementary measurement and processing devices to be fitted after the machine is commissioned, and does not modify the machine in any way.

These requirements are used to specify the design for the intelligence component of the shaft-voltage-based condition monitoring system.

4.3.2 Intelligence Component

The mathematical problem of fault diagnosis may be thought of as an unknown target function which outputs a fault assessment where the measurement modality - shaft voltage in this case - is the input. However, as with many practical problems, such a target function - some n^{th} order polynomial - is complex and cannot be determined. In general, machine learning provides tools for addressing this type of problem (see figure 4.9).

A machine-learning approach is adopted to meet the aforementioned requirements and to provide a fault-diagnosis solution. Essentially, a machine-learning algorithm can provide an approximation of the unknown target function to diagnose faults,

without defining a direct mathematical relation. This solution will also allow for the fault-diagnosis subsystem to be adapted to any 2-pole synchronous generator, as it does not require a machine model. However, a model or historical data may be used for training purposes.

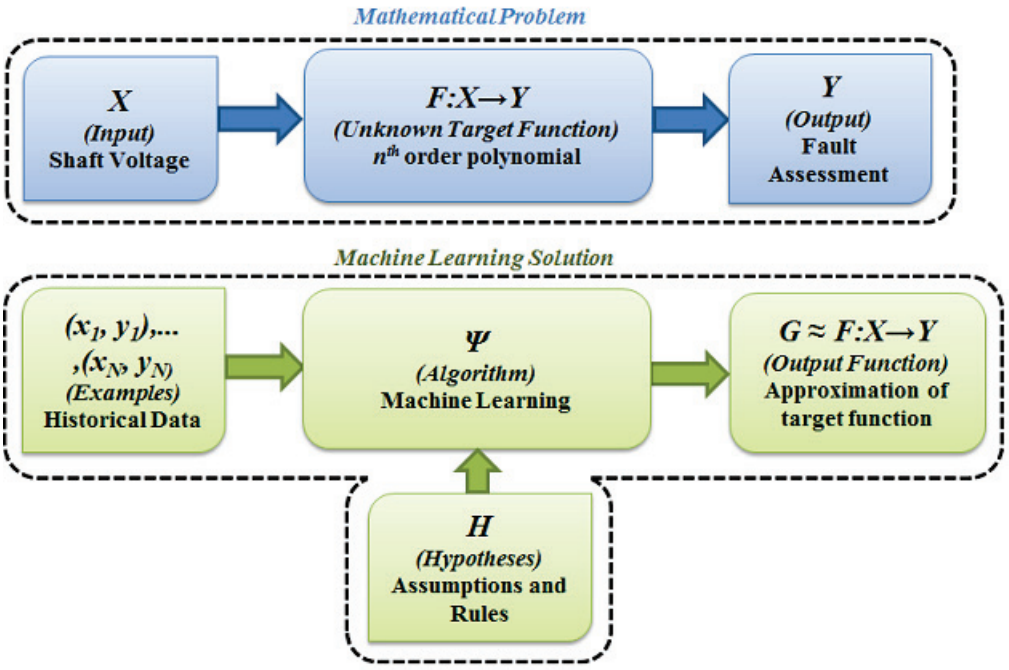


Figure 4.9: Machine-learning approach to approximating the mathematical target function of the fault-diagnosis subsystem

The proposed fault-diagnosis subsystem is designed to fulfill the aforementioned requirements, and consists of two main components. These components are a feature extraction algorithm and an automatic online fault classification algorithm. The extraction algorithm uses an optimal signal-processing technique which extracts features from the shaft-voltage signal. These features are then used by the fault classification algorithm to automatically assess the condition of the machine.

In order to enhance the overall efficiency of the condition-monitoring system, a fault-detection subsystem is designed to supplement the fault-diagnosis subsystem. The fault detection algorithm enables the condition monitoring system to operate online constantly and to avoid false alarms. These two subsystems form

the intelligence component of the shaft-voltage-based condition-monitoring system. The design, implementation and testing of the fault detection and fault diagnosis subsystems are presented in chapters 5 and 6, respectively.

4.4 Conclusion

In this chapter, the measurement modality is validated and the intelligence component of the condition-monitoring system is specified. The CRLB technique is used to determine the optimal measurement modality and to investigate the merits of applying shaft voltages in fault diagnosis. The investigation identifies and compares the accuracy of shaft voltages to a widely used measurement technique that uses flux probes to diagnose eccentricity faults on a synchronous generator. The classical CRLB technique was adjusted in order to deal with the measurement noise and the uncertainties in the magnetic material properties of the stator core. The 2D FE model and the experimental generator is used to validate the technique. The results of the investigation indicate that shaft voltages are more responsive to static eccentricity faults and provide a significantly lower identification error. Furthermore, it was shown that the shaft-voltage-based technique performs exceptionally well past linear operating regions, which is a desirable trait, especially in power-generation applications.

Additionally, the uncertainty and practical limitations of the current methods for diagnosing faults using shaft voltages are also analysed. Functional requirements are then derived to help specify the design for the fault-diagnosis subsystem. A machine-learning solution is determined to be the most suitable solution in terms of fulfilling the requirements of the intelligence component of the shaft-voltage-based condition-monitoring system. A supplementary fault-detection subsystem is also specified to enhance the overall efficiency - by providing constant online operation and avoidance of false alarms.

Chapter 5

Fault Detection with Principal Component Analysis

5.1 Introduction

The practical application of a predictive maintenance philosophy requires an online condition-monitoring system in a condition-based or reliability-centred asset-management context. Reliability, accuracy and efficiency of these online systems are critical to the seamless operation of machines in industry. This necessitates that the system be robust against noise and normal process variation - thus preventing false alarms. Additionally, the system should employ computationally inexpensive techniques with accurate incipient fault-detection capabilities.

Incipient fault diagnosis utilises advanced inferential techniques and usually requires an interpretation/analysis stage. For example, the diagnostic stage could involve the use of historical data, together with pattern recognition or model-based techniques, which may prove to be computationally expensive and, sometimes, impractical for online application. In this case it is more viable to utilise a system that may detect the fault without unnecessary iterations through data-intensive algorithms. The terms fault 'detection' and 'diagnosis' were distinguished in Chapter 2 as descriptions of systems which provide either pure detection of a fault or location and type thereof.

In order to improve the shaft-voltage-based condition-monitoring system, as an online tool, a fault-detection stage is employed. This stage allows detection of new incipient-fault events using shaft voltages, and is intended for continuous online operation. Principal component analysis (PCA) is used to optimise the anomaly identification algorithm. The purpose of the routine is to bypass redundant iterations of a possibly computationally expensive fault-diagnosis algorithm, and yet still provide accurate fault detection. Figure 5.1 shows a flowchart which simply illustrates the addition of the detection stage to the online condition-monitoring system of the machine.

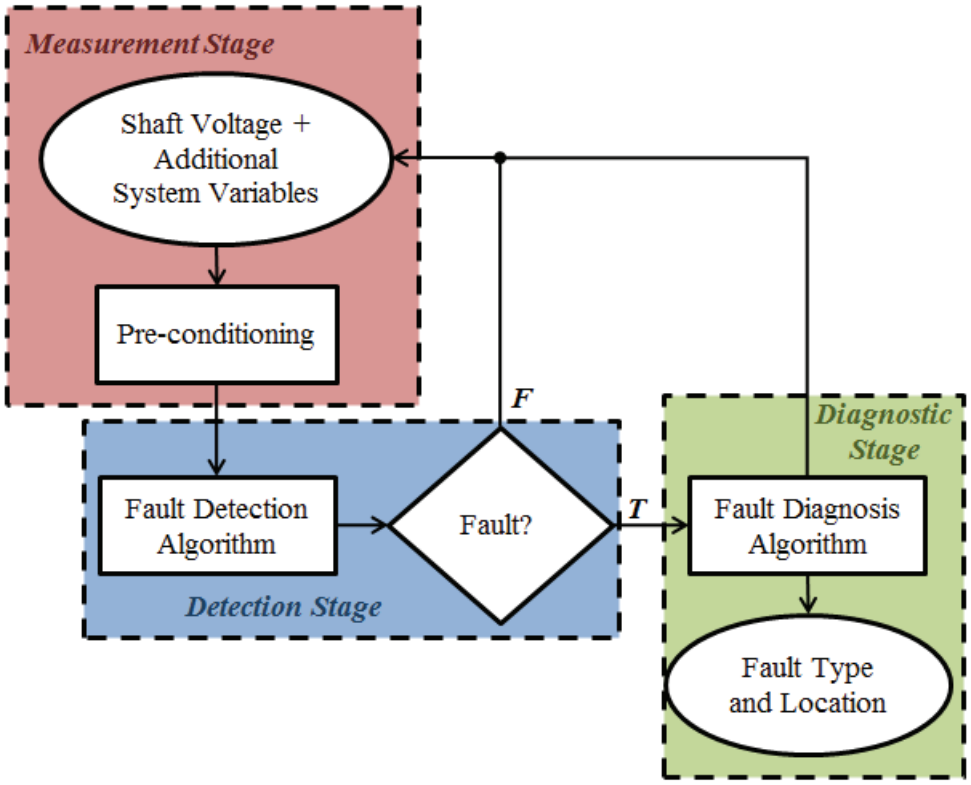


Figure 5.1: Flowchart with simplified illustration of stages for online condition monitoring on a synchronous generator

5.2 Fault-Detection System

5.2.1 Background: Principal Component Analysis

Principal Component Analysis (PCA) is a multivariate statistical technique. The purpose of PCA is to reduce the dimensionality of a data set - consisting of a large number of interrelated variables - while retaining as much as possible, the variation pattern. This is achieved by transforming the original set of measured data to a new set called the Principal Components (PCs). These PCs are uncorrelated and are ordered to retain most of the variation in all of the original variables [110].

There are various fields in which PCA is applied for the purpose of data compression and pattern analysis. Some examples of application, in biomedical engineering, are multichannel electrocardiogram (MECG), data compression [111]

and tissue conductivity prediction [112]. Other examples are found in image processing for noise level estimation [113] and optical tomography [113]. PCA, as a data-driven technique, is also utilised in plant process monitoring where model-based techniques require considerable effort to develop and impose computational expense [113, 114]. However, the benefits of PCA have also been recognised - with this method being adapted for fault detection in other areas like temperature sensing [115], power systems [116], and wireless sensor networks (WSNs) [117]. The PCA method is adapted here for the purpose of detecting abnormalities in a synchronous machine using shaft voltages.

5.2.2 Construction of Principal Component Model

5.2.2.1 Classical principal component analysis

The PCA model is constructed using a dataset consisting of n samples/observations for each of m selected variables. The dataset may therefore be represented as matrix $X \in \Re^{n \times m}$. The selected variables are measured with different scales, and must therefore be normalised to zero mean (as shown in equations 5.1 and 5.2) and unit variance (as shown in equations 5.3 and 5.4):

$$\bar{X}(m) = \sum_{j=1}^{m} \frac{\sum_{i=1}^{n} X(i,j)}{n} \tag{5.1}$$

$$X(n,m) = \sum_{j=1}^{m} \sum_{i=1}^{n} \left\{ X(i,j) - \bar{X}(j) \right\} \tag{5.2}$$

$$\sigma_X(m) = \sum_{j=1}^{m} \sqrt{\frac{1}{n} \sum_{i=1}^{n} \left\{ X(i,j) - \bar{X}(j) \right\}^2} \tag{5.3}$$

$$X(n,m) = \sum_{j=1}^{m} \sum_{i=1}^{n} \{ X(i,j) / \sigma_X(j) \} \tag{5.4}$$

The covariance matrix of the data set is then calculated using equation 5.5:

$$C = \frac{1}{n-1} X^T X \tag{5.5}$$

Singular value decomposition (SVD) is performed on the covariance matrix (C) using equation 5.6:

$$C = \Upsilon \Lambda \Upsilon^T \tag{5.6}$$

where Λ is a diagonal vector containing the eigenvalues of C. The matrix Υ is the eigenvectors of C, and is termed the "loadings" or "coefficients" matrix. At this stage, k eigenvectors or columns of Υ may be selected (according to significance of contribution to the variation in the data set) - to obtain a reduced dimension loading matrix $P \in \Re^{m \times k}$. This allows for calculation of the "scores" matrix, given in equation 5.7, which is a representation of X in the principal component space:

$$Z = XP \tag{5.7}$$

There are several methods for dimension reduction and analysis using PCA - such as parallel analysis, SCREE procedure, cumulative percentage approach (CPV), and cross-validation [118]. For example, when the data set is extremely large, the SCREE procedure is a graphical method used for selecting the number of eigenvectors to retain - thus reducing the size of the matrix P without loss of critical information [110].

5.2.2.2 Modified principal component analysis

The presented fault detection technique uses a modified form of the aforementioned classical PCA method. Firstly, the following five parameters of the synchronous generator are selected for the PCA model:

- Shaft voltage V_S,
- Phase voltage V_A,
- Phase voltage V_B,
- Phase voltage V_C and

- Excitation current I_f.

The instantaneous values of the three phase voltages and excitation current are selected - together with the shaft voltage - for multiple reasons. In fact, it is common practice in condition-based maintenance to monitor multiple machine parameters. This is done to increase the reliability and accuracy of a detection system. For example, if the machine were to be suddenly loaded, the resulting response (for a specific parameter) could initiate a false alarm. In this case, although it has been shown that the shaft voltage has exceptional incipient fault-detection capability, a large shift in the operating conditions of the machine could result in a false alarm or unnecessary iterations of the diagnostic stage (as seen in figure 5.1). Using the stator voltages and the excitation current allows for variation in operating conditions to be recognised. These parameters, like shaft voltages, are also constantly available in a synchronous generator - even under no-load conditions - due to generation services requiring constant voltage operation. In addition to significant variation of the shaft voltage under static eccentricity, slight imbalances in the stator voltages are also expected to contribute to the detection of this fault.

For the presented implementation, the aforementioned dimension reduction techniques are not required, as all of the principal components are utilised. Instead, the reduction of the data-set dimension is inherently administered through use of the T^2 and Q statistics. The most significant modification of the traditional PCA is the use of prior information in the data set. The implemented algorithm (see Appendix B) uses a moving average in the data set - i.e. each current observation is converted to an average of prior observations. This modification is similar to dynamic principle component analysis (DPCA) [119, 120, 121], and provides the following functions in the presented application:

- Resilience to noise.
- Absorbs unexpected variations in parameters caused by transients in machine operation.
- Improves stability by buffering uncertainty in parameter measurement.

- A robust method for creating a PCA model using signal parameters which may display non-stationary behaviour - e.g. under normal operation, the non-ideal excitation current I_f is expected to exhibit non-stationary behaviour due to slight variation in supply and ripple inherent to the three-phase rectifier.

Once the PCA model is created, the algorithm uses the T^2 and Q statistics to isolate any variation caused by a fault.

5.2.3 T^2 and Q Statistics

In order to reduce computational effort and provide reliable fault detection, the T^2 and Q statistics are used. Essentially, the fault-detection algorithm reduces the entire original data set to a subset consisting of these two variables, which are then monitored [122]. The Hotelling T^2 statistic is univariate and represents the variation in the data set or PCA model [123, 124]. After the steps outlined in equations 5.1 to 5.7 are completed, this statistic may be evaluated for a new data set X_F (with possible fault condition) - where X is the historical data set for the machine under normal conditions, using equation 5.8:

$$T^2 = X_F^T P \Lambda^{-1} P^T X_F \tag{5.8}$$

The Q statistics are the residuals for new observations and are a measure of the prediction error of the model[125]. Essentially, this is used here as an additional measure of how new observations deviate from the PCA model. The residuals (r_F) are first calculated using equation 5.9, and thereafter the Q statistic is obtained using equation 5.10:

$$r_F = (\mathbf{I} - PP^T)X_F \tag{5.9}$$

$$Q = r_F^T r_F \tag{5.10}$$

where $\mathbf{I}$ is the appropriate sized identity matrix - i.e. the same as the loading matrix P.

5.2.4 Numerical Results

The modified PCA technique is first implemented and tested in Matlab (see Appendix B). T^2 and Q statistics are then calculated using data generated by the FE model of the considered synchronous generator (shown in figure 3.3). The algorithm and flowchart (see listing 5.1 and figure 5.2, below), are a summary of the steps implemented in the fault-detection system.

Listing 5.1: Main steps of online fault-detection algorithm using PCA

```
1 Read in machine parameters (Vs, Va, Vb, Vc and If)
2 Create matrix X
3 Standardise data - zero mean and unit variance
4 Compute PCA model
5 Calculate T2 and Q statistics and compare to normal
      data statistics (a priori - obtained offline)
```

The result of the comparison mentioned in the final step determines whether to call the fault-diagnosis algorithm (if a fault is indicated through significant variation) or to continue looping through the fault-detection algorithm (under normal conditions). It should be noted that "significant variation" is dependent on the specific machine variables used in the data set and operating conditions of the machine. For example, in some process control applications it is considered to be significant when the T^2 and Q statistics exceed a predetermined upper bound/limit - i.e. a confidence interval [126]. However, this is only effective when the variables of the PCA model are expected to remain relatively constant. Due to the types of variables used here and transients expected under normal operation, it is impractical to use such a confidence interval. Therefore, the means or averages of each of the T^2 and Q statistics are considered a better measure for fault detection for this particular application.

By monitoring the averages of these statistics, it is possible to avoid false alarms caused by fast transients and to emphasise any subtle drift in the PCA model

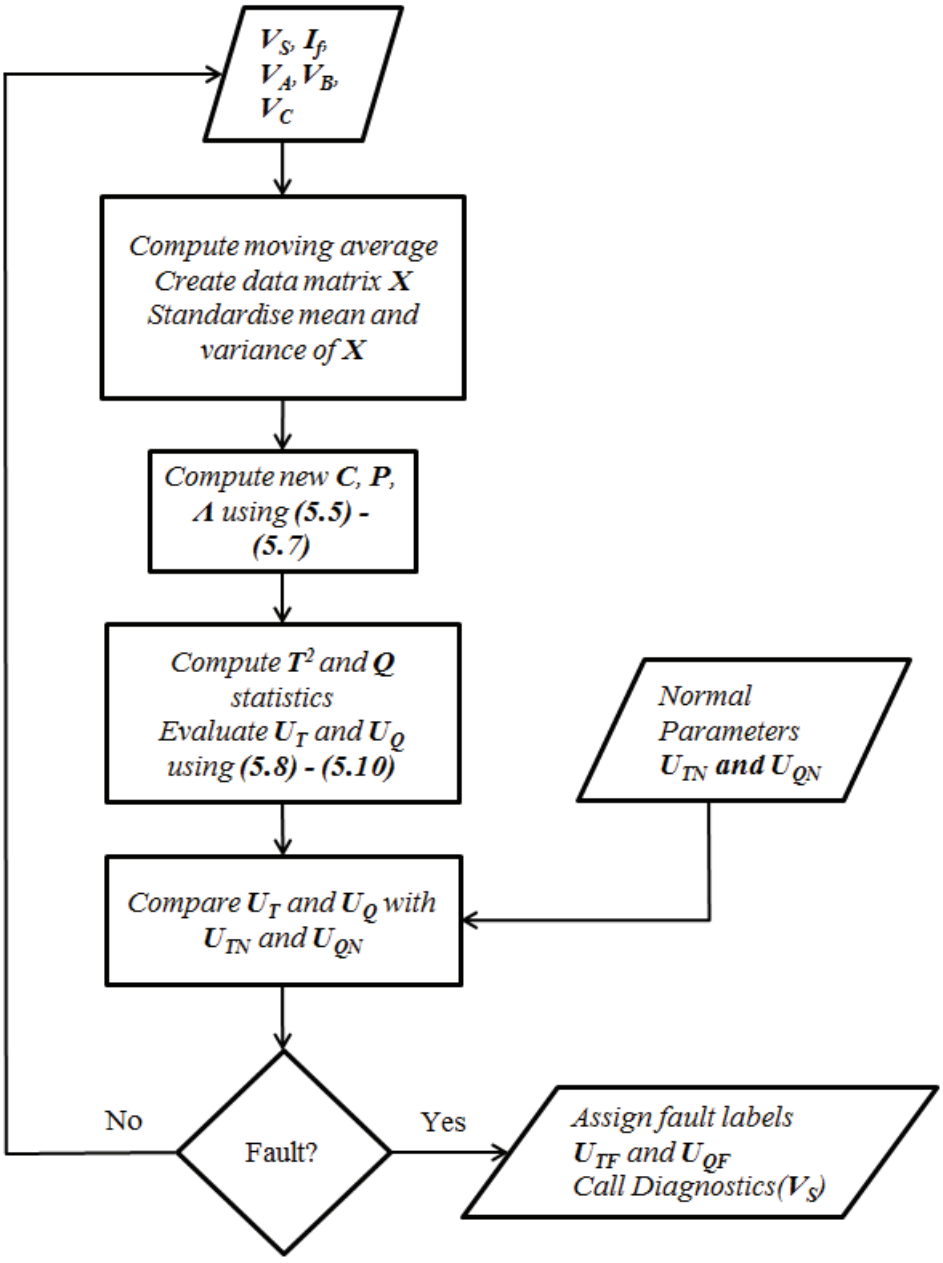


Figure 5.2: Overview of online fault-detection algorithm using PCA

produced by an incipient fault. Figures 5.3 and5.4 (below) show the T^2 and Q statistics generated using data obtained from the FE model. Two data sets are used for this simulation - i.e. normal machine conditions without a load, and a static eccentricity fault of $0.6\,mm$ induced (refer to Appendix A for further details of FE model implementation) and maintained after the first 190 samples.

Simply put, the first set of 190 samples (sample frequency $1\,kHz$)- represents the normal operating conditions and thereafter the samples represent the new fault condition. μ_{TN} and μ_{QN} are the evaluated means for the T^2 and Q statistics under normal conditions, respectively, and μ_{TF} and μ_{QF} are the corresponding means under fault conditions.

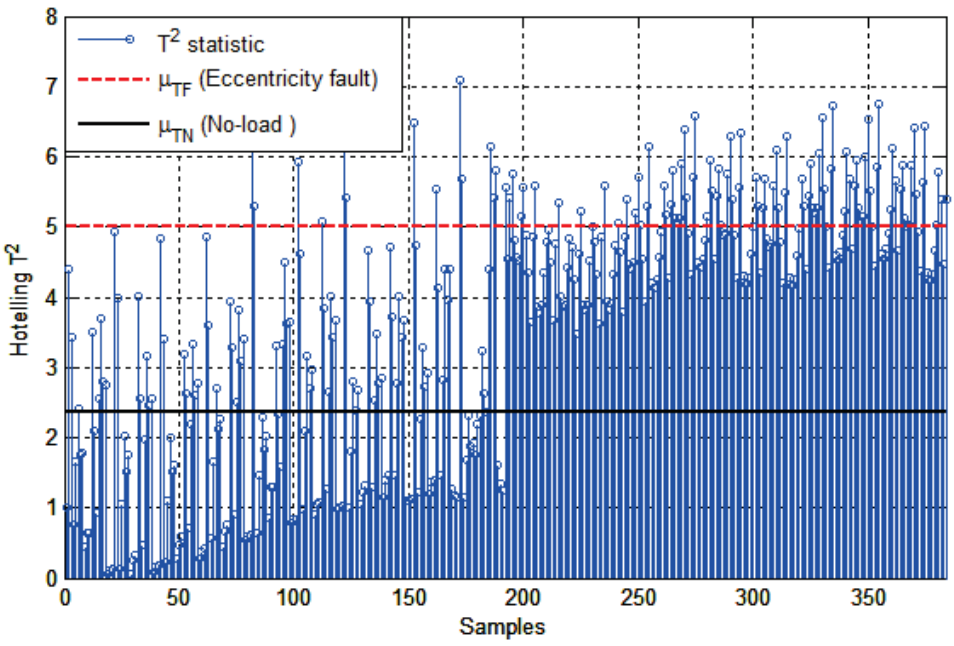


Figure 5.3: Hotelling's T^2 statistic with occurrence of static eccentricity fault, under no-load conditions, evaluated using simulation data

The T^2 and Q statistics presented in figures 5.3 and5.4, clearly indicate significant changes in trend after the occurrence of the eccentricity fault. In order to quantitatively describe this change, equation 5.11 is used to evaluate the actual change in each of the monitored statistics - from normal conditions to fault conditions:

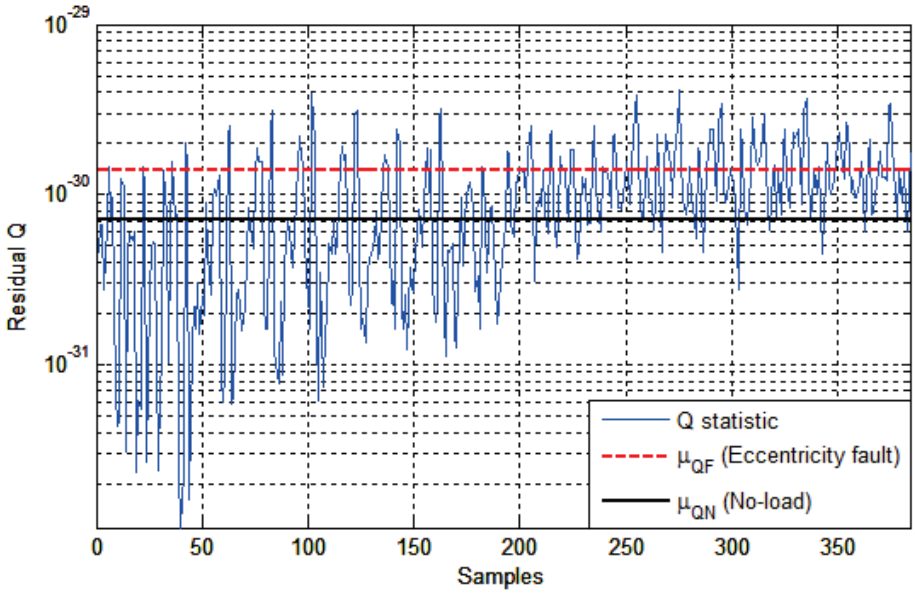


Figure 5.4: Residual Q statistic with occurrence of static eccentricity fault, under no-load conditions, evaluated using simulation data

$$\Delta\mu_x = \frac{\mu_{xF} - \mu_{xN}}{\mu_{xN}} \times 100\% \tag{5.11}$$

Further analysis shows a 111.77 % change in the mean of the T^2 statistic, from normal to a static eccentricity fault condition. The Q statistic exhibits a similar increase of 94.85 %. Similarly, figures 5.5 and 5.6 show results for inception of an inter-turn fault (2 turns) on the rotor winding of the generator. Details of the actual implementation of this fault in the FE model are given in Appendix A.

For the inter-turn short-circuit fault, the mean of T^2 exhibits a 140.62 % change and the mean of Q shows a 146.13 % difference. Results from application of the fault-detection algorithm for additional scenarios are summarised in table 5.1.

Table 5.1 (above) summarises results for each of the previously described fault conditions when the machine is loaded. A similar increase in $\Delta\mu_T$ and $\Delta\mu_Q$ to those obtained under no-load condition is found. The other scenario in the table is the change from normal no-load to normal full-load condition. The purpose of this scenario is to confirm the suitability of the fault-detection algorithm. It is essential that the fault-detection algorithm is capable of distinguishing a change in the operating conditions of the machine from an actual fault. In this case, a

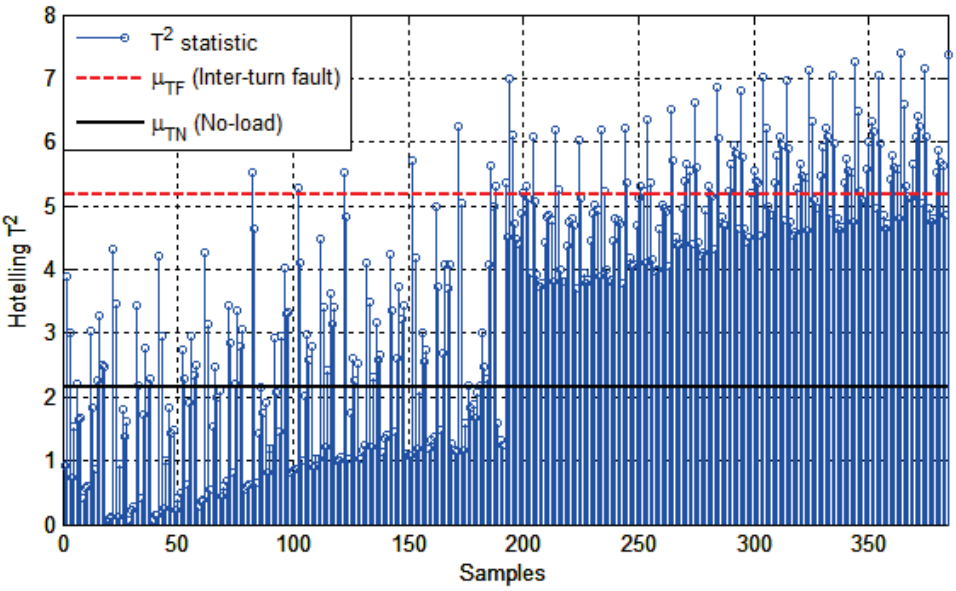


Figure 5.5: Hotelling T^2 statistic with occurrence of rotor winding inter-turn short-circuit fault, under no-load conditions, evaluated using simulation data

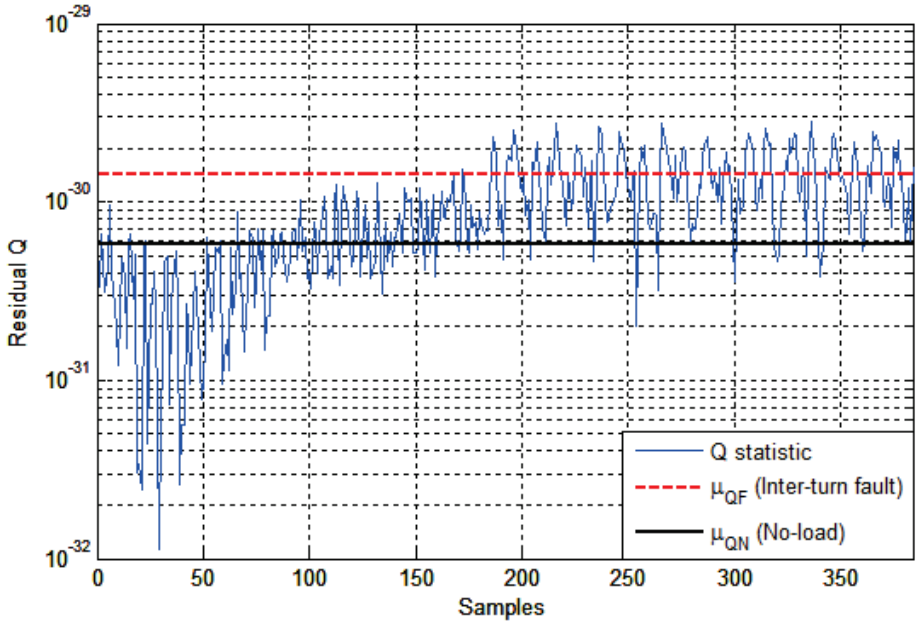


Figure 5.6: Residual Q statistic with occurrence of rotor winding inter-turn short-circuit fault, under no-load conditions, evaluated using simulation data

Table 5.1: $\Delta\mu_T$ and $\Delta\mu_Q$ evaluated using fault-detection algorithm on data obtained from various simulated conditions of synchronous generator

Prior Normal Condition	New Condition	$\Delta\mu_T$ (%)	$\Delta\mu_Q$ (%)
With load (5 Ω)	Eccentricity fault	104.03	73.69
	Inter-turn short (Rotor)	212.46	65.28
No load	With load (5 Ω)	−29.69	3.40

dramatic change in the operating conditions is simulated and each of the statistics are evaluated.

The change in the T^2 statistic - that is $\Delta\mu_T$ - is evaluated to be $-29.69\,\%$. The negative sign of this value is merely an indication of the change in the direction of the average variation of T^2, by virtue of the choice to analyse the means. In other words, there is still a significant variation in T^2 from normal no-load to normal full-load, except that the variation pattern is different from that of a fault. It is expected that $\Delta\mu_Q$ - for this specific scenario - is quite small, since the actual PCA model is not expected to change dramatically when the machine is loaded. These results demonstrate the ability of the fault-detection algorithm to detect the investigated incipient fault, while avoiding false alarms.

5.2.5 Experimental Validation

In order to validate the fault-detection algorithm, experimental measurements are conducted on the synchronous generator. Figures 5.7 and 5.8 (below) show the T^2 and Q statistics generated using the experimental data. These data are processed in the same way as simulation data. Two sets of data are created from experimental measurements - i.e. normal machine conditions without a load, and a static eccetricity fault of $0.5\,mm$ is induced (using procedure described in section 3.4.3) and maintained after the first 190 samples. That is, the first set of 190 samples represents the normal operating conditions and thereafter samples for the new fault condition are used. μ_{TN} and μ_{QN} are the evaluated means of the T^2 and Q statistics under normal conditions, respectively, and μ_{TF} and μ_{QF} are the corresponding means under fault conditions.

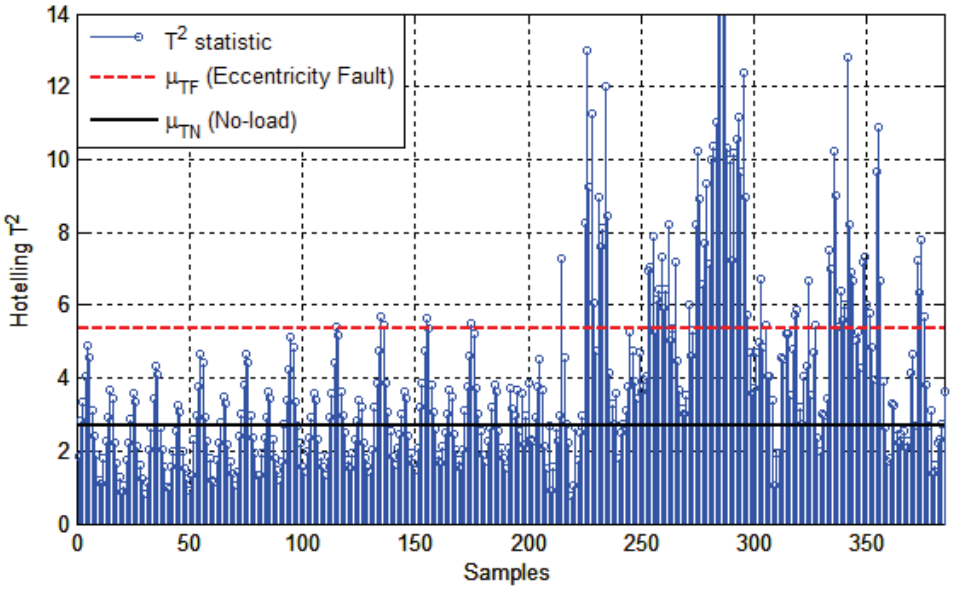


Figure 5.7: Hotelling's T^2 statistic with occurrence of static eccentricity fault, under no-load conditions, evaluated using experimental measurements

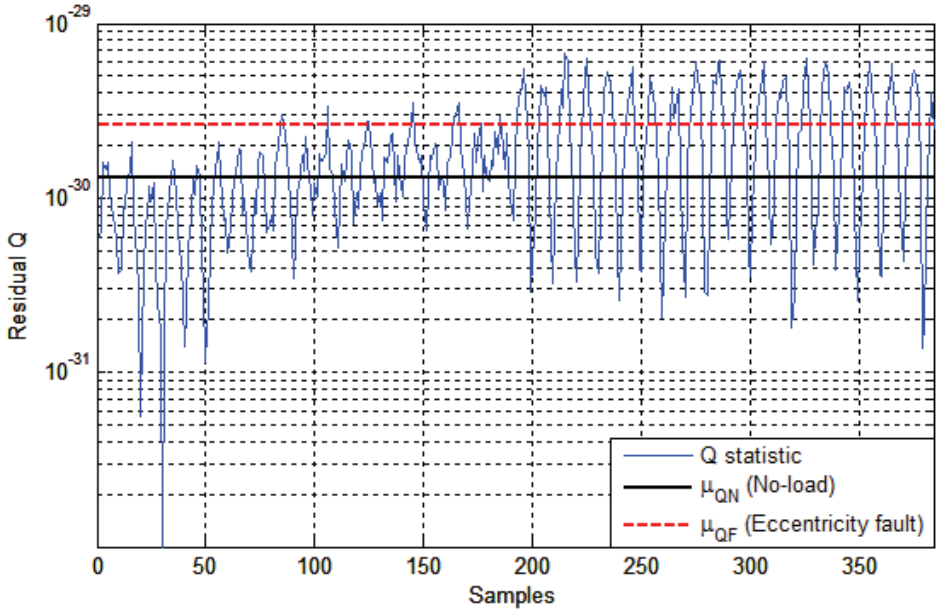


Figure 5.8: Residual Q statistic with occurrence of static eccentricity fault, under no-load conditions, evaluated using experimental measurements

The T^2 and Q statistics, presented in figures 5.7 and 5.8, clearly indicate significant changes in trend on occurrence of the eccentricity fault. Equation 5.11 is again used to quantify the actual change in each of the monitored statistics. The change in the mean of the T^2 statistic from normal conditions to eccentricity fault is found to be 100.72 %. The Q statistic exhibits a similar increase of 99.82 %.

The 2-turn inter-turn short-circuited fault is also experimentally validated. Brass sheet metal is used to create a short-circuit across 2 turns of the rotor-winding overhangs on the generator (see figure 5.9, below). In this way, an inter-turn fault in practice is suitably mimicked under controlled conditions. Like the eccentricity case, figures 5.10 and 5.11 (below) show the fault-detection algorithm results for inception of an inter-turn fault on the rotor winding of the generator.

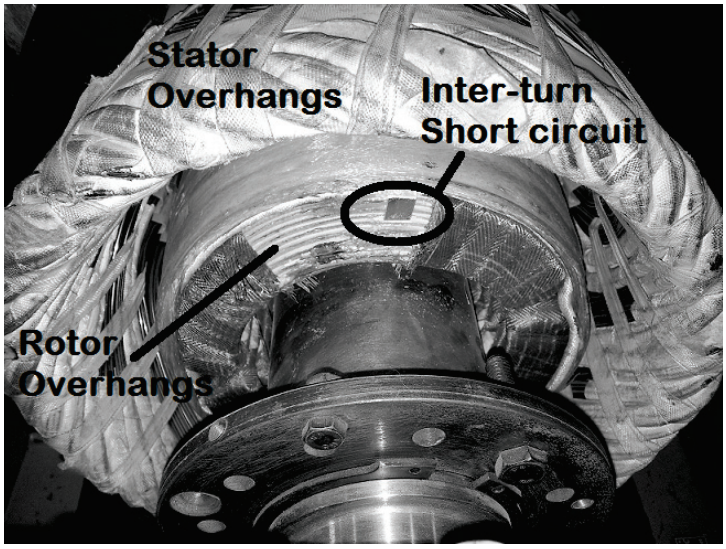


Figure 5.9: Picture of experimental synchronous generator with inter-turn short-circuit fault on rotor overhangs

For the inter-turn short-circuit fault, the mean of T^2 exhibits a 71.87 % change and the mean of Q shows a 140.89 % difference. Results from application of the fault-detection algorithm for additional scenarios are given in table 5.2.

The results given in table 5.2 agree with those results in table 5.1. However, some differences, specifically with $\Delta\mu_T$, are evident. This is due to some minor model

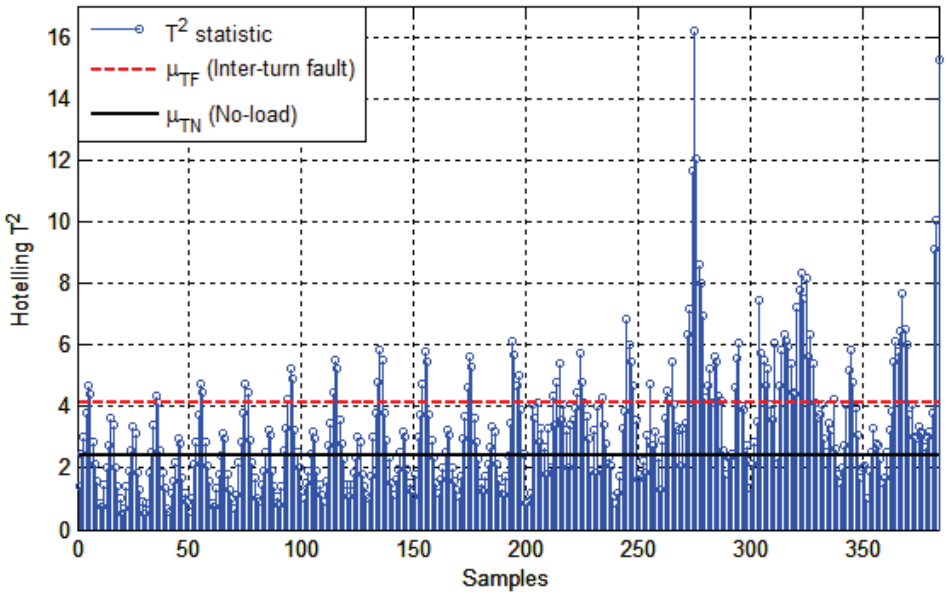


Figure 5.10: Hotelling T^2 statistic with occurrence of rotor winding inter-turn short-circuit fault, under no-load conditions, evaluated using experimental measurements

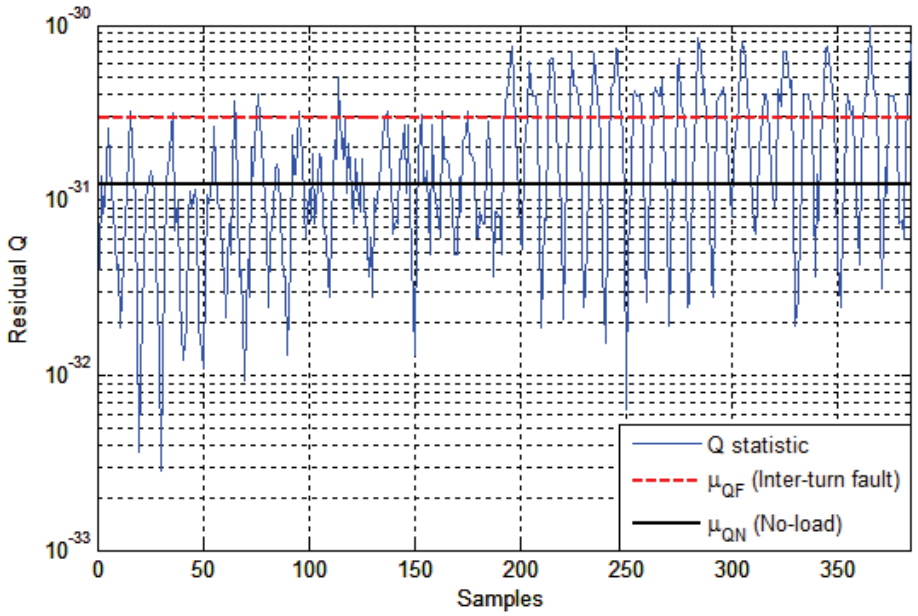


Figure 5.11: Residual Q statistic with occurrence of rotor winding inter-turn short-circuit fault, under no-load conditions, evaluated using experimental measurements

Table 5.2: $\Delta\mu_T$ and $\Delta\mu_Q$ evaluated using fault-detection algorithm on data obtained from experimental measurements for various conditions of synchronous generator

Prior Normal Condition	New Condition	$\Delta\mu_T$ (%)	$\Delta\mu_Q$ (%)
With load (5 Ω)	Eccentricity fault	112.98	70.20
	Inter-turn short (Rotor)	121.74	74.72
No load	With load (5 Ω)	−36.23	−2.68

inaccuracies, as described in 3.4.2, and does not affect the accuracy or suitability of the fault-detection algorithm. Overall change in the mean of the T^2 from a normal no-load to a normal full-load condition follows the pattern - as with the simulation results. $\Delta\mu_Q$ for this case is also found to be approximately zero, as expected. This ensures that the fault-detection algorithm will avoid false alarms when normal operational transients occur on the considered machine. For the implementation of the fault-detection algorithm given in Appendix B, the absolute change in both of the statistical indicators - i.e. $|\Delta\mu_T|$ and $|\Delta\mu_Q|$ - must be greater than 20 % before calling the fault-diagnosis subsystem presented in the following chapter. Figure 5.12 (below) compares the T^2 statistic for the static eccentricity fault with that of the normal loaded condition to illustrate the difference between the T^2 variation pattern for the fault and load condition scenarios. The first 190 samples represent the normal no-load condition, and thereafter the samples are taken from each scenario. It is found that the value of T^2 is greater for the eccentricity fault, on average, than T^2 for the loaded condition.

5.3 Conclusion

In this chapter, a fault-detection subsystem for a synchronous 2-pole generator is presented. The purpose of this subsystem is to assist in optimising shaft-voltage-based condition monitoring in 2-pole synchronous generators. This is achieved by developing an online method to detect incipient faults, avoid false alarms, and prevent unnecessary iterations through the fault-diagnosis algorithm during normal operation.

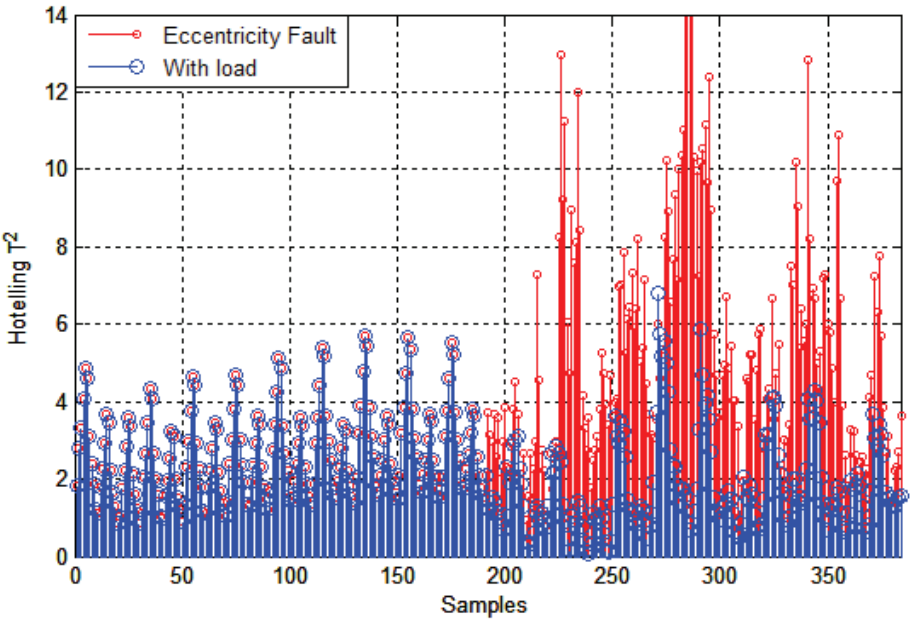


Figure 5.12: Hotelling T^2 statistics for occurrence of an eccentricity fault and for a change in load conditions - i.e. no-load to full-load condition - of the synchronous generator, evaluated using experimental measurements

The statistical PCA method is used for the fault-detection system as it provides reduction in data dimensionality while retaining critical information regarding variation in the raw data. The traditional PCA method is modified to use the three phase voltages, excitation current, and shaft voltage of the machine. Furthermore, the modifications assist in providing resilience to both noise and natural variation in the monitored parameters.

Results from tests conducted on the fault-detection algorithm, using FE model simulation data, show that it can detect two different incipient fault cases: static eccentricity and inter-turn short-circuit faults. Additionally, it was shown that the algorithm is able to distinguish these faults from normal loading on the machine - thus ensuring avoidance of false alarms. The fault-detection algorithm was then validated using experimental measurements on the 2-pole synchronous generator.

Chapter 6

Bayesian Diagnostics

6.1 Introduction

In the previous chapter a fault-detection subsystem was presented. The purpose of the system is to provide accurate incipient fault detection and avoidance of false alarms. As a subcomponent of the condition-monitoring system, it also contributes to the overall efficiency by preventing iterations through the fault-diagnosis algorithm under normal operating conditions. However, this stage of the condition-monitoring system only detects the fault and does not provide details on the type of fault. This chapter presents a subcomponent which is designed to provide qualititative information regarding faults on the machine. In this way, the diagnostic subcomponent serves as the 'intelligence stage' of the condition monitoring system, as described in chapter 2, and carries out an automated assessment of the machine's health.

Diagnostics on an electrical machine may utilise different techniques depending on the maintenance strategy and machine specifications - as described in section 2.3. The specifications of the automated fault-diagnosis subsystem required for optimising the presented shaft-voltage-based condition-monitoring system were described in chapter 4. In order to accurately and efficiently diagnose a fault which has been detected by the fault-detection subsystem presented in chapter 5, a Naive-Bayes Classifier is used - together with Bayesian spectrum estimation. The following section briefly describes the fundamentals of Bayesian statistics. Thereafter, the spectrum-estimation technique used for fault diagnosis is presented. The performance of this technique is compared to other modern signal-processing techniques in the context of the application. Design, implementation and testing of the fault classification technique is then presented in section 6.4. Finally, the overall condition-monitoring system is tested and validated in an experimental setting.

6.2 Fundamentals of Bayesian Statistics

Statistics is the study of uncertainty and is based on two major paradigms - i.e. conventional and Bayesian. The fault-diagnosis subcomponent of the presented condition-monitoring system uses Bayesian methods for spectrum estimation and

fault classification. Bayesian methods provide a complete paradigm for both statistical inference and decision making under uncertainty [127]. Conventional statistics defines probabilities as relative frequencies and does not account for prior information. Bayesian statistics is different in that probability is viewed as a quantitative measure of the strength of knowledge, and incorporates prior information [128].

Recently, Bayesian methods have become increasingly popular with applications that require decision-making under uncertainty - such as [129, 130]. The field of reliability engineering has also adopted Bayesian methods for determining the status of equipment [131]. Fault diagnosis is another good example of an application which involves decision-making under uncertainty, because the condition of a machine is being inferred from measurements.

Bayesian statistics employs Bayes' rule - which is simply derived from the fundamental axioms of probability [132]. The probability of the intersection of event A and event B may be expressed as a conditional probability:

$$p(A \cap B) = p(B)p(A|B). \tag{6.1}$$

The probability of the intersection of these events may be manipulated to give:

$$p(B \cap A) = p(A)p(B|A). \tag{6.2}$$

Since the probability of the intersections given in equations 6.1 and 6.2 are equal, the conditional probabilities may be equated:

$$p(A)P(B|A) = p(B)p(A|B). \tag{6.3}$$

Through substituting event A for a hypothesis H, event B for evidence or data E, and rearranging equation 6.3, Bayes' rule is thus expressed as:

$$p(H|E) = \frac{p(E|H) \times p(H)}{p(E)}. \tag{6.4}$$

Equation 6.4 is used to test the relative truth of the hypothesis, given some information beforehand. The probability $p(H)$ is termed the *prior* which is simply the probability of the hypothesis before the evidence is observed, and $p(H|E)$ is termed the *posterior* which is the probability of the outcome given the evidence. The spectrum estimation and classification methods used for fault diagnosis are based on Bayes' Theorem.

6.3 Bayesian Spectrum Estimation

In chapter 4, the measurement modality was shown to be an important aspect of the condition-monitoring system. However, the signal-processing techniques utilised for fault diagnosis are just as crucial to the overall reliability, accuracy and efficiency of the system. This section presents the Bayesian spectrum estimation technique used in the fault-diagnosis stage of the condition-monitoring system. The technique is used to estimate the frequency characteristics of the shaft-voltage signal for use in the Bayesian fault-classification algorithm.

A study of the performance of different spectral estimation techniques is also presented. The investigation compares the performance of these techniques - specifically for application in incipient fault diagnosis - to the Bayesian technique. The effects of noise on each estimation technique are analysed and the impacts on the diagnosis are assessed.

6.3.1 Fault Diagnosis through Frequency Analysis

Numerous fault detection and diagnosis systems employ methods which require analysis or interpretation of signals in the frequency domain. Examples of these include vibration, flux and current signature-based methods. With discrete measurement of these signals, transformation to the frequency domain is usually carried out using the Fast Fourier Transform (FFT). Most online condition-monitoring systems diagnose problems by registering deviations in the measured signal from a normal steady-state condition. Variations in these signals are usually more distinctly detectable and observable in the frequency domain. Therefore spectral analysis has become a common technique in machine-health diagnostics [2].

In order to monitor minor changes in the health of the system, small changes in the sensing signal should be indubitably quantified. For example, diagnosis of a minor increase of a specific fault level in a machine is only made possible by a definite increase in the *nth* harmonic of the measured signal. However, if the variation of a specific harmonic is not well-defined and highly uncertain, then the diagnosis is rendered unreliable. Figure 6.1 (below) gives an example of the basic elements of a typical fault-diagnosis mechanism which uses spectral analysis.

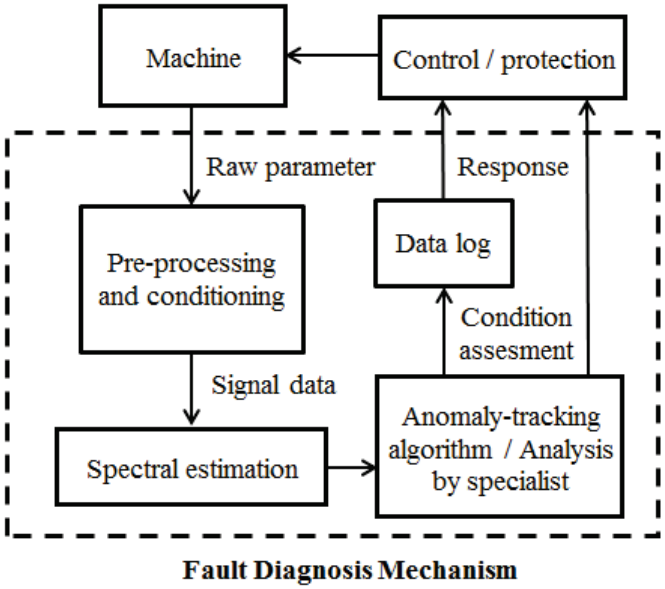


Figure 6.1: Typical example of fault diagnosis on an electrical rotating machine using spectrum estimation

A practical system may be more complex than the example given in figure 6.1, and can contain multiple inputs where various parameters are simultaneously monitored. An automated tracking algorithm or a human specialist may provide spectrum analysis and condition assessment. Additionally, such a system may not always be modular - i.e. integrated implementation of algorithms, as in the case of the presented fault-diagnosis subsystem. The purpose of the example is to indicate the significance of the signal-processing component to the overall efficiency of a system. Many condition-monitoring techniques used in industry use the FFT as a standard processing component of the diagnostic system. The following example of a vibration-based technique is used to illustrate this point.

Vibration Monitoring Example

Traditional practice for diagnosing a defective bearing with a single spall on the track of the outer race, stipulates that a peak shall occur at a frequency (f_p) equal to the number of balls passing over the spall per revolution (n_{BS}), multiplied by the shaft rpm (v_{shaft}) [133]:

$$f_p = n_{BS} \times v_{shaft} \tag{6.5}$$

If the results of a spectrum analysis indicate that a peak occurs at a frequency of $6\,kHz$, then the number of balls passing over a spall defect for a shaft speed of $1000\,rpm$ is calculated, using equation 6.5, as 6.

In the context of the presented system - i.e. shaft-voltage-based system - a relative example would be diagnosis of an eccentricity fault when there is a significant increase in the $300\,Hz$ component of the shaft voltage. Therefore, the objective here is to consider and compare modern signal-processing methods with which to improve the robustness of shaft-voltage-based fault diagnosis. The presented comparison targets performance of spectrum-estimation techniques for cases of incipient fault diagnosis, as part of a predictive maintenance philosophy. Ultimately, this will improve shaft-voltage-based condition monitoring and will potentially assist with improving other traditional frequency-based techniques.

6.3.2 Spectrum Estimation in Condition Monitoring

Recent advancements in signal processing have seen the introduction of many useful techniques, specifically in the area of fault diagnosis in machines. Wavelet transforms is an example of a method that has been gaining in popularity in the field of condition monitoring [134]. There has also been a simultaneous advancement in spectral-analysis tools, with the development of higher resolution techniques and improved computational statistics.

In general, spectrum-estimation techniques may be categorised as either parametric or nonparametric. Nonparametric spectrum estimation is not based on any

assumptions regarding the signal or observed samples, other than wide-sense stationarity. Parametric estimation takes a different approach and views the signal or observed samples as being generated by a random process which can be described by a parametric model. This model enables the spectrum of the process to be expressed in terms of suitably defined parameters.

The presented study focuses on the comparison of a selected few recognised spectrum-estimation techniques - specifically the standard periodogram, Welch and MUltiple SIgnal Classification (MUSIC) techniques - with the presented Bayesian method. The fundamentals of these techniques are firstly described to illustrate the main differences. Thereafter, tests are conducted to determine each technique's suitability for inclusion in the fault-diagnosis algorithm.

6.3.2.1 Standard periodogram

The periodogram is a nonparametric method which was introduced by Schuster in 1898 [135], that acts directly on the observed data/samples to estimate the spectrum. Take a set of observed samples $\left\{x[N]_0^{N-1}\right\}$ - i.e. $x[0]$, $x[1]$, ... , $x[N-1]$. In order to find the periodogram of this data, the autocorrelation sequence must first be estimated and then the Discrete-Time Fourier Transform (DTFT) must be applied. The estimate of the autocorrelation sequence of the data is given by:

$$\hat{R}_x[k] = \frac{1}{N} \sum_{n=0}^{N-1-k} x^*[n]x[n+k], \qquad 0 \leq k \leq N-1 \tag{6.6}$$

where $x^*[n]$ is the complex conjugate and the estimates $\hat{R}_x[k]$, for $-N < k < 0$, are given by:

$$\hat{R}_x[-k] = \hat{R}_x{}^*[k]. \tag{6.7}$$

By taking the DTFT of the total autocorrelation sequence for $-(N-1) \leq k \leq N-1$, the periodogram is estimated as:

$$\hat{P}_{PER}(f) = \sum_{k=-N+1}^{N-1} \hat{R}_x[k] e^{-j2\pi fk} \tag{6.8}$$

where $j = \sqrt{-1}$,
f is the normalised frequency i.e. $0 \leq f < 1$, and
$e^{-j2\pi fk}$ is the complex exponential given by:

$$e^{-j2\pi fk} = cos(2\pi fk) + j\, sin(2\pi fk) \tag{6.9}$$

A more suitable way of defining the periodogram is in terms of the signal samples as given in equation 6.10 - which is given by the squared magnitude of the DTFT of observed samples:

$$\hat{P}_{PER}(f) = \frac{1}{N} \left| \sum_{n=0}^{N-1} x[n] e^{-j2\pi fn} \right|^2 \tag{6.10}$$

The periodogram of a set of observed samples is determined in practice using the FFT algorithm (see Appendix B).

6.3.2.2 Welch method

Welch estimation is essentially a modified periodogram with the observed data split into segments [136]. The averages of the periodograms for the segments are then found. A unique characteristic of this method is that the segments overlap and are windowed. In order to provide a basic expression for the Welch periodogram, a length of segment (L_{Seg}) and offset of successive sequences (D) must be selected. For a total number of sequences (K), the total number of observed samples may be expressed as:

$$N = L_{Seg} + D(K + 1) \tag{6.11}$$

The sequences may then be expressed as:

$$x_i[n] = x[n + (i - 1)D] \qquad where\ n\ \in\ \{0, \ldots, L_{Seg} - 1\} \tag{6.12}$$

Using a weighted window ($w[n]$]), the i^{th} periodogram may be expressed as equation 6.13, with the Welch estimate given by equation 6.14:

$$\hat{P}_i(f) = \frac{1}{L_{Seg}} \left| \sum_{n=0}^{L_{Seg}-1} w[n]x[n]e^{-j2\pi fn} \right|^2 \tag{6.13}$$

$$\hat{P}_{Welch}(f) = \frac{1}{K} \sum_{i=0}^{K} \hat{P}_i(f) \tag{6.14}$$

6.3.2.3 MUSIC method

Multiple Signal Classification (MUSIC) is one of the super-resolution methods which are categorised into the modern parametric spectral-analysis techniques or modern subspace methods. Super-resolution techniques consider a signal model or observed data, in the form of a mixture of a specified number of noisy complex exponentials. The aim of the MUSIC algorithm is to separate the useful signal subspace from the noise subspace. In order carry out this task, this technique firstly defines m complex sinusoids in white noise, as given in equation 6.15:

$$x[n] = \sum_{i=1}^{m} A_i e^{j2\pi f_i n} + w[n] \tag{6.15}$$

where f_i is the frequency of the i^{th} complex sinusoid,
A_i is the complex amplitude of thei^{th} sinusoid, and
w is zero mean white noise with variance σ_w^2.

Using this definition, the autocorrelation matrix (R_x) of $x[n]$ is then expressed as an $M \times M$ matrix with $M > m + 1$, as follows:

$$R_x = \sum_{i=1}^{m} |A_i|^2 \mathbf{e}_i \mathbf{e}_i^H + \sigma_w^2 \mathbf{I} \tag{6.16}$$

where $\mathbf{I}$ is the identity matrix and

$$\mathbf{e}_i = \left[1 \; e^{j2\pi f_i} \; e^{j4\pi f_i} \; ... \; e^{j2\pi f_i(N-1)}\right]^T \tag{6.17}$$

The eigenvalues (λ_i) of R_x are then arranged in descending order - i.e. $\lambda_1 \geq \lambda_2$, ... ,$\geq \lambda_M$ - with corresponding eigenvectors (v_i), for two groups to be made:

1. m signal eigenvectors corresponding to m largest eigenvalues.
2. $M - m$ noise eigenvectors with eigenvalues equal to σ_w.

The variance of the noise is then estimated using equation 6.18, and a pseudospectrum is determined in terms of the signal vector and the noise eigenvector using equation 6.19 [137]:

$$\sigma^2 = \frac{1}{M-m} \sum_{i=m+1}^{M} \lambda_i \tag{6.18}$$

$$\hat{P}_{MUSIC}(f) = \frac{1}{\left| \sum_{i=m+1}^{M} \mathbf{e}^H v_i \right|^2} \tag{6.19}$$

6.3.2.4 Bayesian method

The Bayesian spectrum-density estimation is defined as the expected value of the signal spectrum over the joint posterior probability distribution of all the parameters - i.e. signal and noise parameters [138, 139, 140]. Essentially, this method provides the expectation of the signal spectrum only in the form of a posterior distribution. The expectation is an estimate of the total energy carried by the signal of a specified frequency range. The technique emerges from the basic approximation of the probability for the frequency of a periodic sinusoidal signal given in equation 6.20. The given data (D) may be the observed samples, with prior (I). The Schuster periodogram is divided by the noise variance and emerges in a natural way in the derivation of the posterior probability as shown in [141]:

$$p(f|D,\, I) \propto exp\left\{ \hat{P}_{PER}(f)/\sigma^2 \right\} \tag{6.20}$$

The Bayesian spectrum-estimation technique utilised for this investigation derives the posterior distribution of the spectrum of one or more time series. This non-parametric Bayesian method uses the Whittle likelihood to update the prior in

order to obtain a pseudoposterior. Significant qualities of this method are the treatment of the noise spectrum as an unknown - which is commonly taken as a known - and the freedom to specify the degree of prior information. This feature has an advantage over a frequentist framework, which would require an ad-hoc regularisation to achieve something comparable. Theoretical details of this work are presented in [142], and are summarised here. Consider the time series x_i - consisting of N real-valued observations sampled with period $\triangle t$ - which can be represented in terms of sinusoids of the Fourier frequencies as follows:

$$x_i = \frac{1}{\sqrt{N\triangle t}} \sum_{j=0}^{N/2} \{a_j cos(2\pi f_j t_i) + b_j sin(2\pi f_j t_i)\} \tag{6.21}$$

where a_j and b_j correspond to the Fourier frequencies $f_j = j/N\triangle t$. In this definition, b_0 is always zero, and $b_{N/2}$ is zero when N is even. For each f_j, let κ_j be the number of non-zero Fourier coefficients which implies:

$$\kappa_j = \begin{cases} 0 & if\ j = 0,\ N\, is\, even\, and\, j = N/2 \\ 1 & otherwise \end{cases} \tag{6.22}$$

Therefore, functions of the Fourier coefficients are defined as:

$$p_1(f_j) = \frac{a_j^2 + b_j^2}{\kappa_j} \quad and \tag{6.23}$$

$$p_2(f_j) = \frac{a_j^2 + b_j^2}{\kappa_j} \tag{6.24}$$

which are discrete analogues of the one-sided and two-sided spectral power, respectively. Consider the observations x_i correspond to the random variable X_i, then the time series has zero mean if the expectation (E) of the Fourier coefficients is zero, as follows:

$$E[X_i] = 0\ \forall\, i, \quad if \quad E[A_j] = E[B_j] = 0\ \forall\, i \tag{6.25}$$

A corresponding normal time-series model can be set by assuming all the frequency domain elements to be stochastically independent, have zero mean and:

$$Var(A_j) = \sigma_j^2 \quad where\ j \in \{0, 1 \dots N/2\} \quad and \tag{6.26}$$

$$Var(B_j) = (\kappa_j - 1)\sigma_j^2 \quad where\ j \in \{0, 1 \dots N/2\} \tag{6.27}$$

Assuming normality for A_j and B_j allows inference of the spectrum of the observed data - with an unknown σ_j^2 - through the likelihood function:

$$\begin{aligned} p(x_1, \dots x_N | \sigma_0^2, \dots \sigma_{N/2}^2) \quad = \quad & \prod_{j=0}^{N/2} \left\{ \frac{1}{\sqrt{2\pi}\sigma_j} exp\left(-\frac{a_j^2}{2\sigma_j^2}\right) \right. \\ & \left. \times \left(\frac{1}{\sqrt{2\pi}\sigma_j}\right)^{\kappa_j - 1} exp\left(-\frac{b_j^2}{2\sigma_j^2}\right) \right\} \end{aligned} \tag{6.28}$$

The presented method uses a scaled inverse χ^2 distribution for the conjugate prior distribution of σ_j^2, with the scale parameters s_j^2 and degrees-of-freedom ς_j as given in equation 6.29. These parameters denote the precision and order of magnitude of the prior distribution. The implications of these parameters and of the prior distribution is discussed in detail in [142]:

$$\sigma_j^2 \backsim Inv\,\chi^2(\varsigma_j, s_j^2) \tag{6.29}$$

The use of the conjugate prior distribution enables the unknown noise spectrum to be integrated out of the presented likelihood expression, to yield the marginal likelihood, as follows:

$$\begin{aligned} & p(x_1, \dots x_N | \varsigma_0, \dots \varsigma_{N/2},\ s_0^2, \dots s_{N/2}^2) \\ = & \prod_{j=0}^{N/2} \int_0^\infty p(a_j, b_j | \sigma_j^2) p(\sigma_j^2 | \varsigma_j, s_j^2)\, d\sigma_j^2 \end{aligned} \tag{6.30}$$

and an uninformative prior with zero degrees-of-freedom and density $p(\sigma_j^2) \propto \frac{1}{\sigma_j^2}$ (details of the uninformative prior is shown in [138] and discussed in great detail in [143]), yields:

$$p(x_1, \ldots x_N) \propto \prod_{j=0}^{N/2} p\left(\kappa_j^2 \frac{\triangle t}{N} |\tilde{x_j}|^2\right)^{-\frac{\kappa_j}{2}} \tag{6.31}$$

where $\tilde{x_j}$ is the j^{th} element of the Fourier transformed data vector. For this study, the implementation of this Bayesian spectrum-estimation method - given by [144] - is used. The following algorithm (see listing 6.1, below) describes the function implementation (see code listing in section B.2 of the Appendix) for the 1D data or time series.

Listing 6.1: Algorithm for Bspec function used for Bayesian spectrum estimation

```
1  Input x {time series data}
2  Initial checks for data validity
3  Initialisation of priorscale, priordf,
4  N = length(x)
5  Neven = true if remainder(N/2) ==0 else false
6  FTlength = quotient(N/2)+1
7  Initialise deltaT
8  Kappa = 0, 1...1, q  {length is FTlength-1, q=0 if
       Neven true else q=1 otherwise}
9  y = unnormalised fft(x)
10 a = (1+kappa)*(sqrt(detaT/N))*Re(y[FTlength])
11 b = -(1+kappa)*(sqrt(detaT/N))*Im(y[FTlength])
12 priordfvec = priordf, ..., priordf  {length is
       FTlength}
13 priorscalevec = priorscale, ..., priorscale  {length
       is FTlength}
14 DataSsq = (a^2) + (b^2)
15 Datadf = 1, 2....2, r  {length is FTlength-1, r=1 if
```

```
        Neven true else r=2 otherwise}
16  Result = (priordfvec+priorscalevec+DataSsq)/(
        priordfvec+Datadf)
```

6.3.3 Performance of Techniques in Incipient Diagnosis

6.3.3.1 Fault resolution

A desirable characteristic of the signal processing technique, utilised in incipient fault diagnosis, is the ability to distinguish minor variations in the frequency component attributed to a specific fault. Hence, it is advantageous to use a technique that is sensitive to an early fault. This property is termed the 'fault resolution' for the purpose of this investigation. A greater fault resolution implies an enhanced fault-distinguishing capability. For example, deterioration in the condition of a synchronous generator resulting from the a shift in rotor eccenctricity from $0.3\,mm$ to $0.6\,mm$, can be diagnosed when a considerable change occurs in the $300\,Hz$ frequency component. A quantifiably larger increase in the magnitude of this harmonic allows for a more certain diagnosis. This characteristic is examined for each of the techniques when applied to the shaft voltage-signal for two incremental fault conditions on the rotor:

1. ΔF_A - $0.3\,mm$ to $0.6\,mm$ static eccentricity.
2. ΔF_B - $0.6\,mm$ to $0.9\,mm$ static eccentricity.

These conditions represent the occurrence of an incipient fault event in practice and mimics a default air-gap eccentricity on a real machine due to manufacturing and/or commissioning tolerances. The percentage change in the normalised magnitude of the $300\,Hz$ component is measured after applying each of the techniques for both fault increments. Results of the comparison are given in figure 6.2 and show that the Bayesian method provides the best fault resolution. Additionally, the Welch method is known to have a better frequency resolution than the standard periodogram; these results indicate that it is not the case with the fault resolution.

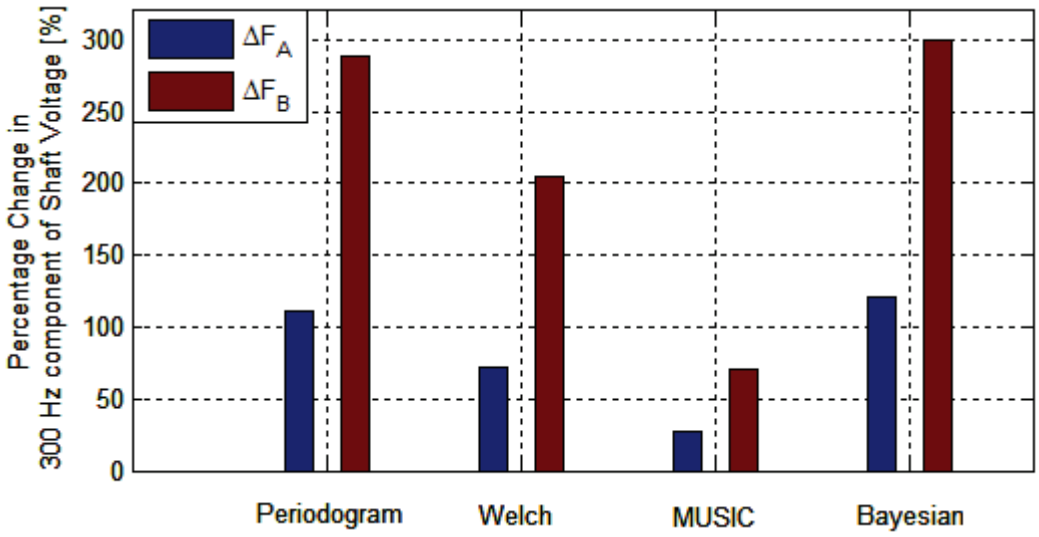


Figure 6.2: Comparison of percentage change in shaft-voltage harmonic, for two types of incipient fault increments, obtained using different spectrum-estimation techniques

6.3.3.2 Frequency estimation and spectral leakage

Another performance indicator for spectral techniques is the accuracy with which a harmonic of a signal is defined. Spectral leakage occurs for a finite-length signal where the estimation exhibits energy 'leaked' into frequencies in between harmonics. In the context of fault diagnostics, it is essential that the harmonic or expected 'fault frequency' is well-defined and easily detected amongst other frequencies. Although the harmonic is usually always detectable - even for short data records - the certainty of the diagnosis diminishes with an increase in spectral leakage. Figure 6.3 (below) gives a comparison of the Welch and Bayesian spectrum estimation of the shaft-voltage signal under a rotor fault of $0.3\,mm$ eccentricity.

The posterior distribution and spectral-density estimates provided by the Bayesian method exhibit well-defined peaks at the expected harmonics. Additionally, the lobes of the signal's natural harmonics are narrower and allow for a more accurate account of the interesting frequency, e.g. $300\,Hz$, than the Welch method.

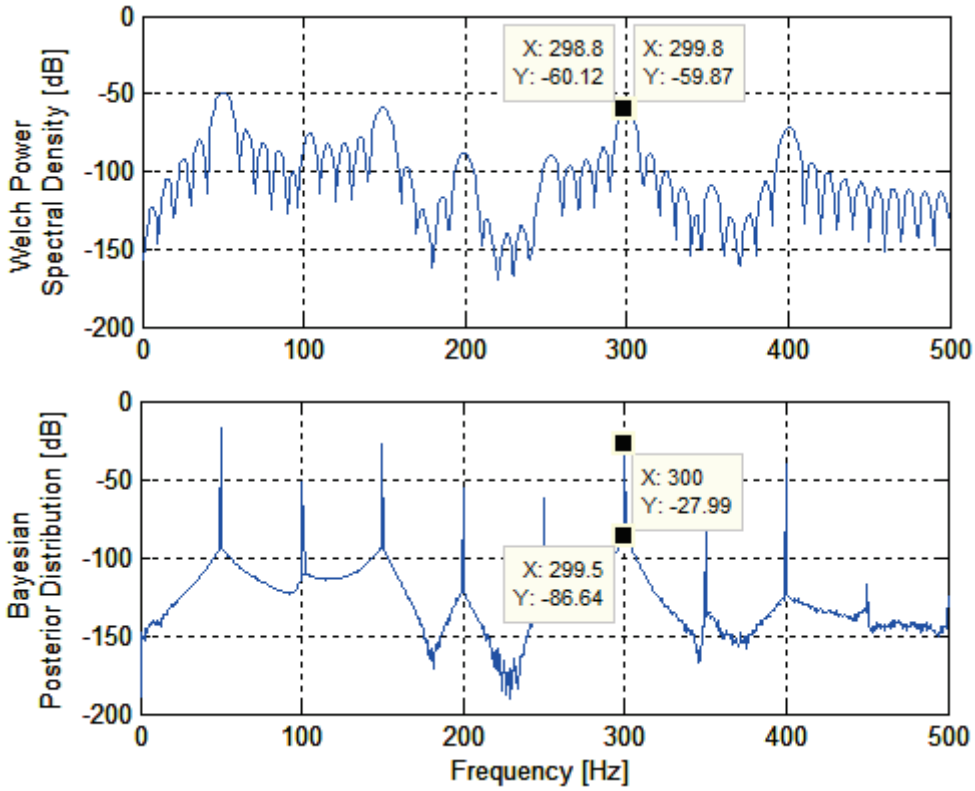


Figure 6.3: Comparison of Welch and Bayesian spectrum estimations of a shaft-voltage signal for a $0.3\,mm$ static rotor eccentricity fault

6.3.3.3 Noise performance

Another significant performance measure of spectrum estimation techniques is the robustness of the signal-processing method against noise. This characteristic may be thought of as the accuracy of the algorithm in extracting the frequency components of the signal in the presence of noise. In practice, noise levels could change for a number of reasons, such as addition of surrounding infrastructure/equipment amongst other changes in the immediate environment surrounding the machine. The relative error in identification of the eccentricity affected harmonic ($300\,Hz$) for each technique, is determined for varying a signal-to-noise ratio (SNR). These results are shown in figure 6.4 (below). Figure 6.4 shows that the lowest identification error for higher noise levels, is achieved when using the Bayesian method. A more generalised performance measure of the estimate is the variance at different noise levels [137], and is given in figure 6.5 (below).

The plot given in figure 6.5 indicates that the MUSIC method exhibits almost no change in the variance of the estimate, while the periodogram exhibits the greatest variation. Moreover, the variance of the Bayesian estimate is less affected in comparison to the Welch and periodogram methods. It is also expected that the Welch method will produce similar results to the periodogram in this case [136].

6.3.4 Evaluation

The Bayesian method exhibits the best performance against noise and also yields good fault-resolution capabilities. The MUSIC algorithm is known to provide good frequency resolution, but is found to be costly in terms of accuracy. Welch spectrum estimation is found to perform poorly in all areas, for the presented application. The overall result indicates that Bayesian spectrum estimation is the most suitable of the investigated techniques, for use in the presented fault-diagnosis subsystem. Hence, the Bayesian spectrum-estimation technique is used to determine the harmonics of the shaft-voltage signal for use in the fault-classification algorithm.

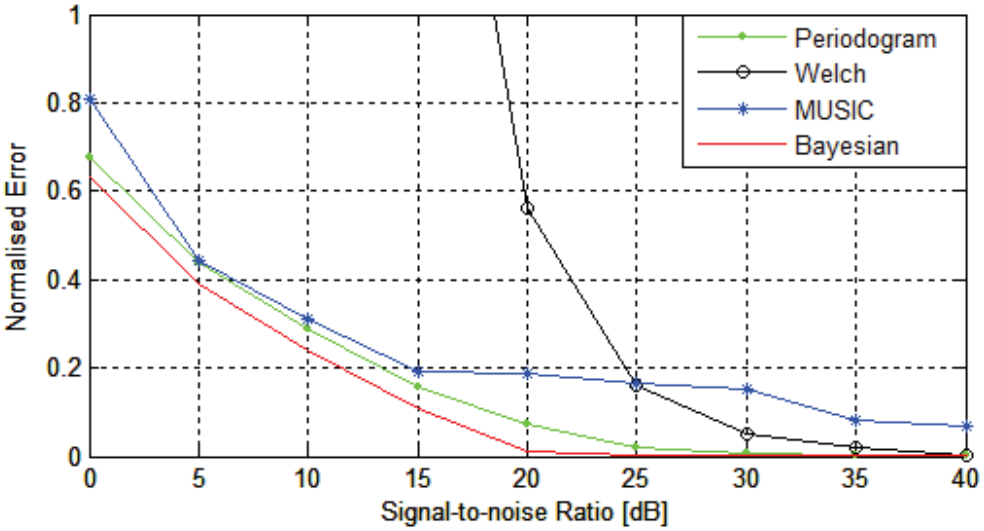


Figure 6.4: Measure of relative error for spectral estimation technique, in identification of eccentricity affected harmonic, simulated under varying noise levels

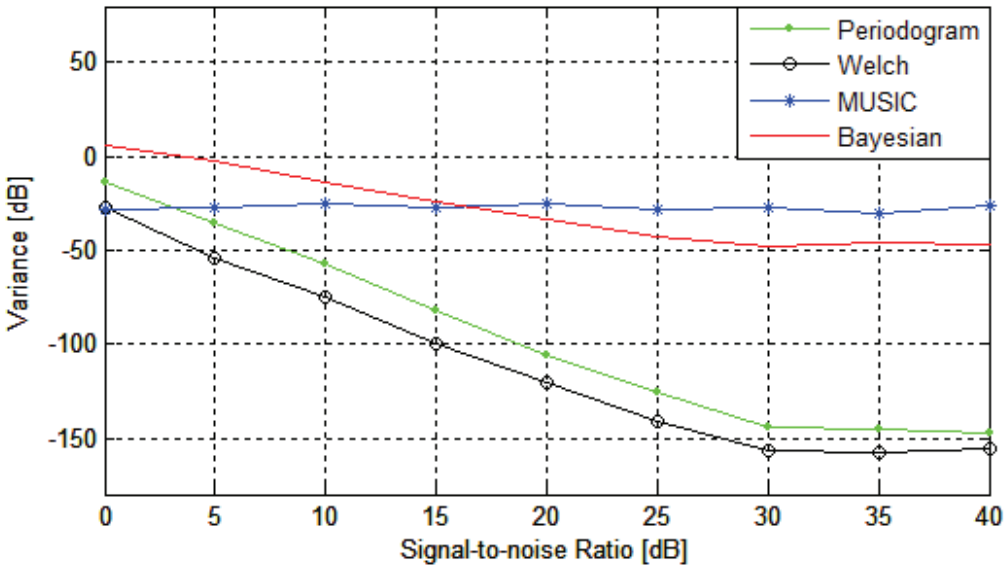


Figure 6.5: Measure of variance for spectral-estimation techniques, in identifying an eccentricity fault, simulated under varying noise levels

6.4 Bayesian Fault Classification

In chapter 4, the requirements for addressing challenges with fault diagnosis were discussed. The main inference from analysing these requirements and associated constraints, is that a machine-learning approach is best suited to solving the fault-diagnosis problem. This section describes the classification component of the fault-diagnosis system. Simply put, once the shaft-voltage frequency spectrum has been estimated, using the previously described Bayesian technique, an algorithm extracts the harmonics. These harmonics are then used by the classifier to predict the type of fault on the machine using probabilistic classification.

6.4.1 Probabilistic Classification using Bayes Theorem

Pattern classification is the act of assigning a class label to an object, physical process or an event, based on some prior information [145]. For the presented application, the shaft-voltage behaviour exhibits a specific pattern corresponding to each fault. The posterior distribution of the shaft voltage at each of the harmonics - given by the Bayesian spectrum estimate - are the characteristics which

enable identification of this pattern. Figure 6.6 (below) illustrates the relationship between these characteristics for different instances measured in an experimental setting. The figure illustrates the Bayesian spectrum estimates, at three different frequencies - i.e. $50\,Hz$, $100\,Hz$ and $300\,Hz$ - of shaft voltages measured under rotor winding short-circuit fault ($2\,turns$), eccentricity fault ($0.5\,mm$), and healthy conditions. A total of 19 separate shaft-voltage measurements were taken with the experimental synchronous generator operating at $3000\,rpm$, with $40\,A$ DC excitation and a $5\,\Omega$ load.

Figure 6.6, shows that the magnitudes of the shaft-voltage measurements, at the presented frequencies, have a tendency to cluster in specific regions corresponding to the condition under which the measurement is taken. Machine-pattern classification is therefore required to accurately and automatically identify a specific condition associated with the shaft-voltage measurement. The presented solution uses a probabilistic form of pattern classification to achieve this.

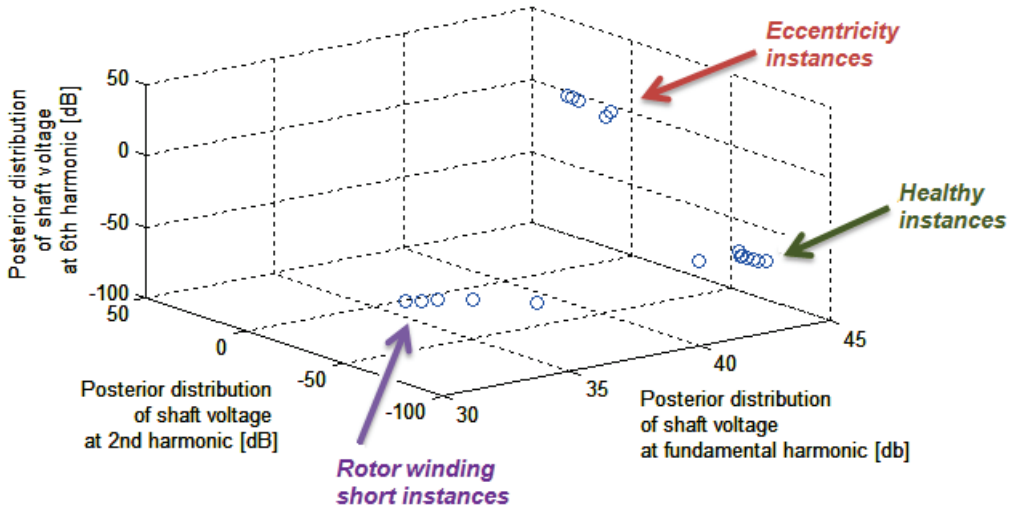


Figure 6.6: 3-D Scatter plot, illustrating the relationship of the shaft-voltage harmonics under different conditions, with each point representing a shaft-voltage measurement on the experimental synchronous generator

Probabilistic classification differs from conventional pattern classification as it predicts a probability distribution over the set of possible classes. This type of classifier is deemed more suitable for the presented application, as it not only assigns

a class label, but also provides a quantifiable certainty with its prediction. For example, if a measurement is predicted to fall into an eccentricity fault category, it is important to quantify how close the case is to being a typical instance of an eccentricity fault. This is achieved by using an algorithm that uses features or attributes as inputs. The presented algorithm uses the Naive-Bayes classifier which is a probabilistic classifier based on the application of Bayes' theorem with independence assumptions. Essentially, the classifier uses multiple evidence to validate a hypothesis by simply extending equation 6.4 to:

$$p(H|E_1, E_2 \ldots, E_N) = \left\{ \frac{p(E_1, E_2 \ldots, E_N|H) \times p(H)}{p(E_1, E_2 \ldots, E_N)} \right\} \tag{6.32}$$

In a practical sense, this means that multiple non-redundant features or attributes are used by classifier. The 3D space illustrated in figure 6.6 is created using only three features (posterior distributions of shaft voltage at 3 different frequencies), while the implemented classifier uses 10 different features. This improves the accuracy of the classifier and extends the range of the behaviour maps. Additionally, the Naive-Bayes classifier provides good performance using moderately sized training sets.

6.4.2 Fault-Classification System

6.4.2.1 Algorithm overview

An algorithm was developed to meet the fault-diagnosis requirements described in chapter 4, as given by the flowchart in figure 6.7. Once the PCA algorithm detects a fault, the diagnostics function is called. A subroutine is first used to estimate the frequency spectrum posterior distribution using the Bayesian method. The magnitudes of the spectrum's posterior distribution are then extracted and used as features in a class instance (see section B.2 of appendix B for code listing). A pre-trained classifier then processes this instance and outputs a label (healthy or fault type) with an associated probability. Details of the mathematical model, implementation and testing of the classifier, is presented in the following sections.

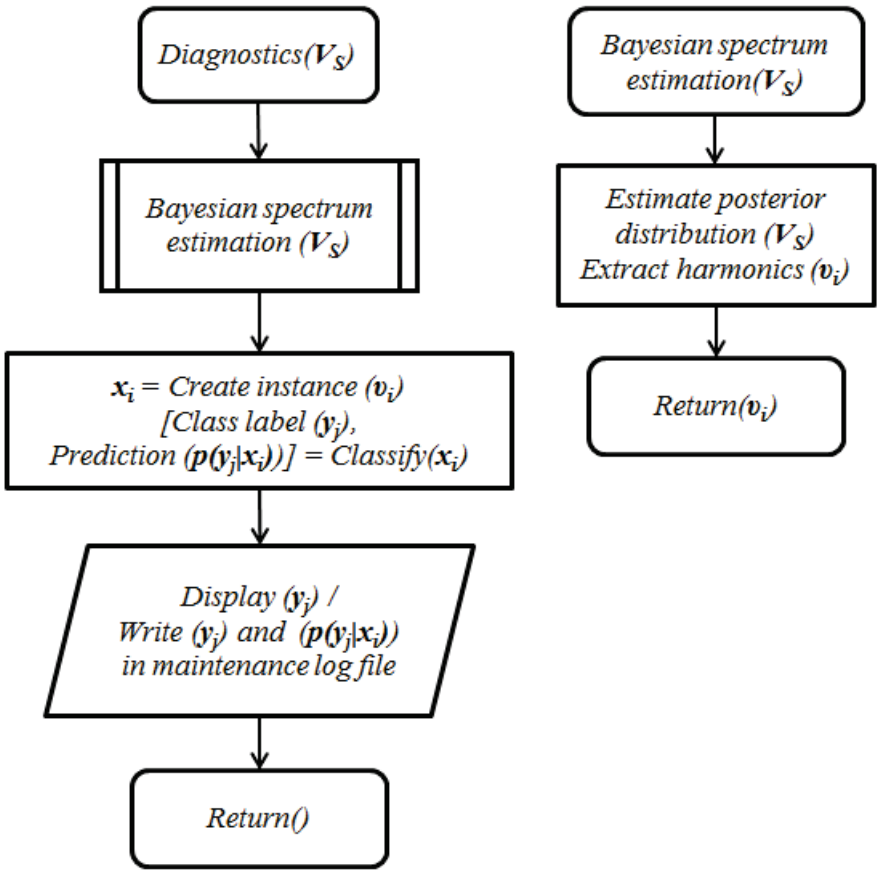


Figure 6.7: Flowchart of fault-diagnosis algorithm for online classification of faults on a synchronous generator using shaft-voltage signals

6.4.2.2 Mathematical model of Naive-Bayes classifier

For practical implementation of the Bayes theorem, the Naive-Bayes method focuses on determining the numerator of equation 6.32. The denominator of this equation, for the presented case, is constant as the values of the features do not depend on the prior class probability $p(H)$. Hence, the posterior can be expressed using the numerator only and simplified using the chain rule, as follows:

$$\begin{aligned} p(H|E_1, E_2 \ldots, E_N) &\propto p(H)p(E_1, E_2 \ldots, E_N|H) \\ &\propto p(H)p(E_1|H)p(E_2|H, E_1), \\ &\quad \ldots, p(E_N|H, E_1, E_2 \ldots, E_{N-1}) \end{aligned} \tag{6.33}$$

The Naive-Bayes method assumes that the features are conditionally independent, which implies that knowledge of one feature does not give any information regarding a separate feature. This enables further simplification of equation 6.33, as follows:

$$\begin{aligned} p(H|E_1, E_2 \ldots, E_N) &\propto p(H)p(E_1|H) \ldots p(E_N|H) \\ &\propto p(H) \prod_{i=1}^{N} p(E_i|H) \end{aligned} \tag{6.34}$$

The main aim of the classifier is to assign a particular label to an instance. This is achieved by determining the maximum probability of the an instance falling in a specific class according to it's features or attributes. This means that the most probable hypothesis (h), given the training data (D), is targeted according to the decision rule or *maximum a posteriori* (MAP) given by:

$$\begin{aligned} h_{MAP} &= \arg\max_{h \in H} p(h|D) \\ &= \arg\max_{h \in H} \frac{p(D|h)p(h)}{p(D)} \\ &= \arg\max_{h \in H} p(D|h)p(h) \end{aligned} \tag{6.35}$$

The above expression is simplified even further by assuming $p(h_i) = p(h_y)$, which implies that the prior-class probabilities are equal. Practically, this means that the probability of each class label corresponding to a specific machine condition or fault is assumed to an equally likely event. This is termed the maximum likelihood (ML) and is expressed as follows:

$$h_{ML} = \arg\max_{h_i \in H} p(D|h_i) \tag{6.36}$$

Now consider the target function $G : X \rightarrow Y$ described in chapter 4, where Y is the class label (condition/fault) and X is the input data (shaft voltage). Let x be

an instance of the shaft voltage with features $\upsilon_1, \upsilon_2 \ldots, \upsilon_n$, corresponding to the harmonics. The most probable values of $G(x)$ are given by:

$$\begin{aligned} y_{MAP} &= \arg\max_{y_j \in Y} p(y_j|\upsilon_1, \upsilon_2 \ldots, \upsilon_n) \\ &= \arg\max_{y_j \in Y} \frac{p(\upsilon_1, \upsilon_2 \ldots, \upsilon_n|y_j)p(y_j)}{p(\upsilon_1, \upsilon_2 \ldots, \upsilon_n)} \\ &= \arg\max_{y_j \in Y} p(y_j) \prod_{i=1}^{n} p(\upsilon_i|y_j) \end{aligned} \tag{6.37}$$

A standard assumption of the presented method is that the features - for a given class - have a normal or Gaussian probability distribution. The probability-density function is defined according to the sample mean:

$$\Theta = \frac{1}{n} \sum_{i}^{n} x_i \tag{6.38}$$

and the standard deviation:

$$\Lambda = \frac{1}{n-1}(x_i - \Theta)^2 \tag{6.39}$$

Since the harmonics are numerical features and continuous values, the probability density of a value (ν) of a specific feature, for a given class, is computed as follows [146]:

$$p(\upsilon = \nu|y) = \frac{1}{\sqrt{2\pi\Lambda_y^2}} e^{-\frac{(\nu-\Theta y)^2}{2\Lambda_y^2}} \tag{6.40}$$

The Naive-Bayes model, at this point, has a computational limitation. This limitation - known as the 'zero frequency' problem - is realised when there is an occurrence of an instance that falls within any class or available training data. In this case, the total posterior probability would result in zero and a computational error. This problem is solved using the Laplace smoothing, which assigns a reasonable non-zero probability through a simple pseudocount [147]. The prevents the

probability estimate from becoming zero and requires the addition of a relatively small value to the argument in equation 6.37, as follows:

$$\hat{p}(\upsilon_i|y_j) = \frac{N_{\upsilon_i y_j} + \kappa}{N_{\nu_i y} + n_i \kappa} \tag{6.41}$$

where $N_{\upsilon_i y_j}$ is the number of occurrences of the feature in a specific class,
$N_{\upsilon_i y}$ is the total number of occurrences of the feature in all classes,
n_i is the number of distinct values which υ_i can take on, and
κ is the smoothing constant.

6.4.2.3 Implementation and testing of classification algorithm

The algorithm given in figure 6.7 is implemented in Matlab - which directly interfaces with the dSpace measurement system and experimental generator. Additional script is used to call specialised routines such as the Bayesian spectrum estimation and Naive-Bayes classifier core, which are coded in R and Java programming languages respectively (see section B.2 of appendix B for listing of implemented code).

A Naive-Bayes classifier is flexible as it allows semi-supervised or supervised learning. In other words, the classifier can actively learn using unlabeled data or it can learn using labeled examples. The presented implementation uses a supervised learning method to train the classifier, since precise fault labels are required for the application. Hence, the training examples used here consist of the features (harmonics) of the recorded shaft-voltage signal and a label corresponding to the condition under which the signal was recorded. This simply means that the classifier is given examples of numerical characteristics of the shaft-voltage signal for healthy and different fault conditions. An example of the training format is given in section B.2.3 of appendix B.

In order to test the functionality of the classifier, training data are firstly generated using the 2-D FE model of the synchronous generator. Instances of shaft voltages are recorded for various simulated conditions. Descriptions of these conditions are given in table 6.1. Each of these scenarios are simulated with rated

Table 6.1: Description of scenarios simulated with FE model to obtain shaft-voltage data for training the classifier

Scenario label	Condition	Description
Healthy	Normal	No eccentricity
Eccentricity	Fault	$0.5\,mm$ Static eccentricity ($8\,\%$ air-gap)
Rotor Short	Fault	Field-winding inter-turn short circuit ($2\,turns$)

speed ($3000\,rpm$) under no-load and with-load ($5\,\Omega$) conditions. Additionally, the field excitation (I_f) is varied about a set operating point of $40\,A$ within a maximum range of $\pm 0.5\,A$. The purpose of introducing variations in the excitation is to simulate - as far as possible - the practical effects of a non-deal current source and voltage regulation on a generator.

An independent set of instances are simulated for cross-validation purposes which assess the performance of the classifier [148]. Figures 6.8 and 6.9 (below) illustrate the results obtained from training and testing the classifier, using simulated data, under no-load and loaded conditions, respectively. These figures show scatter plots of each instance in terms of the three different labels predicted by the classifier, according to one of the instance's features - i.e. the sixth harmonic.

It should be noted that the distance between points along the y-axis does not reflect on the class probability and is artificially separated for visual purposes. Only the region in which each point lies is significant and corresponds to a specific class label - i.e. Healthy: $0-1$, Eccentricity: $1-2$, Rotor winding short: $2-3$. In fact, the implemented classifier only outputs a single number corresponding to each class label. A "Jitter" function is used for random vertical displacement, with the assigned class region, to reduce point concentration and improve identification of individual instances [149]. Additionally, these predictions are plotted against the sixth harmonic only, while the classifier uses a total of 10 different harmonics in its prediction.

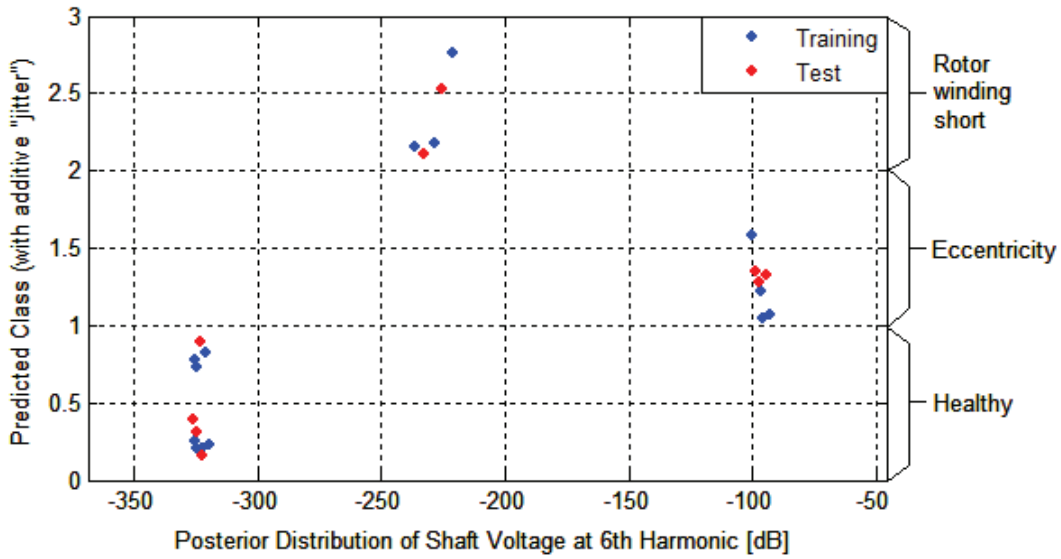


Figure 6.8: Scatter plot of simulated instances (without a load) illustrating relationship between the predicted class labels and posterior distribution of the shaft voltage's sixth harmonic feature only ("Jitter" is applied to Y-axis to reduce point concentration for presentation purposes).

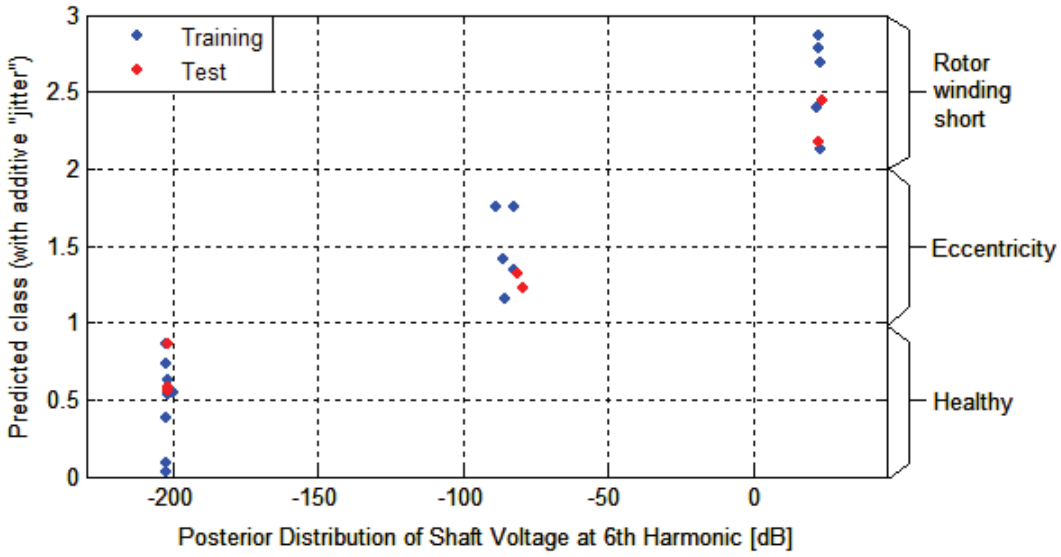


Figure 6.9: Scatter plot of simulated instances (with a load) illustrating relationship between the predicted class labels and posterior distribution of the shaft voltage's sixth harmonic feature only ("Jitter" is applied to Y-axis to reduce point concentration)

The clustering of points in specific areas in figures 6.8 and 6.9 indicate the relationship between the harmonic and each condition. For these cases, the relationship between the condition and the sixth harmonic is significant in assisting the classifier to distinguish between each instance and to correctly predict the class. Healthy instances correspond to the lowest magnitude of the sixth harmonic under both no-load and with-load conditions.

Experimental training and test data are obtained using the experimental generator under the same conditions as the simulated cases. Results from the classification of the experimental data are given in figures 6.10, 6.11 and 6.12 (below). As with the simulated cases, the classifier predicts each experimental instance correctly. Additionally, 6.12 shows the relationship between the condition and the sixth harmonic. Although this feature is not as distinct as the sixth harmonic, it still contributes to the overall classification and probability calculations. As previously mentioned, the implemented algorithm calculates a probability distribution for every classified instance. An example of the calculated probability distribution of the test instances used in the experimental case (no-load) is given in table 6.2 (below). The presented distributions indicate that each prediction is carried out with a high degree of certainty and precision.

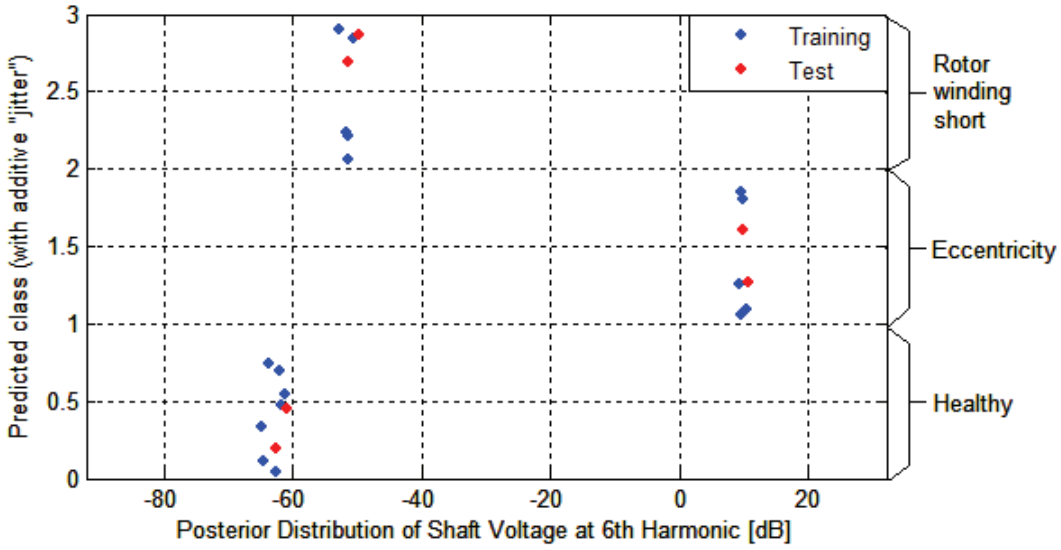


Figure 6.10: Scatter plot of experimental instances (without a load) illustrating relationship between the predicted class labels and posterior distribution of the shaft voltage's sixth harmonic feature only ("Jitter" is applied to Y-axis to reduce point concentration)

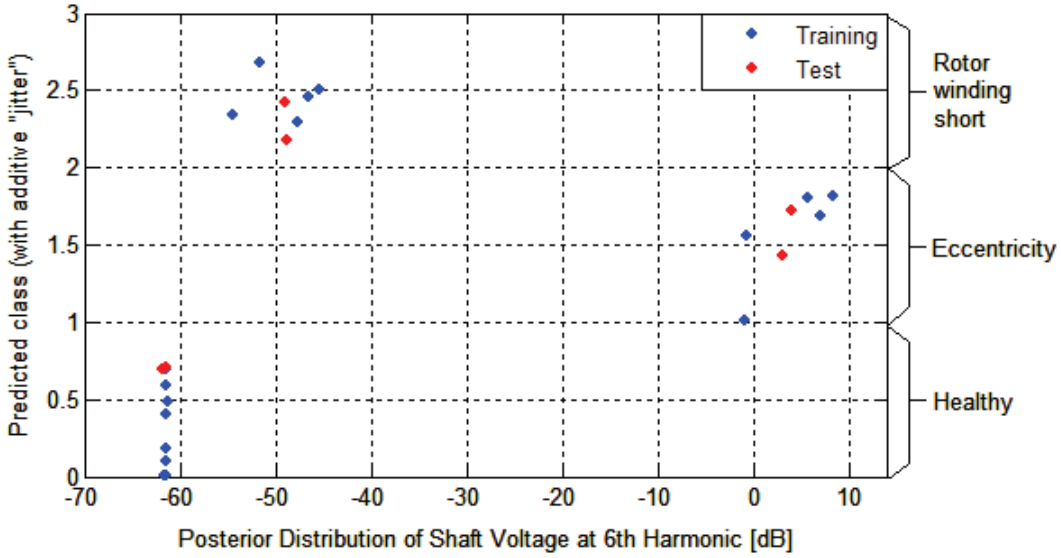


Figure 6.11: Scatter plot of experimental instances (with a load) illustrating relationship between the predicted class labels and posterior distribution of the shaft voltage's sixth harmonic feature only ("Jitter" is applied to Y-axis to reduce point concentration)

Table 6.2: Probability distribution of test instances, obtained using the experimental generator with a load, over predicted classes

Test Instance	Predicted class probability		
	Healthy	Eccentricity	Rotor Short
1	1	3.9007e-060	1.5941e-090
2	1	3.0128e-059	1.3895e-090
3	0	1	0
4	0	1	0
5	4.83e-203	3.1084e-144	1
6	1.8074e-197	9.4305e-140	1

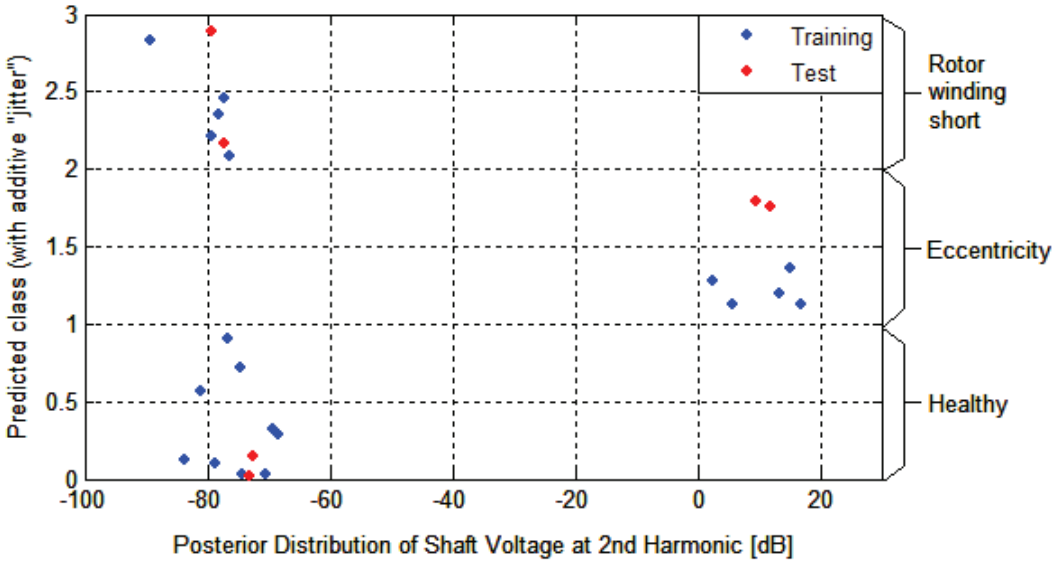


Figure 6.12: Scatter plot of experimental instances (without a load) illustrating relationship between the predicted class labels and posterior distribution of the shaft voltage's second harmonic feature only ("Jitter" is applied to Y-axis to reduce point concentration)

6.5 Testing and Validation of System

The testing and validation of the overall functionality of the presented shaft-voltage-based condition-monitoring system was carried out. Firstly, the system was tested using a heterogeneous data set consisting of simulated instances of

shaft-voltage recordings under healthy, eccentricity fault and field-winding short-circuit fault conditions. This mixed data set also consists of instances with the generator under no-load and load conditions. The purpose of have a mixed set of instances is to test the accuracy of the system over a wide range of possible conditions.

Thereafter, each of the aforementioned conditions were reproduced on the experimental setup and the system was again tested. It was found that once the fault-detection system had detected an anomaly, the diagnostics algorithm correctly classified the instance in both the simulated and experimental cases. The training instances are shown together with the test predictions, for the simulated cases, in figure 6.13, in relation to the posterior distribution of the shaft voltage's sixth harmonic. A total of 48 simulation cases are used - i.e. 32 training instances and 16 test instances. Experimental training instances and test predictions are given in figures 6.14, 6.15 and 6.16 (below) in relation to the posterior distributions of the shaft voltage's sixth, third and tenth harmonics. A total of 48 experimental are used - i.e. 36 training instances and 12 test instances.

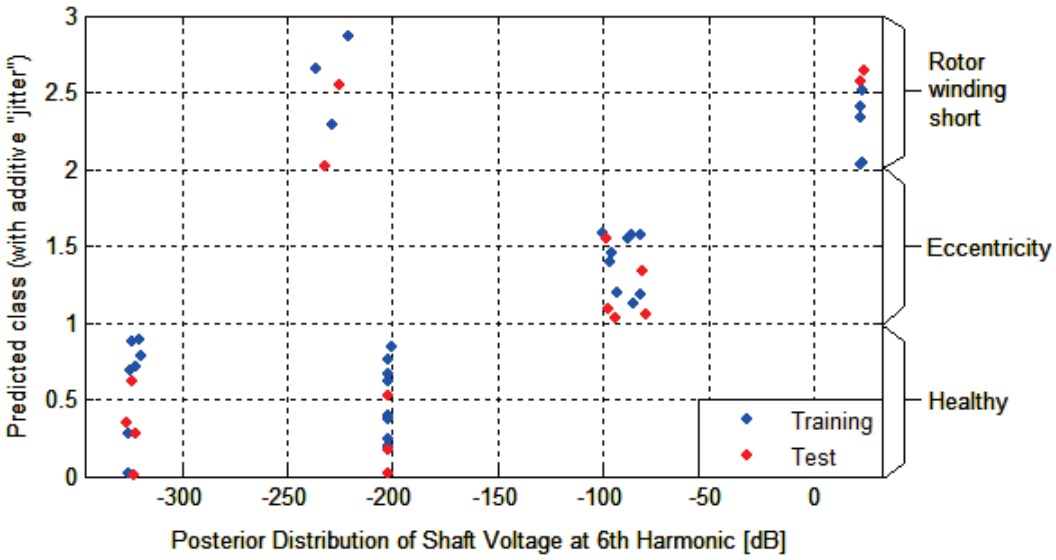


Figure 6.13: Scatter plot of heterogeneous simulated instances (with and without a load) illustrating relationship between the predicted class labels and posterior distribution of the shaft voltage's sixth harmonic feature only ("Jitter" is applied to Y-axis to reduce point concentration)

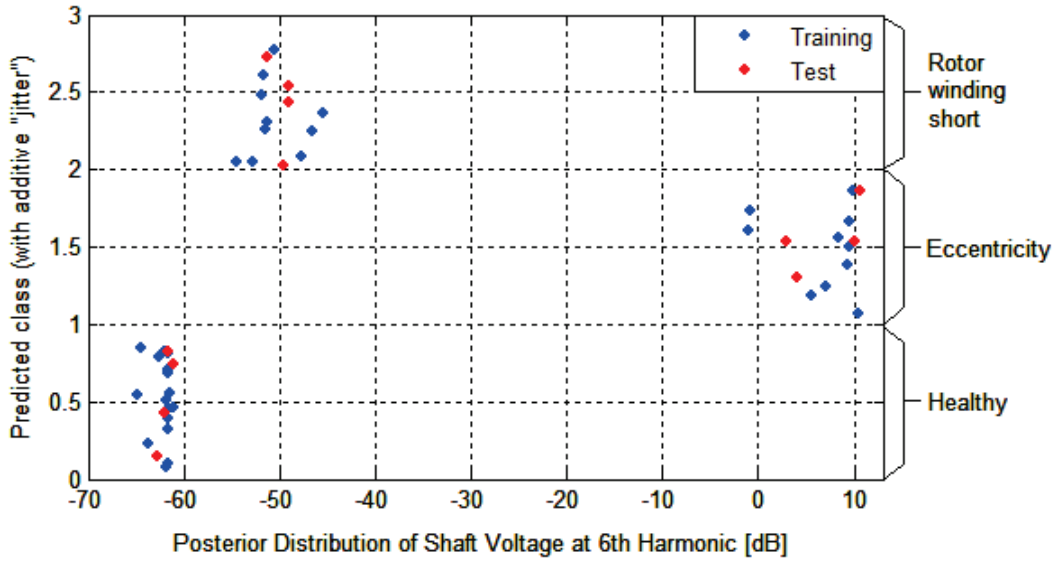


Figure 6.14: Scatter plot of heterogeneous experimental instances (with and without a load) illustrating relationship between the predicted class labels and posterior distribution of the shaft voltage's sixth harmonic feature only ("Jitter" is applied to Y-axis to reduce point concentration)

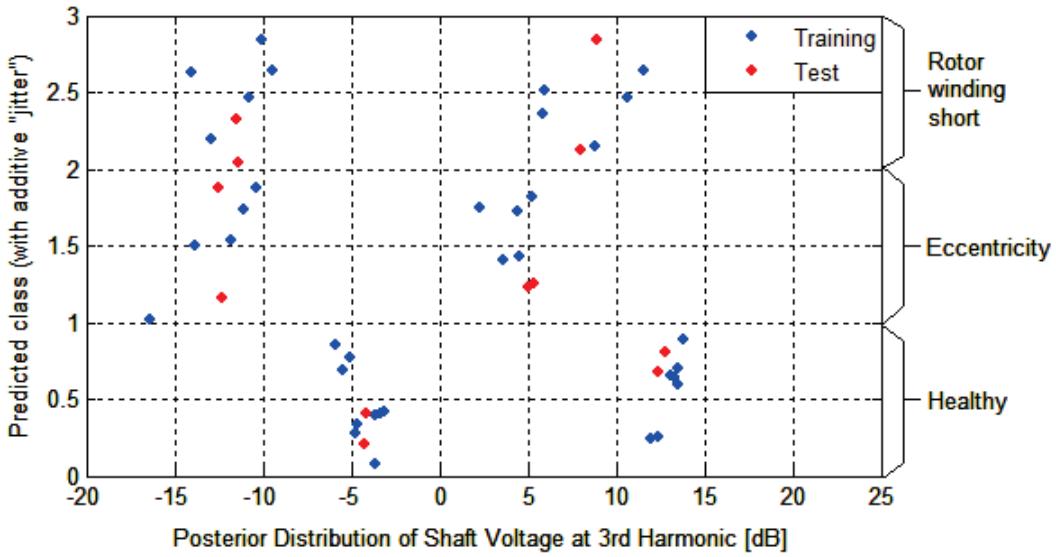


Figure 6.15: Scatter plot of heterogeneous experimental instances (with and without a load) illustrating relationship between the predicted class labels and posterior distribution of the shaft voltage's third harmonic feature only ("Jitter" is applied to Y-axis to reduce point concentration)

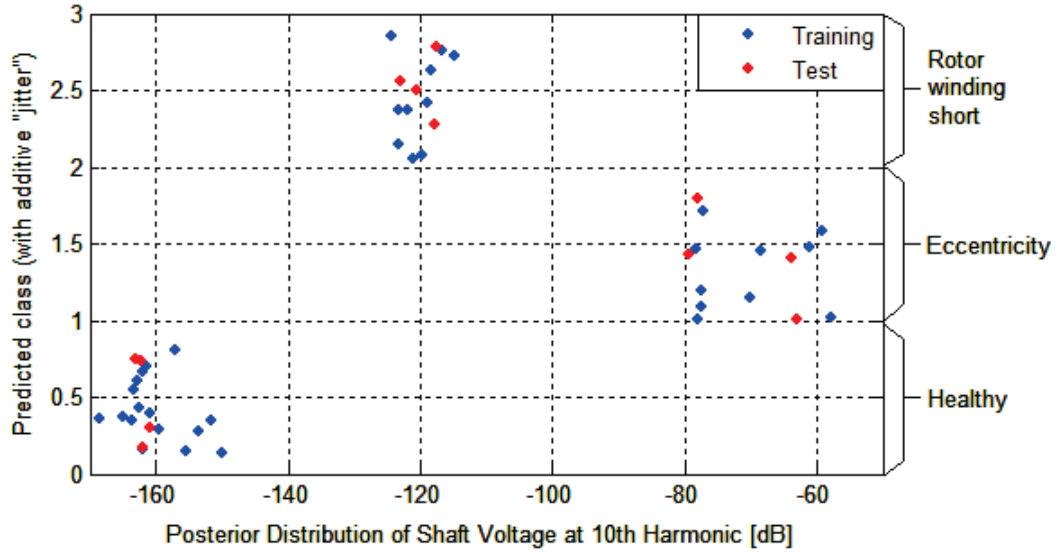


Figure 6.16: Scatter plot of heterogeneous experimental instances (with and without a load) illustrating relationship between the predicted class labels and posterior distribution of the shaft voltage's tenth harmonic feature only ("Jitter" is applied to Y-axis to reduce point concentration)

Besides validating the accuracy of instance classification, the results presented in figures 6.14, 6.15 and 6.16 also allow for additional inferences to be made about the behaviour of shaft-voltage harmonics under each condition. Figure 6.15 shows that the shaft voltage's third harmonic ($150\,Hz$) is less responsive to a change in the machine's condition than the sixth ($300\,Hz$) and tenth ($500\,Hz$) harmonics. This does not imply that the third harmonic is a redundant feature, as the classifier utilises all features to correctly predict the unknown class. Furthermore, this inference is valid for the investigated healthy, eccentricity fault and field-winding inter-turn short-circuit fault conditions, and may not be the case for other fault types. The use of additional features does, however, allow for the potential broadening of the system's fault-identification range. Broadening the range of training examples will improve the classifier's fault-identification range. Large training sets are not readily available in industrial applications, as it is impractical to implement faults under controlled conditions. The presented shaft voltage model can be used to generate data sets for training provided that the FE model is accurate. It is also possible to further develop the classifier with training data recorded over a period of time through logging of faults and problems, during planned maintenance. The presented classifier allows for continuous learning, as unidentified faults can be recognised and added to the list of probable classes.

6.6 Conclusion

A fault-diagnosis subsystem which uses shaft voltages is presented. The subsystem itself consists of two major components: feature extraction and fault classification. The feature-extraction algorithm determines the posterior distribution of the shaft-voltage signal at each harmonic. These features or characteristics are used by the fault classifier. A performance evaluation of the Bayesian spectrum-estimation technique, in comparison to three other widely-used signal-processing techniques, shows that it is most suited to the presented application. Results of the investigation indicate that the Bayesian technique is robust against noise, mitigates spectral leakage (precise frequency estimation), and has good fault resolution. The fault-classification system uses the Naive-Bayes probabilistic classifier, as it not only assigns a class label, but also provides a quantifiable certainty with its prediction.

The classification system has been implemented, trained and validated using data obtained from the simulation model and experimental system. The complete system has also been tested and validated on the experimental synchronous generator for healthy and fault cases. Results show that the fault-diagnosis subsystem is able to automatically provide accurate prediction of the condition of the machine. Furthermore, the presented fault-diagnosis solution enables inference of new behavioural information regarding shaft voltages which is otherwise not obtainable.

Chapter 7

General Conclusions

This chapter gives a complete overview and presents general conclusions of the research presented in this thesis. This is followed by a summary of the most significant contributions of the work and suggestions for further research.

7.1 Research Overview

The general goal of the work presented in this thesis is to improve shaft-voltage-based condition monitoring for application on 2-pole synchronous generators. A literature review showed that although shaft voltage is recognised as a potential candidate for incipient fault diagnosis, the limitations in the modelling, processing and analysis thereof, has hindered its application in condition monitoring. The absence of a practical method for modelling shaft voltages is due to uncertainty about physical interpretation and inception mechanisms. Furthermore, there is insufficient qualitative and quantitative evidence of the merits of shaft-voltage-based fault diagnosis. This is mainly due to inadequate processing techniques and a lack of inferential methods for extracting useful information from a shaft-voltage signal.

The major objectives of this research, listed in chapter 1, address each of the aforemetioned issues. The work carried out in this thesis may be summarised, with respect to the objectives, as follows:

1. A general framework for developing condition-monitoring systems was presented. This framework is intended to provide a systematic approach to developing a condition-monitoring system for electrical rotating machines. The impacts of system design on different maintenance strategies and the life of machines were investigated. Common failure mechanisms and cascading processes of faults were described to emphasise the importance of incipient fault diagnosis in practising predictive maintenance. A modern architecture for condition-monitoring systems consisting of three main subsystems - measurement modality, pre-processing and intelligence - was also presented.

2. A method for predicting shaft voltages in synchronous generators was semi-analytically derived through combining the concept of shaft-voltage mea-

surement with fundamental electromagnetic principles. This method was then implemented using a 2-D FE model of a synchronous generator. Shaft-voltage data obtained from simulations of various machine conditions were compared to experimental results, in order to test the validity of the model.

3. A method which uses the Cramér-Rao Lower Bound (CRLB) was designed for selecting optimal measurement modality. This selection method was used to qualitatively and quantitatively assess the merits of using shaft voltages as a measurement modality in fault diagnosis. A comparison was made between the shaft-voltage and flux-probe techniques in the diagnosis of static eccentricity.

4. The uncertainty and limitations of the current processing and analysis methods used for shaft voltage based diagnosis were identified. Hence, fault detection and diagnosis subsystems were specified to provide an intelligent and automated solution for practical application.

5. A fault-detection subsystem was designed, implemented and tested. The detection algorithm uses principle component analysis (PCA) to provide reduction in data dimensionality while retaining critical information on variation in the raw data. This subsystem enables online fault detection, avoidance of false alarms and prevention of unnecessary iterations through the fault-diagnosis algorithm during normal operation.

6. An intelligent and automated fault-diagnosis subsystem was designed, implemented and tested. The Bayesian spectrum estimation was determined to be the most suitable candidate for the presented application by comparison with three other widely-used techniques. This estimation technique is used in an algorithm to extract features of the shaft-voltage signal for fault classification. The Naive-Bayes probabilistic classifier is used, as it provides the degree of certainty to which a fault is predicted.

7.2 Conclusions and Significance of Research

In chapter 2, it was found that no systematic method of developing and selecting a modern condition-monitoring system is available. Therefore, a general framework which uses a bottom-up approach for this purpose was proposed. The proposed methods not only take into consideration fundamental maintenance philosophy, but also propose a modern architecture for condition-monitoring systems. This framework is generalised to enable its use in most condition-monitoring applications. Additionally, the importance of the ability of a condition-monitoring system to address incipient faults, was also described. The proposed modular architecture allows for each subsystem or subcomponent of a new or existing condition-monitoring system to be optimised.

In chapter 3, the shortcomings of the current shaft-voltage theory were described. The main deficiency in the theory comes from an uncertainty with regard to the physical interpretation of the shaft voltages. A novel semi-analytical method for modelling shaft voltages and addressing this major limitation in fundamental theory, has been presented. Essentially, the shaft voltage is proven to be the rate of change of the net flux through a specific loop and surface on the synchronous generator. Previously, a direct derivation was not possible and this finding represents a significant contribution to the fundamental theory of shaft voltages in synchronous generators. Practical implementation of the method is also carried out using an FE model. Testing of the model yielded some important findings. One such finding was that the rotor end-windings of the machine make a negligible contribution, of approximately 1 %, to the overall shaft-induced voltage. Manufacturing imperfections and inherent asymmetries were also found to be main contributors to the production of shaft voltages on a synchronous generator. This finding explains why shaft voltages vary under fault conditions. Results obtained from model simulations and experimental measurements both indicate that there is a significant rise in the sixth harmonic of the shaft voltage for a static eccentricity fault.

Chapter 4 dealt with uncertainty in the measurement modality and fault-diagnosis components of shaft-voltage-based condition monitoring. A novel technique for

comparing measurement modalities has been provided, which uses the CRLB for assessing measurement modalities and takes into account measurement noise and parameter uncertainties. Currently, there is no definitive method for assessing the early failure detection capabilities of a measurement modality, and this method represents a unique contribution to the field of condition monitoring. In the thesis, the method is used to compare the error of the shaft-voltage and flux-probe techniques in identifying static eccentricity faults. The result of this investigation is that the shaft-voltage technique is more suited to diagnosing this type of fault than the widely-used flux-probe technique. Additionally, this chapter also described how a machine-learning approach can be used to solve the target function of a fault-diagnosis system.

Chapters 5 and 6 presented the fault-detection and fault-diagnosis subsystems respectively. The fault-detection algorithm uses PCA and the fault-diagnosis algorithm uses Bayesian spectrum analysis and classification. Both subsystems were tested using simulation data and experimental measurements. The fault-detection algorithm uses an adapted PCA method and monitors both the Hotelling T^2 and Q residuals statistics to evaluate variations in a multi-parameter model comprising the excitation current, stator voltages and shaft voltage. This is a novel approach to online fault detection on electrical rotating machines. Results from testing of the fault-detection algorithm are that the subsystem is able to accurately identify anomalies in the machine's condition, and can also distinguish acute load variations and thus avoid false alarms. The Bayesian spectrum estimation technique was compared to the widely-used Periodogram, Welch and MUSIC techniques before implementation in the fault-diagnosis algorithm. Results of the comparison indicated that the Bayesian technique is most suited to the application, as it is robust against noise, mitigates spectral leakage (precise frequency estimation), and has good fault resolution. The Naive-Bayes classifier was implemented, trained and tested to provide high accuracy in predicting healthy, rotor-winding short-circuit faults, and static eccentricity faults. Furthermore, this machine-learning solution provides inference of new behavioural information about shaft voltages which is otherwise not obtainable.

Many power-generation plants depend on ageing units, which are not easily replaced due to the cost of new installations. Furthermore, newer installations have different monitoring requirements with the advancement of machine design, power electronics, control, and automation. This research is important in satisfying the monitoring requirements of ageing units, but it is also a vital step towards addressing the requirements for modern condition-monitoring systems.

7.3 Further Research

Completion of this research revealed some areas that merit further research. The following topics are suggested for further research are considered to have potential to contribute to the field of condition monitoring in electrical rotating machines.

7.3.1 Extension of Presented Methodologies

The presented shaft-voltage simulation method was implemented for a specific experimental synchronous generator. As mentioned in Chapter 3, this generator is designed to accommodate a specific range of faults. It is therefore recommended that this method be implemented and tested using a different experimental generator - which is designed to accommodate a wider variety of faults, in a controlled manner. Additionally, the stator of this machine should use formed coils for comparison with shaft voltages obtained on a machine with a mush-wound stator. Simulation and measurement over an extended range of faults will also improve knowledge of the behaviour shaft voltages. Furthermore, a different experimental machine with an extended fault range will enable testing of the fault detection and diagnosis subsystems, which were specifically developed for flexible application and to enable continuous fault learning on any synchronous generator.

Another related topic to be considered for future research is simultaneous fault conditions on a synchronous machine. This is a condition where multiple faults occur at the same time on a machine - e.g. stator-winding short-circuit and field-winding short-circuit faults. The effects of simultaneous faults on the measurement modality can be investigated. A machine which allows implementation of a wider variety of faults will assist with this investigation. It is believed that the presented

classification system can help with such an investigation by learning to distinguish between two or more simultaneous fault conditions.

In chapter 3, the end-windings of the synchronous generator were found to make a negligible contribution to shaft-induced voltages. However, the results indicated that most of the contribution was to the higher frequency harmonics. Therefore, further investigation of the end-windings using a 3D implementation of the presented method and a machine which can accommodate end-winding faults, is suggested. A 3D implementation, although expensive, would also enable the presented simulation method to be used for model-based fault diagnosis.

The PCA fault-detection algorithm was adapted for use on a rotating eletrical machines. Before the Hotelling T^2 and Q residuals statistics are processed, the model is regularised and therefore enables addition of supplementary parameters. The shaft voltage may be substituted, if not available on another machine, but the new parameter should be suitably sensitive to the fault. This implies that the fault detection method can be implemented on other applications and perhaps other machines. Therefore, this method is recommended for other applications as it will assist in improving the overall efficiency and accuracy of the machine's condition monitoring system.

7.3.2 Industry Application

Industrial application will significantly assist further development of the proposed system. This may require an industrial partner or in-house research - due to intellectual property policies usually adopted by utilities. Firstly, this will enable a better understanding of utilities' maintenance practice and failure mechanisms experienced on turboalternators. Secondly, shaft-voltage measurements and detailed design specifications for generators operated by utilities at a power station will help optimise the presented simulation method. Additional sources of shaft voltages - only experienced in power stations - such as the separation of charge when wet steam flows through the turbine blades, may be quantified. Field testing of the complete system on a large turboalternator will also contribute to evaluation

and optimisation of the fault-detection and fault-diagnosis systems for practical application.

7.3.3 Diversifying Application of Novel Methods

Some of presented methods have not been applied previously in the field of condition monitoring of electrical rotating machines. The CRLB-based selection technique was proposed as a means of quantitatively and qualitatively assessing measurement modalities. It is suggested that this method be applied for other measurement modalities such as vibration and temperature. For example, the method could be applied to selecting optimal position for sensor placement on an electrical motor - by evaluating the sensitivity of each measurement to a rise in temperature.

It is also suggested that the Bayesian spectrum-estimation technique be used for other fault-diagnosis applications. The technique is extremely robust against noise and performs well with a smaller number of samples. It should also be mentioned that this technique can perform spectrum estimation using unevenly sampled non-stationary data [150]. In other words, this method may be adapted to work regardless of how the signal samples are spaced. Examples of application areas are: vibration, current-signature, and magnetic-flux analysis in condition monitoring.

References

[1] P. Nippes, "Early warning of developing problems in rotating machinery as provided by monitoring shaft voltages and grounding currents," *IEEE Transactions on energy conversion*, vol. 19, no. 2, June 2004.

[2] P. J. Tavner, L. Ran, J. Penman, and H. Sedding, "Condition monitoring of rotating electrical machines," *IET Power and Energy Series*, vol. 56, pp. 219 - 221, 2008.

[3] P. Tavner, "Review of condition monitoring of rotating electrical machines," *IET Electric Power Applications*, vol. 2, no. 4, pp. 215 - 247, July 2008.

[4] J. L. Kohler, J. Sottile, and F. C. Trutt, "Condition-based maintenance of electrical machines," *IEEE Industry Applications Conference Thirty-Fourth IAS Annual Meeting*, vol. 1, pp. 205 - 211, 1999.

[5] S. J. Hoffe, "Synchronous generator fault diagnosis using shaft signal measurements," *MSc. Dissertation*, University of the Witwatersrand, Johannesburg, South Africa, 2006.

[6] D. de Canha, W. A. Cronje, A. Meyer, and S. J. Hoffe, "Methods for diagnosing static eccentricity in a 2 pole generator," *IEEE Powertech*, Paper ID 528, 2007.

[7] Y. Wu, Y. Li, and H. Li, "Diagnosis of turbine generator typical faults by shaft voltage," *IEEE Industry Applications Society Annual Meeting (IAS)*, Las Vegas, Nevada, October 2012.

[8] W. Doorsamy, W. Cronje, and A. Meyer, "Multiple fault diagnosis on a synchronous 2 pole generator using shaft and flux probe signals," *IEEE In-*

ternational Conference on Industrial technology (ICIT), Cape Town, South Africa, pp. 362 - 367, Feb. 2013.

[9] P. Waide and C. U. Brunner, "Energy-efficiency policy opportunities for electric motor-driven systems," *International Energy Agency*, Paris, France, 2011.

[10] I. E. Agency, "How will global energy markets evolve to 2035?" *World Energy Outlook Factsheet*, Paris, France, 2013.

[11] C. Carson, S. Barton, and F. Echeverria, "Immediate warning of local overheating in electric machines by the detection of pyrolysis products," *IEEE Transactions on Power Apparatus and Systems*, vol. PAS-2, no. 2, pp. 532 - 542, March 1973.

[12] S. A. Mortazavizadeh and S. M. G. Mousavi, "Review on condition monitoring and diagnostic techniques of rotating electrical machines," *Physical Science International Journal*, vol 4, no. 3, pp. 310-338, 2014.

[13] T. Sorita, S. Minami, H. Adachi, M. Takashima, and S. Numata, "The detection of degraded materials in turbine generators by chemical analysis," *IEEE International Symposium on Electrical Insulating Materials*, pp. 751 - 754, September 1998.

[14] H. W. Whittington, B. W. Flynn, and G. H. Mills, "An on-line wear debris monitor," *Measurement Science and Technology*, vol. 3, no. 7, pp. 656 - 61, July 1992.

[15] O. Lloyd and A. F. Cox, "Monitoring debris in turbine generator oil," *Wear*, vol. 71, no. 1, pp. 79 - 91, September 1981.

[16] C. P. Potter, "Measurement of temperature in general purpose squirrel-cage induction motors," *Electrical Engineering*, vol. 58, no. 9, pp. 468 - 477, September 1939.

[17] J. Ramussen and C. Tuttle, "Early detection of internal stator winding faults using rotor-mounted infrared sensors," *IEEE International Conference on Electrical Machines and Drives*, pp. 800 - 802, May 1999.

[18] P. Milanfar and J. Lang, "Monitoring the thermal condition of permanent-magnet synchronous motors," *IEEE Transactions on Aerospace and Electronic Systems*, vol. 32, no. 4, pp. 1421 - 1429, October 1996.

[19] M. Ganchev, B. Kubicek, and H. Kappeler, "Rotor temperature monitoring system," *International Conference on Electrical Machines (ICEM)*, pp. 1 - 5, September 2010.

[20] A. Boglietti, A. Cavagnino, D. Staton, M. Shanel, M. Mueller, and C. Mejuto, "Evolution and modern approaches for thermal analysis of electrical machines," *IEEE Transactions on Industrial Electronics*, vol. 56, no. 3, pp. 871 - 882, March 2009.

[21] F. Qi, M. Schenk, and R. W. DeDoncker, "Discussing details of lumped parameter thermal modeling in electrical machines," *IET International Conference on Power Electronics, Machines and Drives (PEMD)*, pp. 1 - 6, April 2014.

[22] P. H. Mellor, D. Roberts, and D. R. Turner, "Lumped parameter thermal model for electrical machines of tefc design," *IEE Proceedings B - Electric Power Applications*, vol. 138, no. 5, pp. 205 - 218, September 1991.

[23] M. Tsypkin, "Induction motor condition monitoring: vibration analysis technique - a practical implementation," *IEEE International Conference on Electrical Machines and Drives*, pp. 406 - 411, May 2011.

[24] M. R. Bissonnette, "End-winding vibration monitoring and interpretation," *IEEE International Symposium on Electrical Insulation (ISEI)*, pp. 285 - 290, June 2012.

[25] A. J. Ellison and S. J. Yang, "Effects of rotor eccentricity on acoustic noise from induction machines," *Proceedings of the Instituition of Electrical Engineers*, vol. 118, no. 1, pp. 174 - 184, January 1971.

[26] L. Wu, X. Huang, T. G. Habetler, and R. G. Harley, "Eliminating load oscillation effects for rotor eccentricity detection in closed-loop drive-connected

induction motors," *37th IEEE Power Electronics Specialists Conference (PESC)*, pp. 1 - 6, June 2006.

[27] O. V. Thorsen and M. Dalva, "Condition monitoring methods, failure identification and analysis for high voltage motors in petrochemical industry," *Eighth International Conference on Electrical Machines and Drives*, pp. 109 - 113 , September 1997.

[28] F. Britz, M. W. Degner, A. B. Diez, and J. M. Guerrero, "Online diagnostics in inverter-fed induction machines using high-frequency signal injection," *IEEE Transactions on Industry Applications*, vol. 40, no. 4, pp. 1153 - 1161, July/August 2004.

[29] G. C. Stone, "A perspective on online partial discharge monitoring for assessment of the condition of rotating machine stator winding insulation," *IEEE Electrical Insulation Magazine*, vol. 28, no. 5, pp. 8 - 13, September/October 2012.

[30] F. T. Emery, B. N. Lenderking, and R. D. Crouch, "Turbine-generator on-line diagnostics using rf monitoring," *IEEE Transactions on Power Apparatus and Systems*, vol. PAS-100, pp. 4974 - 4982, December 1981.

[31] A. Pedersen, G. C. Crichton, , and I. W. McAllister, "The theory and measurement of partial discharge transients," *IEEE Transactions on Electrical Insulation*, vol. 26, no. 3, pp. 487 - 496, June 1991.

[32] M. A. Cash and T. G. Habetler, "Insulation failure detection in the stator windings of asd-driven induction machines using standard deviation of line currents," *IEEE Thirty-Third IAS Annual Meeting Industry Applications Conference*, vol. 1, pp. 299 - 303, October 1998.

[33] M. Arkan and P. J. Unsworth, "Stator fault diagnosis in induction machines using power decomposition," *IEEE Thirty-Fourth IAS Annual Meeting Industry Applications Conference*, vol. 3, pp. 1908 - 1912, October 1999.

[34] J. Jung, J. Lee, and B. Kwon, "Online diagnosis of induction motors using

mcsa," *IEEE Transactions on Industrial Electronics*, vol. 53, no. 6, pp. 1842 - 1852, December 2006.

[35] J. Penman, M. N. Dey, A. J. Tait, and W. E. Bryan, "Condition monitoring of electrical drives," *IEE Proceedings B on Electric Power Applications*, vol. 133, no. 3, pp. 142 - 148, May 1986.

[36] H. Henao, C. Demian, and G. A. Capolino, "A frequency-domain detection of stator winding faults in induction machines using an external flux sensor," *IEEE Transactions on Industrial Applications*, vol. 39, no. 5, pp. 1272 - 1279, September/October 2003.

[37] R. Ong, J. Dymond, R. Findlay, and B. Szabados, "Shaft current in ac induction machine - an online monitoring system and prediction rules," *IEEE Transactions on Energy Conversion*, vol. 37, no. 4, pp. 1189 - 1196, August 2001.

[38] D. R. Rankin and I. Wilson, "The use of shaft voltage to detect air gap eccentricity and shorted turns in salient pole alternators," *IEEE 7th International Conference on Electrical machines and Drives*, pp. 194 - 197, September 1995.

[39] F. Filippetti, G. Franceschini, C. Tassoni, and P. Vas, "Recent developments of induction motor drives fault diagnosis using ai techniques," *IEEE Transactions on Energy Conversion*, vol. 47, no. 5, pp. 994 - 1004, October 2000.

[40] X. Dang, N. Tai, and J. Liu, "Stator winding's inter-turn fault intelligent diagnosis in large turbo-generator by elman neural network," *IEEE International Conference on Advanced Power System Automation and Protection (APAP)*, pp. 763 - 768, October 2008.

[41] R. M. Bharadwaj, A. J. Parlos, A. H. Toliyat, and S. K. Menon, "A neural network-based speed filter for induction motors: Adapting to motor load changes," *IEEE International Joint Conference on Artificial Neural Networks*, vol. 5, pp. 3447 - 3450, July 1999.

[42] J. Schneider, C. Neumann, J. Hografer, W. Wellssow, M. Schwan, and A. Schnettler, "Asset management techniques," *15th Power Systems Computation Conference*, pp. 1 - 11, August 2005.

[43] F. Parasiliti and P. Bertoldi, *Energy efficiency in motor-driven systems*, Springer, Germany, 1st Ed, 2003.

[44] M. Miman and E. A. Pohl, "Uncertainty assessment for availability: importance measures," *Annual Reliability and Maintainability Symposium (RAMS)*, pp. 222 - 227, January 2006.

[45] P. Tavner, B. Gaydon, and D. Ward, "Monitoring generators and large motors," *IEE Proceedings, Part B, Electric Power Applications*, vol. 133, no. 3, pp. 169 - 180, May 1986.

[46] L. Agrawal and S. Tripathi, "Study of fault detecting techniques in electrical machines," *VSRD International Journal of Electrical, Electronics and Communication Engineering*, vol. 1, no. 8, pp. 478 - 489, 2011.

[47] M. Kaufhold, H. Auinger, M. Berth, J. Speck, and M. Eberhardt, "Electrical stress and failure mechanism of the winding insulation in pwm-inverter-fed low-voltage induction motors," *IEEE Transactions on Industrial Electronics*, vol. 47, no. 2, pp. 396 - 402, April 2000.

[48] T. K. Mandal, "Study on health assessment of generator winding insulation," *IEEE Symposium on Electric Ship Technologies*, pp. 468 - 477, 2005.

[49] L. Yonggang, L. Jianwen, and S. Wei, "On-line fault detection of inter-turn short circuits in turbo-generator rotor windings," *IEEE International Conference on Electrical Machines and Systems*, pp. 763 - 768, October 2008.

[50] R. Fisser, D. Makuc, H. Lavric, D. Miljavec, and M. Bugeza, "On-line fault detection of inter-turn short circuits in turbo-generator rotor windings," *Modelling, analysis and detection of rotor field winding faults in synchronous generators*, pp. 1 - 6, September 2010.

[51] S. Wang, L. Heming, L. Yonggang, and Y. Wang, "The diagnosis method of generator rotor winding inter-turn short circuit fault based on excitation cur-

rent harmonics," *IEEE 5th International Conference on Power Electronics and Drives Systems*, vol. 2, pp. 1669 - 1673, November 2003.

[52] A. Smith, D. Bertenshaw, C. Ho, T. Chan, and M. Sasic, "Detection of stator core faults in large turbo-generators," *IEEE International Conference on Electrical Machines and Drives*, vol. 3, pp. 763 - 770, May 2009.

[53] R. Romary, C. Demian, P. Schlupp, and J. Roger, "Off-line and on-line methods for stator core fault detection in large generators," *IEEE Transactions on Industrial Electronics*, vol. 60, no. 9, pp. 4084 - 4092, September 2013.

[54] H. Arabaci and O. Bilgin, "Efficiency analysis of submersible induction motor with broken rotor bar," *Transactions on Engineering Technologies*, pp 27-40, July 2014.

[55] B. Mirafzal and N. A. O. Demerdash, "On innovative methods of induction motor interturn and broken-bar fault diagnostics," *IEEE Transactions on Industrial Electronics*, vol. 42, no. 2, pp. 405 - 414, March/April 2006.

[56] H. A. Toliyat and G. B. Kliman, *Handbook of electric motors*, Marcel Dekker, 2nd Ed, 2004.

[57] H. S. Swoyer, "Commutator and slip ring maintenance," *IEEE Transactions on Industrial and General Applications*, vol. IGA, no. 5, pp. 311 - 319, September 1965.

[58] R. D. Hall and R. P. Roberge, "Carbon brush performance on slip rings," *IEEE Paper and Pulp Industry Technical Conference*, pp. 1 - 6, June 2010.

[59] J. Faiz, B. M. Ebrahimi, and M. Valavi, "Mixed eccentricity fault diagnosis in salient-pole synchronous generator using modified winding function method," *Progress In Electromagnetics Research B*, vol. 11, pp. 155 - 172, 2009.

[60] S. Nandi, T. C. Ilamparithi, S. B. Lee, and D. Hyun, "Detection of eccentricity faults in induction machines based on nameplate parameters," *IEEE Transactions on Industrial Electronics*, vol. 58, no. 5, pp. 1673 - 1683 , May 2011.

[61] W. Saadaoui and K. Jelassi, "Induction motor bearing damage detection using stator current analysis," *Proceedings of the 2011 International Conference on Power Engineering, Energy and Electrical Drives*, pp. 1 - 6, May 2011.

[62] J. Z. Zhang and J. C. Chen, "Tool condition monitoring in an end-milling operation based on the vibration signal collected through a microcontroller-based data acquisition system," *The International Journal of Advanced Manufacturing Technology*, vol. 39, no. 2, pp. 118 - 128, October 2008.

[63] R. Maier, "Protection of squirrel-cage induction motor utilizing instantaneous power and phase information," *IEEE Transactions on Industry Applications*, vol. 28, no. 2, pp. 376 - 380, March/April 1992.

[64] J. Liu, W. Wang, and F. Golnaraghi, "An extended wavelet spectrum for bearing fault diagnostics," *IEEE Transactions on Instrumentation and Measurement*, vol. 57, no. 12, pp. 2801 - 2812, December 2008.

[65] L. A. Garcia-Escudero, O. Duque-Perez, D. Morinigo-Sotelo, M. Perez-Alonso, and R. Operadora, "Robust multivariate control charts for early detection of broken rotor bars in induction motors fed by a voltage source inverter," *Proceedings of the 2011 International Conference on Power Engineering, Energy and Electrical Drives*, pp. 1 - 6, May 2007.

[66] X. W. andV. L. Syrmos, "Fault detection, identification and estimation in the eha system using multiple model estimation," *IEEE Aerospace Conference*, pp. 1 - 10, March 2009.

[67] M. Delgado, J. C. Urresty, L. Albiol, J. A. Ortega, A. Garcia, L. Romeral, and E. Vidal, "Motor fault classification system including a novel hybrid feature reduction methodology," *37th Annual Conference on IEEE Industrial Electronics Society (IECON)*, pp. 2388 - 2393, November 2011.

[68] N. Nguyen, J. Kwon, and H. Lee, "Fault diagnosis of induction motor using decision tree with an optimal feature selection," *7th International Conference on Power Electronics*, pp. 729 - 732, October 2007.

[69] D. Singh, D. Kaur, and Y. Singh, "Condition monitoring leading to control by using fuzzy and hybrid fuzzy models: A review," *International Journal of Engineering and Advanced Technology (IJEAT)*, vol. 2, no. 2, pp. 199 - 206, December 2012.

[70] G. D'Antona, P. Pennacchi, and C. Pensieri, "Turboalternator shaft voltage measurements," *Applied Measurements for Power Systems (AMPS)*, pp. 1 - 4, September 2012.

[71] R. J. Corkins, "The importance of grounding brushes to the safe operation of large turbine generators," *IEEE Transactions on Energy Conversion*, vol. 3, no. 3, pp. 607 - 612, September 1988.

[72] C. Ammann, K. Reichert, R. Joho, and Z. Posedel, "Shaft voltages in generators with static excitation systems - problems and solutions," *IEEE Transactions on Energy Conversion*, vol. 3, no. 2, pp. 409 - 419, June 1988.

[73] F. Punga and W. Hess, "Bearing currents," *Ekbrotechnik and Maschinenbau*, vol. 25, pp. 615-18, August 1907.

[74] L. Berger, "Causes of bearing currents and their elimination," *La Lumiere Electrique*, vol. 11, pp. 268-17, August 1910.

[75] P. L. Alger and H. W. Samson, "Shaft currents in electric machines," *Transactions AIEE*, pp. 235-245, 1945.

[76] J. Boyd and H. N. Kaufman, "The causes and control of electrical currents in bearings," *Lubrication Engineering*, pp. 28-35, January 1959.

[77] ANSI/IEEE-C50.30, *IEEE guide for operation and maintenance of turbine generators*, IEEE, 1972.

[78] M. Costello, "Shaft voltages and rotating machinery," *IEEE Transactions on Industry Applications*, vol. 29, no. 2, pp. 71 -78, 1993.

[79] P. Nippes, D. David, and A. Peniazev, "Monitoring of shaft voltages and grounding current brushes," *EPRI Motor and Generator Predictive Maintenance and Refurbishment Conference*, Orlando, Florida, November 1993.

[80] J. Torlay, A. Foggia, C. Corenwinder, A. Audoli, , and J. Herigault, "Analysis of shaft voltages and circulating currents in the parallel-connected windings in large synchronous generators," *Electric Power Components and Systems*, vol. 30, no. 2, pp.135 - 149, 2002.

[81] I. Kerzenbaum, "Shaft currents in electric machines fed by solid-state drives," *IEEE Proceedings of Annual Industrial and Commercial Power Systems Technical Conference*, pp. 71 -79, 1992.

[82] A. D. Kiureghian, "Aleatory or epistemic? does it matter?" *Special Workshop on Risk Acceptance and Risk Communication*, Stanford University, March 2007.

[83] J. S. Sohre, "Shaft riding brushes to control electric stray currents," *Proceedings of Twentienth Turbomachinery Symposium*, pp. 63 - 75, 1991.

[84] P. I. Nippes and E. S. Galano, "Understanding shaft voltage and grounding currents of turbine generators," Magnetic Products and Services, Inc, Holmdel Press, Online: http://gaussbusters.com/resources/articles/.

[85] J. P. A. Bastos and N. Sadowski, *Electromagnetic modeling by finite element methods*, Marcel Dekker, 2003.

[86] L. W. Matsch and J. D. Morgan, *Electromagnetic and electromechanical machines*, John Wiley and Sons, Canada, 3rd ed., 1986.

[87] J. Pyrhonen, T. Jokinen, and V. Hrabocov, *Design of rotating electrical machines*, John Wiley and Sons, Canada, 1st ed., 2008.

[88] Y. Liao and T. A. Lipo, "Effect of saturation third harmonic on the perfomrance of squirrel cage induction machines," *Electric Machines and Power Systems*, vol. 22, no. 2, pp. 155 - 171, 1994.

[89] K. Gyftakis and J. Kappatou, "A novel and effective method of static eccentricity diagnosis in three-phase psh induction motors," *IEEE Transactions on Energy Conversion*, vol. 28, no. 2, pp. 405 - 412, 2013.

[90] D. Hyun, S. Lee, J. Hong, S. B. Lee, and S. Nandi, "Detection of airgap eccentricity for induction motors using the single-phase rotation test," *IEEE Transactions on Energy Conversion*, vol. 27, no. 3, pp. 689 - 696, 2012.

[91] S. Nandi, S. Ahmed, and H. Toliyat, "Detection of rotor slot and other eccentricity related harmonics in a three phase induction motor with different rotor cages," *IEEE Transactions on Energy Conversion*, vol. 16, no. 3, pp. 253 - 260, 2001.

[92] G. Crevecoeur, D. Baumgarten, U. Steinhoff, J. Haueisen, L. Trahms, and L. Dupré, "Advancements in magnetic nanoparticle reconstruction using sequential activation of excitation coil arrays using magnetorelaxometry," *IEEE Transactions on Magnetics*, vol. 48, no. 4, pp. 1313 - 1316, 2012.

[93] L. T. Rosenberg, "Eccentricity, vibration and shaft currents in turbine generators," *AIEE Transactions*, vol. 74, no. 3, pp. 38 - 41, January 1955.

[94] R. L. Stoll and A. Hennache, "Method of detecting and modelling presence of shorted turns in dc filed winding of cylindrical rotor synchronous machines using two airgap search coils," *IEEE Proceedings Electric Power Applications*, vol. 135, no. 6, pp. 281 - 294, 1988.

[95] D. Albright, "Interturn short-circuit detector for turbine-generator rotor windings," *IEEE Transactions on Power Apparatus and Systems*, vol. PAS-90, no. 2, pp. 478 - 483, 1971.

[96] B. Ebrahimi, M. Roshtkhari, J. Faiz, and S. Khatami, "Advanced eccentricity fault recognition in permanent magnet synchronous motors using stator current signature analysis," *IEEE Transactions on Industrial Electronics*, vol. 61, no. 4, pp. 2041 - 2052, 2014.

[97] P. Stoica, E. Larsson, and A. Gershman, "The stochastic crb for array processing: A textbook derivation," *IEEE Signal Processing Letters*, vol. 8, no. 5, pp. 148 - 150, 2001.

[98] A. Emery, A. Nenarokomov, and T. Fadale, "Uncertainties in parameter

estimation: The optimal experiment," *International Journal of Heat and Mass Transfer*, vol. 43, no. 18, pp. 3331 -3339, 2000.

[99] A. Abdallh, G. Crevecoeur, and L. Dupré, "Optimal needle placement for the accurate magnetic material quantification based on uncertainty analysis in the inverse approach," *Measurement Science and Technology*, vol. 21, no. 11, pp. 1 - 16, 2010.

[100] ——, "Selection of measurement modality for magnetic material characterization of an electromagnetic device using stochastic uncertainty analysis," *IEEE Transactions on Magnetics*, vol. 47, no.11, pp. 4564 - 4573, 2011.

[101] A. Abdallh and L. Dupré, "Magnetic material characterization using an inverse problem approach," *Advanced Magnetic Materials*, ISBN 978- 953-51-0637-1, InTech, 2012.

[102] T. Mthombeni, P. Pillay, and R. Strnat, "New epstein frame for lamination core loss measurements under high frequencies and high flux densities," *IEEE Transactions on Energy Conversion*, vol. 22, no.3, pp. 614 - 620, 2007.

[103] B. Vaseghi, S. Rahman, and A. Knight, "Influence of steel manufacturing on j-a model parameters and magnetic properties," *IEEE Transactions on Magnetics*, vol. 49, no. 5, pp. 1961 - 1964, May 2013.

[104] G. Strang, *Introduction to applied mathematics*, Cambridge, United Kingdom, Wellesley, 1986.

[105] T. Fadale, A. Nenarokomov, and A. Emery, "Uncertainties in parameter estimation: the inverse problem," *International Journal of Heat and Mass Transfer*, vol. 38, no. 3, pp. 511 - 518, 1995.

[106] A. Emery and A. Nenarokomovz, "Optimal experiment design," *Measurement Science and Technology*, vol. 9, no. 6, pp. 864 - 876, 1998.

[107] B. Radich and K. Buckley, "Eeg dipole localization bounds and map algorithms for head models with parameter uncertainties," *IEEE Transactions on Biomedical Engineering*, vol. 42, no. 3, pp. 233 - 241, 1995.

[108] S. Nandi, H. A. Toliyat, and X. Li, "Condition monitoring and fault diagnosis of electrical motors - a review," *IEEE Transactions on Energy Conversion*, vol. 20, no. 4, pp. 719 - 729, 2005.

[109] A. Abdallh, G. Crevecoeur, and L. Dupré, "Bayesian approach for stochastic modeling error reduction of magnetic material identification of an electromagnetic device," *Measurement Science and Technology*, vol. 23, no. 3, pp. 1 - 12, 2012.

[110] I. T. Joliffe, *Principal Component Analysis*, Springer, New York, 2nd Ed., 2002.

[111] L. N. Sharma, S. Dandapat, and A. Mahanta, "Multichannel ecg data compression based on multiscale principal component analysis," *IEEE Transactions on Information technology in Biomedicine*, vol. 16, no. 4, pp. 730 - 736, July 2012.

[112] F. M. Weber, D. U. J. Keller, M. S. Bauer, G. Seemann, C. Lorenz, and O. Dossel, "Predicting tissue conductivity influences on body surface potentials - an efficient approach based on principal component analysis," *IEEE Transactions on Biomedical Engineering*, vol. 58, no. 2, pp. 265 - 273, February 2011.

[113] S. Pyatykh, J. Hesser, and L. Zheng, "Image noise level estimation by principal component analysis," *IEEE Transactions on Image Processing*, vol. 22, no. 2, pp. 687 - 699, February 2013.

[114] P. C. Deng, W. H. Gu, and Y. F. Xie, "Latent space transformation based on principal component analysis for adaptive fault detection," *IEEE Transactions on seminconductor manufacturing*, vol. 23, no. 2, pp. 194 - 200, May 2010.

[115] R. M. L. Penha and J. W. Hines, "Using principal component analysis modeling to monitor temperature sensors in a nuclear research reactor," *Maintenance and Reliability Conference (MARCON)*, May 2001.

[116] N. Yadaiah and N. Reddy, "Statistical method for fault detection in synchronous generators," *International Conference on Computer Communication and Informatics (ICCCI)*, pp. 1 - 4, January 2012.

[117] S. C. Chan, H. C. Wu, and K. M. Tsui, "Robust recursive eigendecomposition and subspace-based algorithms with application to fault detection of wireless sensor networks," *IEEE Transactions on Instrumentation and Measurement*, vol. 61, no. 6, pp. 1703 - 1718, June 2012.

[118] J. E. Jackson, *A user's guide to principal components*, Wiley, New York, 1991.

[119] J. Mina and C. Verde, "Fault detection for large scale systems using dynamic principal components analysis with adaptation," *International Journal of Computers, Communications and Control*, vol. 2, no. 2, pp. 185-194, 2007.

[120] Q. He, X. He, and J. Zhu, "Fault detection of excavator's hydraulic system based on dynamic principal component analysis," *Journal of Central South University of Technology*, vol. 15, no. 5, pp. 700 - 705, October 2008.

[121] J. Mina and C. Verde, "Fault detection using dynamic principle component analysis by average estimation," *2nd International Conference on Electrical and Electronics Engineering (ICEEE) and XI Conference on Electrical Engineering*, pp. 374 - 377, September 2005.

[122] D. Garcia-Alvarez, M. J. Fuente, P. Vega, and G. Sainz, "Fault detection and diagnosis using multivariate statistical techniques in a wastewater treatment plant," *Advanced Control of Chemical Processes*, vol. 7, no. 1, pp. 952 - 957, 2009.

[123] J. P. George, Z. Chen, and P. Shaw, "Fault detection of drinking water treatment process using pca and hotelling's t2 chart," *World Academy of Science, Engineering and Technology*, vol. 3, no. 2, pp. 803 - 808, 2009.

[124] J. Jackson and G. Mudholkar, "Control procedures for residuals associated with principal component analysis," *Technometrics*, pp. 341 - 349, 1979.

[125] A. Khosravi, J. Melendez, M. Zapateiro, and J. Colomer, "Classification of voltage sags based on multiway principal component analysis and case based reasoning," *Proceedings of the 17th World Congress The International Federation of Automatic Control*, pp. 5529 - 5534, 2008.

[126] E. L. Russell, L. H. Chiang, and R. D. Braatz, "Fault detection in industrial processes using canonical variate analysis and dynamic principal component analysis," *Chemometrics and Intelligent Laboratory Systems*, vol. 51, pp. 81 - 93, 2000.

[127] J. M. Bernardo, "Bayesian statistics," *Encyclopedia of Life Support Systems, Probability and Statistics*, UNESCO, Oxford, United Kingdom, 2003.

[128] E. T. Jaynes, "The relation of bayeisan and maximum entropy methods," *Maximum entropy and Bayesian methods in Science and Engineering*, vol. 1, pp. 25 -29, 1988.

[129] A. Nissinen, L. M. Heikkinen, and J. P. Kaipio, "The bayesian approximation error approach for electrical impedance tomography - experimental results," *Measurement Science and Technology*, vol. 19, no. 1, pp. 1 - 9, 2008.

[130] Z. Lia, J. Zhua, X. Shena, C. Zhanga, and J. Guoa, "Fault diagnosis of motor bearing based on the bayesian network," *Procedia Engineering - International Workshop on Automobile, Power and Energy Engineering*, vol. 16, pp. 18 - 26, 2011.

[131] M. Muratovic, K. Sokolija, and M. Kapetanovic, "Modelling of high voltage sf6 circuit breaker reliability based on bayesian statistics," *IEEE GCC Conference and exhibition*, pp. 303 - 308, November 2013.

[132] D. C. Montgomery and G. C. Runger, *Applied statistics and probability for engineers*, John Wiley and Sons, New York, 3rd Ed., 2003.

[133] C. Scheffer and P. Girdhar, *Practical machinery vibration analysis and predictive maintenance*, Elsevier- Newnes, Oxford, United Kingdom, 2004.

[134] S. H. Yaghouti, S. S. Patankar, and J. V. Kulkarni, "Condition monitoring of rotary machinery using continuous wavelets," *IEEE International Confer-*

ence on Computational Intelligence and Computing Research (ICCIC), pp. 1 - 5, December 2012.

[135] A. Schuster, "On the investigation on hidden periodicities with application to a supposed 26-day period of meteorological phenomena," *Terrestrial Magnetism*, vol. 3, pp. 13 - 41, 1898.

[136] A. Quinquis, *Digital signal processing using MATLAB*, Hermes Science-Lavosier, France, 2007.

[137] M. H. Hayes, *Statistical digital signal processing and modeling*, John Wiley and Sons, Canada, 1996.

[138] P. M. Djuric and H. Li, "Bayesian estimation of harmonic signals," *IEEE Signal Processing Letters*, vol. 2, no. 11, pp. 213 - 215, November 1995.

[139] P. C. Gregory, "A bayesian revolution in spectral analysis," *AIP Conference Proceedings*, pp. 557 - 568, July 2000.

[140] N. Choudhuri, S. Ghosal, and A. Roy, "Bayesian estimation of the spectral density of a time series," *Theory and Method Journal of American Statistical Association*, vol. 99, no. 468, pp. 1050 - 1059, December 2004.

[141] G. L. Bretthorst, *Bayesian spectrum analysis and parameter estimation*, Springer-Verlag, 1988.

[142] C. Röver, R. Meyer, and N. Christensen, "Modeling colored residual noise in gravitational-wave signal processing," *Classical and Quantum Gravity*, vol. 28, no. 1, pp. 1- 20, 2011.

[143] H. Jeffreys, "An invariant form for the prior probability in estimation problems," *Proceedings of the Royal Society of London, Series A, Mathematical and Physical Sciences*, vol. 186, no. 1007, pp. 453 - 461, September 1946.

[144] C. Röver, "Bayesian spectral inference," R Package, 2008. Online: http://cran.r-project.org/package=bspec.

[145] F. van der Heijden, R. P. W. Duin, D. de Ridder, and D. M. J. Tax, *Classification, parameter estimation and state estimation*, John Wiley and Sons, 1st Ed., 2004.

[146] G. John and P. Langley, "Estimating continuous distributions in bayesian classifiers," *Proceedings of the Eleventh Conference on Uncertainty in Artificial Intelligence*, pp. 338 - 345, 1995.

[147] J. Wu, J. Cai, and X. Zhu, "Self-adaptive probability estimation for naive bayes classification," *IEEE International Joint Conference on Neural Networks*, pp. 1-8, 2013.

[148] M. Last, "The uncertainty principle of cross-validation," *IEEE International Conference on Granular Computing*, pp. 276 - 280, 2008.

[149] R. R. Bouckaert, E. Frank, M. Hall, R. Kirkby, P. Reutemann, A. Seewald, and D. Scuse, *WEKA Manual for Version 3-6-0*, University of Waikato, Hamilton, New Zealand, 2008.

[150] Y. Qi, T. P. Minka, and R. W. Picara, "Bayesian spectrum estimation of unevenly sampled nonstationary data," *IEEE International Conference on Acoustics, Speech and Signal Processing (ICASSP)*, vol. 2, pp. 1473 - 1476, 2002.

[151] dSpace GmbH, *Controldesk reference guide*, Release 6.5, 2009.

[152] M. Dunham, "Matlab weka interface," MATLAB source code, 2008. Online: http://www.mathworks.com/matlabcentral/fileexchange/21204-matlab-weka-interface.

Appendix A

Finite-Element Model

This Appendix presents the model for finite-element (FE) based analysis of the synchronous generator used in this thesis and consists of two sections. The first section presents basic information of the geometry, physics and mesh construction with Flux 2D. The second section describes the fault models and how the machine characteristics are evaluated.

A.1 Geometry and Physics

The synchronous 2-pole generator used in the presented research is designed to mimic large turbogenerators and is rated at $20\,kVA$, $3000\,rpm$, for an operational frequency of $50\,Hz$. This machine is equipped with a solid cylindrical rotor core, open stator slots, insulated bearings, and outboard static excitation (supplied from an external three phase rectifier). The geometrical parameters of the machine are given in table A.1 (below).

Table A.1: Geometrical parameters of the experimental synchronous generator

Parameter	Value	Unit
Number of rotor slots	32	-
Number of stator slots	48	-
Number of damper bars	38	-
Stator diameter - inner	190.5	mm
Stator diameter - outer	355.6	mm
Rotor diameter	178.5	mm
Shaft length	1290	mm
Shaft diameter	67	mm
Stator slot height	5.8	mm
Stator slot width	15	mm
Rotor slot height	5	mm
Rotor slot width	36	mm
Damper slot height	2.2	mm
Damper slot width	5	mm
Core length	280	mm

The geometrical parameters given in A.1 are used to construct the 2D geometry of the generator. A 2D implementation assumes that the rotor and stator are equal in length, and that the model is an adequate axisymmetrical slice along the length of the machine. However, a complete 2D 'slice' of the machine is modelled and radial symmetry is not assumed because the investigation requires evaluation of the electromagnetic fields and the shaft voltages resulting from asymmetrical characteristics. Each geometrical region - within the computation domain of the electromagnetic field - has dinstinct physical properties. Descriptions of the main regions follow:

- Stator case - Solid-conductor region representing the outer case of the machine. It is defined as a fixed steel region, comprising axially extending key ways.
- Stator core - Magnetic non-conducting region defined as a fixed part. This region is laminated steel, consisting of 48 slots.
- Rotor core - Solid-conductor region defined as a rotating part. This region is consists of 32 slots.
- Air-gap - Non-magnetic and non-conducting annular region between the stator core and the rotor core.
- Rotor and stator air gaps - Small non-magnetic and non-conducting annular regions between the air gap and slots.
- Stator Windings - Copper coil-conductor regions for the 3 phases. The phases are wye connected and consist of 2 parallel conductor groups of 24 turns.
- Rotor Windings - Copper coil-condutor regions for DC field windings. The rotor windings consists of negative and positive orientated conductors, positioned on either side of the rotor, with 10 turns per slot.
- Damper Bars - Solid copper-conductor regions distributed radially on the outer surface of the rotor core. There are 38 dampers in total.

The aforementioned regions of the machine model are illustrated in figure A.1 (below). Figure A.2 (below) illustrates the stator and rotor winding configurations.

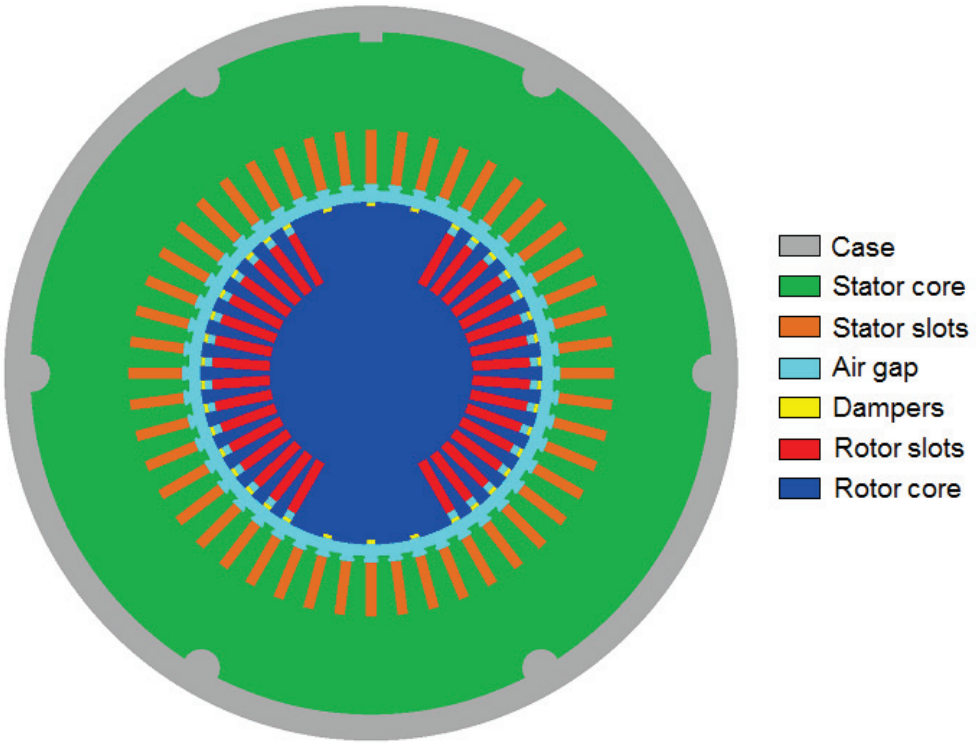


Figure A.1: FE model of synchronous generator indicating the different regions within the computation domain

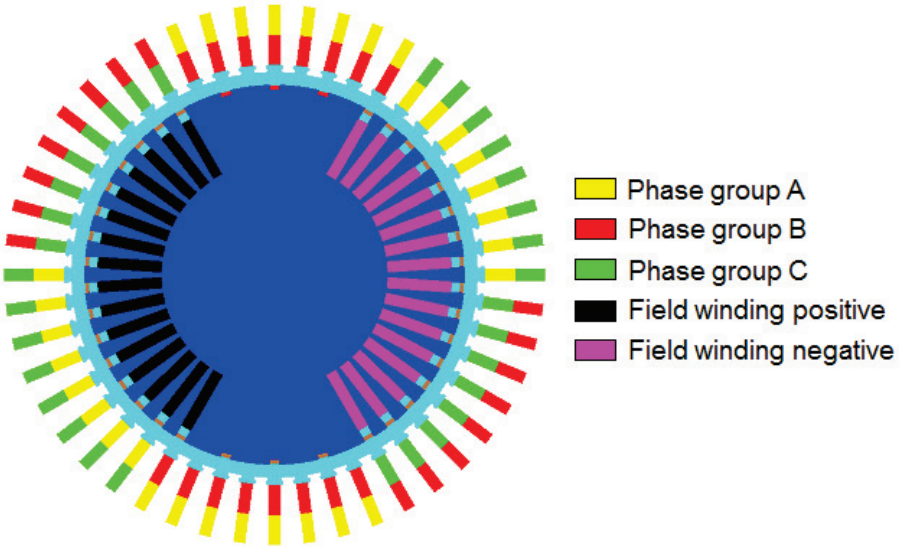


Figure A.2: FE model of synchronous generator, indicating only the winding regions

The FE model of the machine consists of a physics component which includes an external circuit model describing the interaction of the regions and external excitation (see figure A.3, below). The following components are used by the circuit model:

- Excitation - $V1$, $V2$ and $V3$ are AC voltage sources which supply the field windings via the three phase rectifier (diodes $D1 - D6$). These devices are external to the machine and are not directly associated with any region within the geometrical computation domain.

- Stator windings - A, B and C are coil elements representing the stator windings of the machine. These coil elements define the electrical interaction of the winding regions within the computation domain of the electromagnetic fields (shown in figure A.2).

- Load - $R1$, $R2$ and $R3$ model an external three-phase load to the synchronous generator. These elements are parameterised according to the investigation - e.g. open-circuited no-load or resistive load - and are not associated with any geometric region.

- Dampers - Solid conductor elements represent the damper bars of the machine, and are directly associated with the geometric region shown in figure A.1. The physical dampers on the machine do not directly interact with any electrical circuit of the machine such as the windings, but are included as circuit elements, as seen in A.3, to model the electrical characteristics - e.g. currents induced during operation.

- Rotor windings - $F1 - F6$ model the field windings of the machine. These elements are associated with the positive and negative field-winding regions, indicated in figure A.2. Multiple coil conductors are used for modelling faults on the machine - which is discussed in the following section. $C2$ represents the parasitic capacitance.

- Flux probe - $R1$, P and $C1$ model the flux probe fitted on the experimental synchronous generator - as described in Chapter 4. Coil element P consists of a single-turn conductor and is modelled as a small cross-sectional area, on

the stator-side of the air-gap, of the 2D geometry. This represents the actual conductor which runs along the length of the generator, on the inner surface of the stator.

- Stator case and rotor shaft - Mcs, Msh and Rsh model the solid conductor elements of the stator case and rotor shaft of the machine. Similarly to the dampers, these elements are not physically connected to any electrical components of the machine, but display electrical properties which must be modelled.

The stator and rotor cores of the machine are defined as magnetic regions - within the computation domain - with specific $B-H$ dependencies. This physical property is dependent on predefined materials used by the model. Non-oriented laminated electrical steel (with stacking factor of 0.95) is used for the stator and a non-laminated steel (machined from a solid bar) is used for the rotor core. In chapter 4, the $B-H$ values are varied to investigate the effects of uncertainty in the magnetic properties of these materials.

A.2 Fault Modelling and Solution

The outer boundary of the computation domain is defined as the outside of the stator case, which imposes a zero Dirichlet condition. As mentioned in chapter 3, the evaluation of the electromagnetic fields is based on the FE computation of the unknown magnetic vector potential. Prior to solving the model, a mesh of the computation domain is constructed (see figure A.4, below). A dense mesh, consisting of approximately 30900 nodes, minimises the FE model updating error. The geometry also contains smaller features - such as the air spaces at the slots, key way, weld recesses, and selected turns in the slots - which must be accounted (see figure A.5).

The two fault types investigated in this thesis are simulated using the FE model. Inter-turn short-circuited rotor windings are modelled through modifying the rotor winding region shown in figure A.2, and the coil conductors shown in figure A.3.

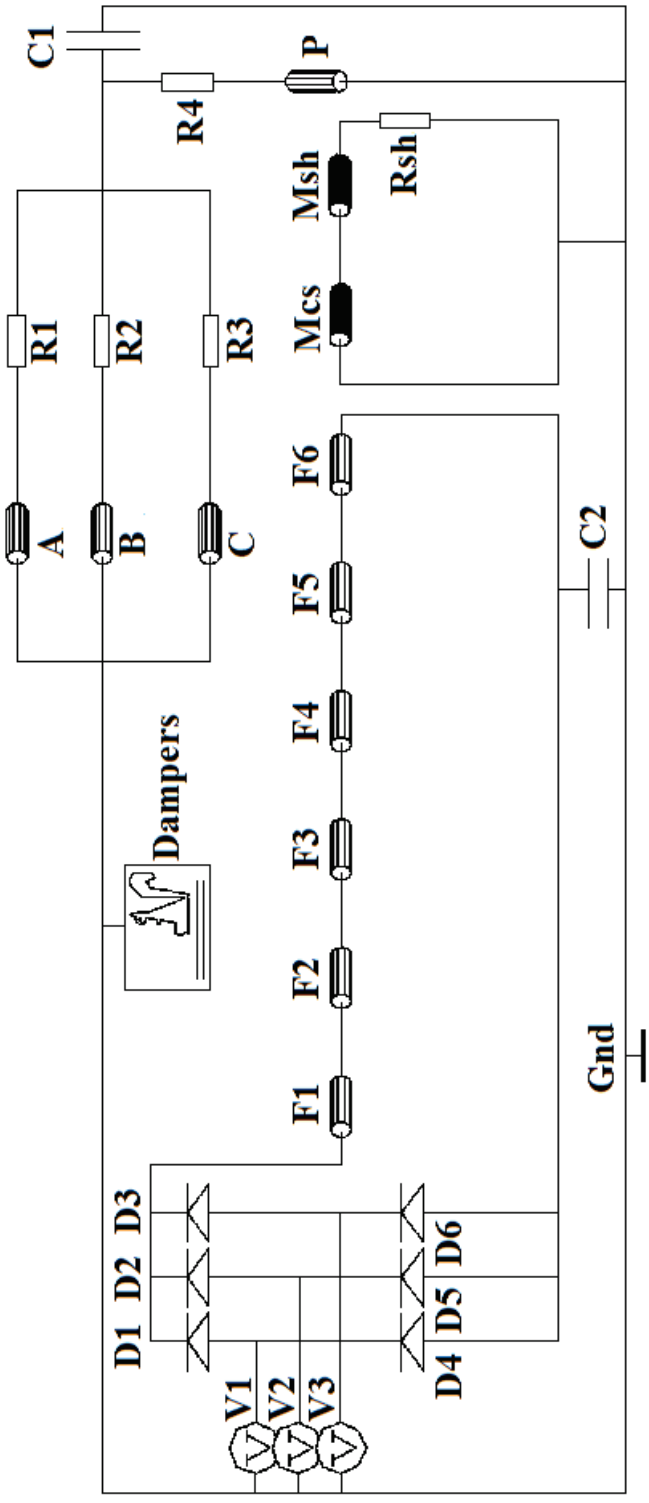


Figure A.3: Circuit model for the physics component of FE model and external devices of the synchronous generator

This is carried out by short-circuiting a rotor coil conductor corresponding to a specific turn in the winding region in the computation domain. For example, when coil element $F1$ is short-circuited in the circuit model, the associated elements on the geometry (as indicated by the differently coloured rotor-winding elements in figure A.4) will not have any current flow. Therefore, one short-circuited turn of the rotor winding will have a two associated elements in the geometry - i.e. one in the positive-winding region and another in the negative-winding region. Static eccentricity is carried out by manipulating the geometrical position of the rotor relative to the stator. For an eccentricity fault, the entire rotor geometry is shifted relative to the stator of the machine thus forming a new asymmetrical air gap. Furthermore, the presented research only models low levels of eccentricity (incipient faults), thus avoiding any possible overlapping the geometrical elements.

In chapter 3, the shaft voltage is described as the rate of change of the net flux over the path AB (refer to figure 3.4). An example of the output of the FE model, used to determine the shaft voltage, is given in figure A.6 (below). The figure shows the total flux along the stipulated path over time. Essentially, the distribution of the flux along the path is the same as shown in figure 3.5. The shaft voltage is obtained by integrating this distribution over time - i.e. total flux through loop "ABCD", described in chapter 3 of this thesis.

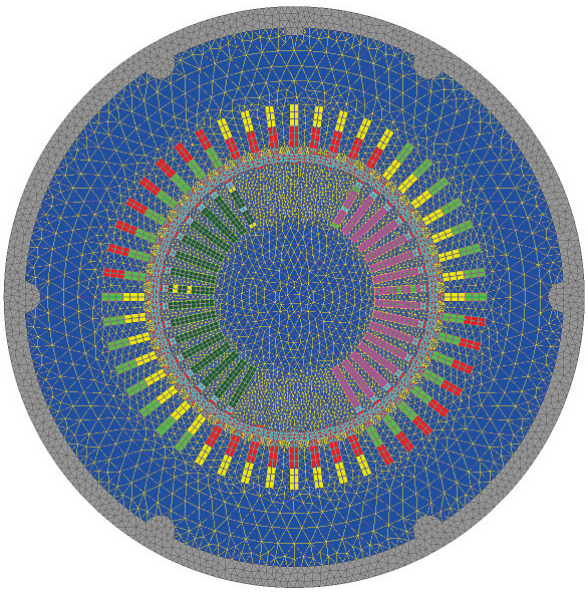


Figure A.4: Mesh of the computation domain of the FE model for the synchronous generator

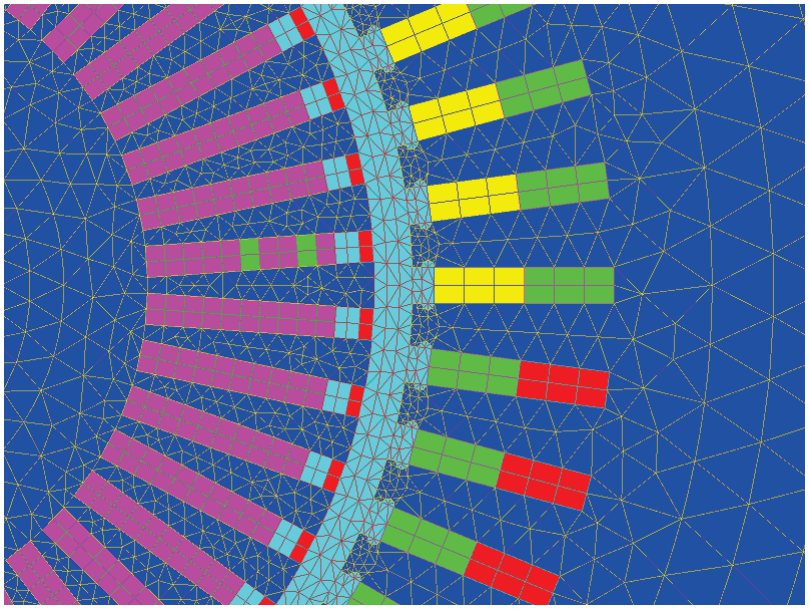


Figure A.5: Section of FE model geometry of synchronous generator with the mesh elements

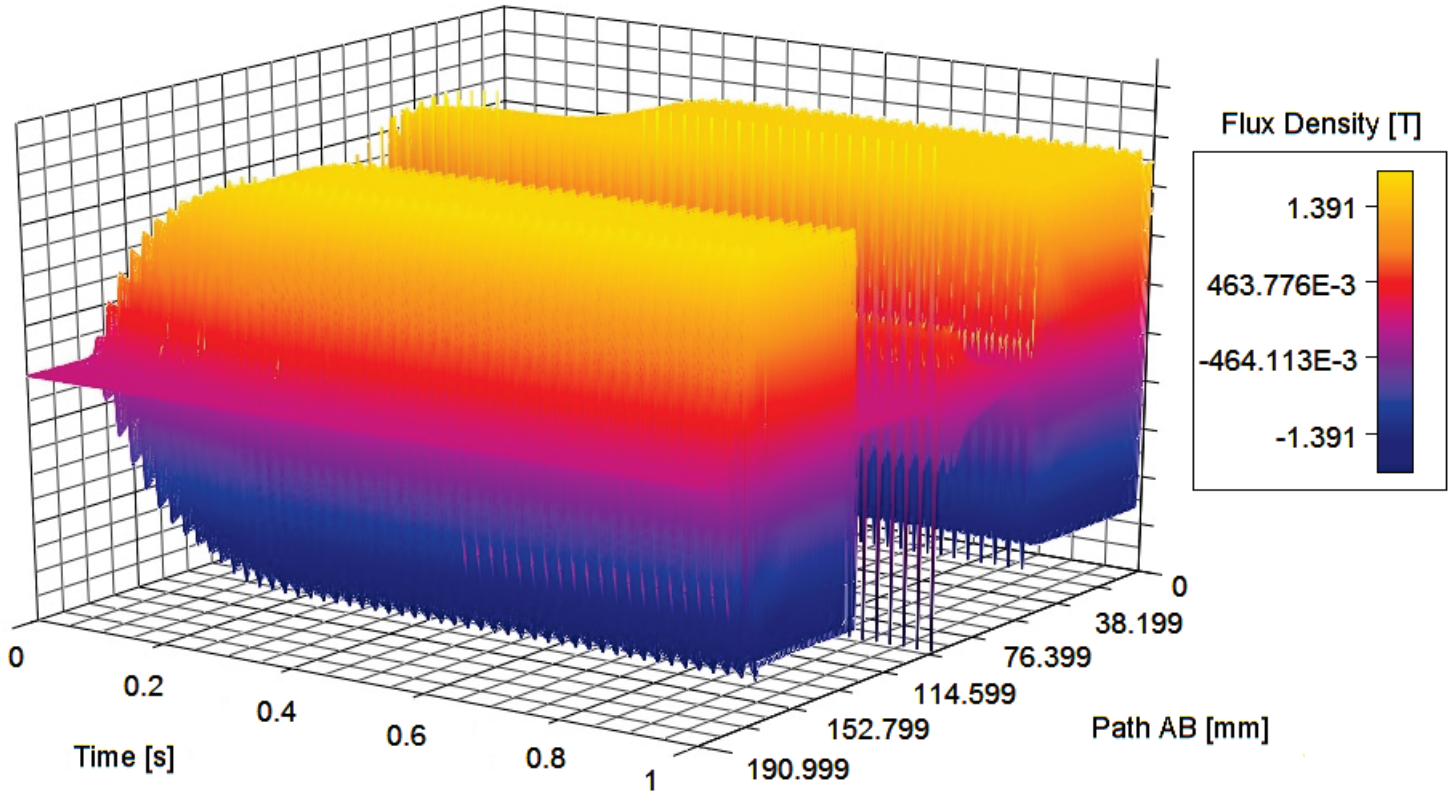


Figure A.6: Flux density along path AB of FE model of synchronous generator, under normal operating conditions, at different instances of time

Appendix B

Code listings

B.1 Fault Detection

The principle component analysis (PCA) algorithm - described in chapter 5 - is implemented in Matlab. Matlab directly interfaces with the dSpace measurement system [151], for online monitoring of the synchronous generator.

The following code is a function implementation of the fault-detection algorithm. This function receives online data through the main function and runs constantly. The presented code also includes an example of how faults are detected using offline data, obtained from measurements carried on the experimental synchronous generator with short-circuited rotor winding and eccentricity faults.

Listing B.1: Implementation of PCA fault detection algorithm as a Matlab function

```
1  function fault = PCA_compute_exp_NL_excludetrans()
2  %PCA on experimental (Without load)
3  clc;
4  clear all;
5  fault = false;
6  %read in No load no fault variables
7  load NL_NE_Rshaft_rms_e.mat;
8  load NL_WE_Rshaft_rms_e.mat;
9  load NL_WS_Rshaft_rms_e.mat;
10 load NL_NE_RAphase_rms_e.mat;
11 load NL_WE_RAphase_rms_e.mat;
12 load NL_WS_RAphase_rms_e.mat;
13 load NL_NE_RBphase_rms_e.mat;
14 load NL_WE_RBphase_rms_e.mat;
15 load NL_WS_RBphase_rms_e.mat;
16 load NL_NE_RCphase_rms_e.mat;
17 load NL_WE_RCphase_rms_e.mat;
18 load NL_WS_RCphase_rms_e.mat;
19 load NL_NE_If_rms_e.mat;
```

```
20 load NL_WE_If_rms_e.mat;
21 load NL_WS_If_rms_e.mat;
22 %read in No load no fault variables
23 [NL_NE_Rshaft] = NL_NE_Rshaft_rms_e';
24 [NL_NE_RAphase] = NL_NE_RAphase_rms_e';
25 [NL_NE_RBphase] = NL_NE_RBphase_rms_e';
26 [NL_NE_RCphase] = NL_NE_RCphase_rms_e';
27 [NL_NE_If] = NL_NE_If_rms_e';;
28 %read in No load eccentricity variables
29 [NL_WE_Rshaft] = NL_WE_Rshaft_rms_e';
30 [NL_WE_RAphase] = NL_WE_RAphase_rms_e';
31 [NL_WE_RBphase] = NL_WE_RBphase_rms_e';
32 [NL_WE_RCphase] = NL_WE_RCphase_rms_e';
33 [NL_WE_If] = NL_WE_If_rms_e';;
34 %read in No load with rotor short variables
35 [NL_WS_Rshaft] = NL_WS_Rshaft_rms_e';
36 [NL_WS_RAphase] = NL_WS_RAphase_rms_e';
37 [NL_WS_RBphase] = NL_WS_RBphase_rms_e';
38 [NL_WS_RCphase] = NL_WS_RCphase_rms_e';
39 [NL_WS_If] = NL_WS_If_rms_e';;
40  %compute moving average for Dynamic PCA (remove
       initial transients)
41  NE_SV = tsmovavg(NL_NE_Rshaft(600:980),'s',50,1)
42  NE_VA = tsmovavg(NL_NE_RAphase(600:980),'s',50,1)
43  NE_VB = tsmovavg(NL_NE_RBphase(600:980),'s',50,1)
44  NE_VC = tsmovavg(NL_NE_RCphase(600:980),'s',50,1)
45  NE_If = tsmovavg(NL_NE_If(600:980),'s',50,1)
46  %compute moving average for Dynamic PCA (remove
       initial transients)
47  WE_SV = tsmovavg(NL_WE_Rshaft(600:980),'s',50,1)
48  WE_VA = tsmovavg(NL_WE_RAphase(600:980),'s',50,1)
49  WE_VB = tsmovavg(NL_WE_RBphase(600:980),'s',50,1)
```

```
50  WE_VC = tsmovavg(NL_WE_RCphase(600:980),'s',50,1)
51  WE_If = tsmovavg(NL_WE_If(600:980),'s',50,1)
52  %compute moving average for Dynamic PCA (remove
        initial transients)
53  WS_SV = tsmovavg(NL_WS_Rshaft(600:980),'s',50,1)
54  WS_VA = tsmovavg(NL_WS_RAphase(600:980),'s',50,1)
55  WS_VB = tsmovavg(NL_WS_RBphase(600:980),'s',50,1)
56  WS_VC = tsmovavg(NL_WS_RCphase(600:980),'s',50,1)
57  WS_If = tsmovavg(NL_WS_If(600:980),'s',50,1)
58  %(exclude initial dead-zone)
59  X(:,1) = NE_SV(100:341)
60  X(:,2) = NE_VA(100:341)
61  X(:,3) = NE_VB(100:341)
62  X(:,4) = NE_VC(100:341)
63  X(:,5) = NE_If(100:341)
64  %(exclude initial dead-zone)
65  Y(:,1) = WE_SV(100:341)
66  Y(:,2) = WE_VA(100:341)
67  Y(:,3) = WE_VB(100:341)
68  Y(:,4) = WE_VC(100:341)
69  Y(:,5) = WE_If(100:341)
70  %(exclude initial dead-zone)
71  Z(:,1) = WS_SV(100:341)
72  Z(:,2) = WS_VA(100:341)
73  Z(:,3) = WS_VB(100:341)
74  Z(:,4) = WS_VC(100:341)
75  Z(:,5) = WS_If(100:341)
76  %zero mean and unit variance
77  X(:,1) = X(:,1) - mean(X(:,1));
78  X(:,2) = X(:,2) - mean(X(:,2));
79  X(:,3) = X(:,3) - mean(X(:,3));
80  X(:,4) = X(:,4) - mean(X(:,4));
```

```
81   X(:,5) = X(:,5) - mean(X(:,5));
82   X(:,1) = X(:,1)/std(X(:,1));
83   X(:,2) = X(:,2)/std(X(:,2));
84   X(:,3) = X(:,3)/std(X(:,3));
85   X(:,4) = X(:,4)/std(X(:,4));
86   X(:,5) = X(:,5)/std(X(:,5));
87    %zero mean and unit variance
88  Y(:,1) = Y(:,1) - mean(Y(:,1))
89  Y(:,2) = Y(:,2) - mean(Y(:,2))
90  Y(:,3) = Y(:,3) - mean(Y(:,3))
91  Y(:,4) = Y(:,4) - mean(Y(:,4))
92  Y(:,5) = Y(:,5) - mean(Y(:,5))
93  Y(:,1) = Y(:,1)/std(Y(:,1))
94  Y(:,2) = Y(:,2)/std(Y(:,2))
95  Y(:,3) = Y(:,3)/std(Y(:,3))
96  Y(:,4) = Y(:,4)/std(Y(:,4))
97  Y(:,5) = Y(:,5)/std(Y(:,5))
98   %zero mean and unit variance
99  Z(:,1) = Z(:,1) - mean(Z(:,1))
100 Z(:,2) = Z(:,2) - mean(Z(:,2))
101 Z(:,3) = Z(:,3) - mean(Z(:,3))
102 Z(:,4) = Z(:,4) - mean(Z(:,4))
103 Z(:,5) = Z(:,5) - mean(Z(:,5))
104 Z(:,1) = Z(:,1)/std(Z(:,1))
105 Z(:,2) = Z(:,2)/std(Z(:,2))
106 Z(:,3) = Z(:,3)/std(Z(:,3))
107 Z(:,4) = Z(:,4)/std(Z(:,4))
108 Z(:,5) = Z(:,5)/std(Z(:,5))
109 %Create PCAModel
110 [COEFF_NE,SCORE_NE,latent_NE,tsquare_NE] = princomp(
      X);
111 %Introduce eccentricity fault (exclude any
```

```
    insufficent time-lag data)
112 XY(1:length(X)+length(Y),1:5) = 0;
113 XY(1:length(X),:) = X(1:length(X),:);
114 XY(length(X)+1:length(X)+length(Y),:) = Y(1:length(Y
    ),:);
115 [COEFF_WE,SCORE_WE,latent_WE,tsquare_WE] = princomp(
    XY);
116 %Introduce rotor-short (exclude any insufficent time
    -lag data)
117 XZ(1:length(X)+length(Z),1:5) = 0;
118 XZ(1:length(X),:) = X(1:length(X),:);
119 XZ(length(X)+1:length(X)+length(Z),:) = Z(1:length(Z
    ),:);
120 [COEFF_WS,SCORE_WS,latent_WS,tsquare_WS] = princomp(
    XZ);
121 % Compute T squared with averages
122 tsquare_WE_final(1:length(tsquare_WE)-100) = 0;
123 tsquare_WE_final(1:length(tsquare_NE)-50) =
    tsquare_WE(51:length(tsquare_NE));
124 tsquare_WE_final(length(tsquare_NE)-50:length(
    tsquare_WE_final)) = tsquare_WE(length(tsquare_NE
    )+50:length(tsquare_WE));
125 mean_NE_T_1(1:length(tsquare_WE_final)) = mean(
    tsquare_WE_final(1:length(tsquare_NE)-50));
126 mean_WE_T(1:length(tsquare_WE_final)) = mean(
    tsquare_WE_final(length(tsquare_NE)-50:length(
    tsquare_WE_final)));
127 tsquare_WS_final(1:length(tsquare_WS)-100) = 0;
128 tsquare_WS_final(1:length(tsquare_NE)-50) =
    tsquare_WS(51:length(tsquare_NE));
129 tsquare_WS_final(length(tsquare_NE)-50:length(
    tsquare_WS_final)) = tsquare_WS(length(tsquare_NE
```

```
    )+50:length(tsquare_WS));
130 mean_NE_T_2(1:length(tsquare_WS_final)) = mean(
    tsquare_WS_final(1:length(tsquare_NE)-50));
131 mean_WS_T(1:length(tsquare_WS_final)) = mean(
    tsquare_WS_final(length(tsquare_NE)-50:length(
    tsquare_WS_final)));
132 %compute Q residuals with averages
133 ndim = 5;
134 residuals_NE = pcares(X,ndim);
135 residuals_WE = pcares(XY,ndim);
136 residuals_WS = pcares(XZ,ndim);
137 Q_NE = diag(residuals_NE*residuals_NE')
138 Q_WE = diag(residuals_WE*residuals_WE');
139 Q_WS = diag(residuals_WS*residuals_WS');
140 Q_WE_final(1:length(Q_WE)-100) = 0;
141 Q_WE_final(1:length(Q_NE)-50) = Q_WE(51:length(Q_NE)
    );
142 Q_WE_final(length(Q_NE)-50:length(Q_WE_final)) =
    Q_WE(length(Q_NE)+50:length(Q_WE));
143 mean_NE_Q_1(1:length(Q_WE_final)) = mean(Q_WE_final
    (1:length(Q_NE)-50));
144 mean_WE_Q(1:length(Q_WE_final)) = mean(Q_WE_final(
    length(Q_NE)-50:length(Q_WE_final)));
145 Q_WS_final(1:length(Q_WS)-100) = 0;
146 Q_WS_final(1:length(Q_NE)-50) = Q_WS(51:length(Q_NE)
    );
147 Q_WS_final(length(Q_NE)-50:length(Q_WS_final)) =
    Q_WS(length(Q_NE)+50:length(Q_WS));
148 mean_NE_Q_2(1:length(Q_WS_final)) = mean(Q_WS_final
    (1:length(Q_NE)-50));
149 mean_WS_Q(1:length(Q_WS_final)) = mean(Q_WS_final(
    length(Q_NE)-50:length(Q_WS_final)));
```

```
150 %plot New models with faults
151 plott =1;
152 if plott
153 figure;
154 plot(tsquare_WE_final,'g');
155 plot(tsquare_WS_final,'g');
156 hold on; grid on;
157 plot(mean_WE_T,'r')
158 plot(mean_NE_T_1,'k')
159 plot(mean_WS_T,'r')
160 plot(mean_NE_T_2,'k')
161 end
162 if plott
163 figure;
164 plot(Q_WE_final,'g');
165 plot(Q_WS_final,'g');
166 hold on; grid on;
167 plot(mean_WE_Q,'r')
168 plot(mean_NE_Q_1,'k')
169 plot(mean_WS_Q,'r')
170 plot(mean_NE_Q_2,'k')
171 end
172 %Output percentage change in T square and Q residual
      means
173 mean_NE_WE_T_change = 100*(mean_WE_T - mean_NE_T_1)/
      mean_NE_T_1
174 mean_NE_WS_T_change = 100*(mean_WS_T - mean_NE_T_2)/
      mean_NE_T_2
175 mean_NE_WE_Q_change = 100*(mean_WE_Q - mean_NE_Q_1)/
      mean_NE_Q_1
176 mean_NE_WS_Q_change = 100*(mean_WS_Q - mean_NE_Q_2)/
      mean_NE_Q_2
```

```
177  If (mean_NE_WE_T_change >= 20) && (
         mean_NE_WE_Q_change >= 20)
178        fault = True;
179  end
180  end
```

B.2 Fault Diagnosis

Once a fault has been detected by the PCA routine the fault diagnosis algorithm, described in chapter 6, is called. The fault diagnosis routine consists of two main components. The first component extracts the features from the shaft-voltage signal using the Bayesian spectrum-estimation routine. Secondly, the Bayesian classifier is used to diagnose the fault.

The following code listings show function implementations of the fault-diagnosis algorithm. The Bayesian spectrum-estimation routine is implemented using the programming lanaguage R, and the Bayesian classifier consists of a Java-implemented Weka core [149] - which is a set of open source machine-learning algorithms. However, all routines are managed using the Matlab platform, which enabes online exchange with the dSpace measurement system. In order to utilise the Weka Naive-Bayes core in Matlab, the interfacing method described in [152], is modified and implemented as given below. The Bayesian spectrum estimation routine uses a function called 'Bspec'. This function is part of a spectrum-estimation package [144] - with details of the implementation are given in [142].

B.2.1 Bayesian Spectrum Estimation and Feature Extraction

Listing B.2: Matlab function for scripting of Bayesian spectrum-estimation function in an R run-time environment

```
1  function Rscript()
```

```
2  %Calls Rscript from Matlab to perform Bayesian
       Spectrum Analysis on data and return results for
       fault diagnosis
3  % Load recorded data for offline usage (Load
       directly from dSpace monitoring system when
       online)
4  load Data.mat
5  transx= Data;
6  % Save the variable to an R formatted data file
7  saveR('Data.R','transx')
8  % Get the current directory and switch slashes (R
       file pathes require '\')
9  CurrentDirectory=strrep(pwd,'\','/');
10 % Run script in R
11 eval(['!C:\PROGRA~1\R\R-3.0.2\bin\x64\Rscript.exe␣
       Command.R'])
12 % Load the results from R
13 load('SpecResults.mat')
14 end
```

Listing B.3: Matlab function for saving an instance created in an R run-time environment

```
1  function saveR(filename, varargin)
2  %Saves workspace variables to an R data file.
3  if(nargin < 1), error('Requires␣at␣least␣one␣input␣
       arguments.'); end
4  if(nargin < 2),
5       vars = evalin('caller', 'who');
6  else
7       vars = varargin;
8  end
9  fid = fopen(filename,'wt');
```

```
10 for var_index = 1:length(vars),
11     var_name = vars{var_index};
12     var_namestr = ['"' var_name '" <-'];
13     var_value = evalin('caller', vars{var_index});
14     var_size = size(var_value);
15     var_sizestr = mat2str(var_size(:));
16     var_sizestr = strrep(var_sizestr(2:end-1),';',',
           ');
17     if(isstruct(var_value))
18         warning('SAVER:structure','R cannot handle
               structures. File "%s" will be written but
               will not contain variable "%s".',
               filename,var_name);
19         continue;
20     elseif(iscell(var_value)),
21         var_valuestr = sprintf('"%s", ',var_value
               {:});
22         var_valuestr = ['structure(c(' var_valuestr
               (1:end-2) '), .Dim = c(' var_sizestr '))'
               ];
23     elseif(isscalar(var_value)),
24         var_valuestr = num2str(var_value);
25         var_valuestr = strrep(var_valuestr,'NaN','NA
               ');
26     else
27         var_valuestr = mat2str(var_value(:));
28         var_valuestr = strrep(var_valuestr,'NaN','NA
               ');
29         var_valuestr = ['structure(c(' strrep(
               var_valuestr(2:end-1),';',', ') '), .Dim
               = c(' var_sizestr '))'];
30     end
```

```
31        fprintf(fid, '%s\n%s\n', var_namestr,
              var_valuestr);
32    end
33    fclose(fid);
34    end
```

Listing B.4: Function executed in R run-time environment - when called by Matlab script - to carry out Bayesian spectrum-estimation

```
1  #Bayesian Spectrum Function call using RScripting
2  #Load required R.matlab package
3  library(R.matlab)
4  library(bspec)
5  #Load data saved from Matlab
6  source('..Rscripting/saveR/Data.R')
7  #Run one sample t test and save results
8  SVTS <- as.ts(transx, 0, 2, deltat = 0.001)
9  #Estimate Bayesian Spectrum
10 bspecSV <-bspec(SVTS)
11 y <- bspecSV$freq
12 z <- bspecSV$scale
13 #Save results to Matlab data file
14 writeMat('Rscripting/saveR/SpecResults.mat',z=z,y=y)
```

Listing B.5: Bayesian spectrum-estimation function of the Bspec package

```
1  bspec.default <- function(x, priorscale=1, priordf
       =0,
2                            intercept=TRUE, two.sided=
                                 FALSE, ...)
3  # x                  : time series object (uni- or
       multivariate)
```

```
4  # priorscale, priordf : a vector or a function of
       frequency
5  # intercept           : flag indicating whether to
       include zero frequency
6  # two.sided           : flag indicating whether to
       refer to one- or two-sided spectrum.
7  #                       only effect within _this_
       function is interpretation of prior scale.
8  #                       Note that the 'two.sided'
       flag is "inherited" by other functions
9  #                       via their default arguments.
        See e.g. 'expectation.bspec()'.
10 {
11   # some initial checks:
12   if (is.vector(x) | (is.ts(x) & !is.mts(x)))
13     N <- length(x)
14   else if (is.mts(x) | is.matrix(x) | is.data.frame(
       x))
15     N <- nrow(x)
16   else warning("incompatible argument 'x'")
17   FTlength <- (N %/% 2) + 1   # size of (
       nonredundant) FT output
18   Neven <- ((N %% 2) == 0)    # indicator for even N
19   stopifnot(is.function(priorscale) ||
20             ((length(priorscale)==1) |
21             (intercept & (length(priorscale)==
                 FTlength)) |
22             ((!intercept) & (length(priorscale)==(
                 FTlength-1)))))
23   stopifnot(is.function(priordf) ||
24             ((length(priordf)==1) |
```

```
25              (intercept & (length(priordf)==FTlength)
                    ) |
26              ((!intercept) & (length(priordf)==(
                    FTlength-1)))))
27    stopifnot(is.function(priorscale) || (all(is.
          finite(priorscale)) & all(priorscale>0)),
28              is.function(priordf) || (all(is.finite(
                    priordf)) & all(priordf>=0)))
29    if (!is.ts(x)) {
30      x <- as.ts(x)
31      warning("argument 'x' is not a time-series
            object, default conversion 'as.ts(x)' applied
            .")
32    }
33    deltat <- 1 / tsp(x)[3]
34    deltaf <- 1 / (N*deltat)
35    t0 <- tsp(x)[1]             # time stamp
          corresponding to 1st observation
36    kappa <- c(0, rep(1,FTlength-2), ifelse(Neven,0,1)
          )
37    # 1-D case:
38    if (!is.mts(x)) {
39      # Fourier transform:
40      y <- fft(as.vector(x))
41      # ('fft()' yields unnormalised FT)
42      nonredundant <- 1:FTlength
43      # vector of (N/2 + 1) cosine coefficients:
44      a <- (1+kappa) * sqrt(deltat/N) * Re(y[
            nonredundant])
45      # vector of (N/2 + 1) sine coefficients:
46      b <- -(1+kappa) * sqrt(deltat/N) * Im(y[
            nonredundant])
```

```
47      datassq <- a^2 + b^2
48      datadf <- c(1, rep(2,FTlength-2), ifelse(Neven
            ,1,2))
49    }
50    # multidimensional case:
51    else {
52      # Fourier transform:
53      #y <- apply(x, 2, fft)
54      y <- mvfft(x)
55      # ('fft()' yields unnormalised FT)
56      nonredundant <- 1:FTlength
57      # vector of (N/2 + 1) cosine coefficients:
58      a <- sqrt(deltat/N) * Re(y[nonredundant,])
59      for (i in 1:ncol(a)) a[,i] <- (1+kappa)*a[,i]
60      # vector of (N/2 + 1) sine coefficients:
61      b <- -sqrt(deltat/N) * Im(y[nonredundant,])
62      for (i in 1:ncol(b)) b[,i] <- (1+kappa)*b[,i]
63      datassq <- apply(a^2 + b^2, 1, sum)
64      datadf <- c(1, rep(2,FTlength-2), ifelse(Neven
            ,1,2)) * ncol(x)
65    }
66    # vector of corresponding frequencies:
67    freq <- (0:(FTlength-1)) * deltaf

69    # set up a-priori scale:
70    if (is.function(priorscale))
71      priorscalevec <- priorscale(freq)
72    else if (length(priorscale)==1)
73      priorscalevec <- rep(priorscale, FTlength)
74    else if (!intercept)
75      priorscalevec <- c(0, priorscale)
76    else priorscalevec <- priorscale
```

```
77    if (two.sided){
78      # /!\ different interpretation of prior scale
            /!\
79      priorscalevec <- priorscalevec * (1+kappa)
80    }

82    # set up a-priori degrees-of-freedom:
83    if (is.function(priordf))
84      priordfvec <- priordf(freq)
85    if (length(priordf)==1)
86      priordfvec <- rep(priordf, FTlength)
87    else if (!intercept)
88      priordfvec <- c(0, priordf)
89    else priordfvec <- priordf

91    #arg <- seq(from=tsp(x)[1], to=tsp(x)[2], le=500)
92    #trigo <- arg*0
93    #for (i in 1:length(a))
94    # trigo<-trigo+(a[i]*cos(2*pi*freq[i]*(arg-t0)) +
          b[i]*sin(2*pi*freq[i]*(arg-t0)))
95    #trigo <- trigo / sqrt(N*deltat)
96    #plot(x,type="b")
97    #lines(arg, trigo, col="red")

99    if (! intercept) {
100     freq <- freq[-1]
101     priorscalevec <- priorscalevec[-1]
102     priordfvec <- priordfvec[-1]
103     datassq <- datassq[-1]
104     datadf <- datadf[-1]
105     kappa <- kappa[-1]
106   }
```

```
108     # determine posterior distribution's parameters:
109     # (posterior distn. of 1-sided spectrum S_1(f_j)
            == sigmasquared_j!)
110     # --> S_2(f_j) = sigmasquared_j / (1+kappa(j))
              = S_1(f_j) / (1+kappa(j))
111     scale <- (priordfvec*priorscalevec + datassq) / (
            priordfvec + datadf)
112     df <- datadf + priordfvec

114     result <- list(freq = freq,
115                    scale = scale,
116                    df = df,
117                    priorscale = priorscalevec,
118                    priordf = priordfvec,
119                    datassq = datassq,
120                    datadf = datadf,
121                    N = N, deltat = deltat, deltaf =
                           deltaf,
122                    start = t0,
123                    call = match.call(expand.dots=FALSE
                           ),
124                    two.sided = two.sided)
125     class(result) <- "bspec"
126     return(result)
127 }
```

Listing B.6: Matlab function used to extract harmonics from Bayesian spectrum estimate for use as features in the classifier

```
1 Function harmonic = Extract()
2 %Function for extraction of shaft signal harmonics
      from Bayesian spectrum
```

```
3  clc;
4  clear all;
5  %load Bayesian spectrum estimate
6  load Data_res.mat;
7  %scale imported posterior distribution
8  f = freq*1000
9  Pyyy = scale;
10 j=0;k=1;
11 temp = [0 0 0 0 0 0 0 0 0 0];
12 harmonic = [0 0 0 0 0 0 0 0 0 0];
13 %search through posterior distribution
14 while ((k>=1) & (k<=251))
15 % extract maximum in vincinity of interesting
       harmonics
16      while ((f(k) >= 46) & (f(k) <=54))
17              k = k+1;
18              j = j + 1;
19              temp(j) = Pyyy(k)
20              harmonic(1) = max(temp)
21      end;
22      while ((f(k) >= 96) & (f(k) <= 104))
23               k = k+1;
24              j = j + 1;
25              temp(j) = Pyyy(k)
26              harmonic(2) = max(temp)
27      end;
28      while ((f(k) >= 146) & (f(k) <= 154))
29               k = k+1;
30              j = j + 1;
31              temp(j) = Pyyy(k)
32                   harmonic(3) = max(temp)
33      end;
```

```
34      while ((f(k) >= 196) & (f(k) <= 204))
35                k = k+1;
36              j = j + 1;
37              temp(j) = Pyyy(k)
38                  harmonic(4) = max(temp)
39      end;
40      while ((f(k) >= 246) & (f(k) <= 254))
41                k = k+1;
42              j = j + 1;
43              temp(j) = Pyyy(k)
44                  harmonic(5) = max(temp)
45      end;
46      while ((f(k) >= 296) & (f(k) <= 304))
47                k = k+1;
48              j = j + 1;
49              temp(j) = Pyyy(k)
50                  harmonic(6) = max(temp)
51      end;
52      while ((f(k) >= 346) & (f(k) <= 354))
53                k = k+1;
54              j = j + 1;
55              temp(j) = Pyyy(k)
56                  harmonic(7) = max(temp)
57      end;
58      while ((f(k) >= 396) & (f(k) <= 404))
59                k = k+1;
60              j = j + 1;
61              temp(j) = Pyyy(k)
62                  harmonic(8) = max(temp)
63      end;
64      while ((f(k) >= 446) & (f(k) <= 454))
65                k = k+1;
```

```
66                  j = j + 1;
67                  temp(j) = Pyyy(k)
68                       harmonic(9) = max(temp)
69        end;
70        while ((f(k) >= 496) & (f(k) < 500))
71                  k = k+1;
72                  j = j + 1;
73                  temp(j) = Pyyy(k)
74                  harmonic(10) = max(temp)
75        end;
76        k = k+1;
77        temp(:) = 0,j=0;
78  end;
79  end
```

B.2.2 Fault Classification

Listing B.7: Validates the Java class path

```
1  function bool = validate()
2  %Validates Java path
3       bool = true;
4       check = strfind(javaclasspath('-all'),'weka.jar'
            );
5       if(isempty([check{:}]))
6            bool = false;
7            errordlg('Invalid␣java␣class␣path');
8            help validate;
9       end
10 end
```

Listing B.8: Saves Java object to a data file

```
1  function save_instfile(filename,W_Obj)
2  %Saves Java object to data file
3   if(~validate)
4           W_obj = [];
5           return
6   end
7       import weka.core.converters.ArffSaver; %Import
            weka converters
8       import java.io.File;
9       saver = ArffSaver();
10      saver.setInstances(W_Obj);
11      saver.setFile(File(filename));
12      saver.writeBatch();
13 end
```

Listing B.9: Loads data from file, into a Java object, for use by the classifier

```
1  function W_Obj = load_instfile(filename)
2  %Loads data into a Java object
3       if(~validate)
4           W_obj = [];
5           return
6       end
7       import weka.core.converters.ArffLoader; %Import
            weka converters
8       import java.io.File;
9       loader = ArffLoader();
10      loader.setFile(File(filename));
11      W_Obj = loader.getDataSet();
12      W_Obj.setClassIndex(W_Obj.numAttributes - 1);
13 end
```

Listing B.10: Converts the input data to Java instances

```
1  function W_obj = convert_to_w(title,feature,data,
       index)
2  %Converts data to Java Instances object for
       classification
3   if(~validate)
4           W_obj = [];
5           return
6   end
7       if(nargin < 4)
8           index = numel(feature);
9       end
10      import weka.core.*; %import Java Weka core
11      vec = FastVector();
12      if(iscell(data))
13          for i=1:numel(feature)
14              if(ischar(data{1,i}))
15                  attvals = unique(data(:,i));
16                  values = FastVector();
17                  for j=1:numel(attvals)
18                      values.addElement(attvals{j});
19                  end
20                  vec.addElement(Attribute(feature{i},
                        values));
21              else
22                  vec.addElement(Attribute(feature{i})
                        );
23              end
24          end
25      else
26          for i=1:numel(feature)
```

```
27                  vec.addElement(Attribute(feature{i}));
28              end
29          end
30          W_Obj = Instances(title,vec,size(data,1));
31          if(iscell(data))
32              for i=1:size(data,1)
33                  inst = Instance(numel(feature));
34                  for j=0:numel(feature) - 1
35                      inst.setDataset(W_Obj);
36                      inst.setValue(j,data{i,j+1});
37                  end
38                  W_Obj.add(inst);
39              end
40          else
41              for i=1:size(data,1)
42                  W_Obj.add(Instance(1,data(i,:)));
43              end
44          end
45          W_Obj.setClassindex(index - 1);
46      end
```

Listing B.11: Converts Java instances output from classifier, to a data file

```
1   function [cache,feature,index,optstring,namestr] =
        convert_to_m(W_obj,optcache)
2   %Converts Java instances to data
3    if(~validate)
4              W_obj = [];
5              return
6          end
7   if(nargin < 2)
8          optcache = [];
```

```
 9 end
10 if(not(isjava(W_obj)))
11     fprintf('Requires a java weka object as input.')
           ;
12     return;
13 end
14 cache = zeros(W_obj.numInstances,W_obj.numAttributes
       );
15 for i=0:W_obj.numInstances-1
16     cache(i+1,:) = (W_obj.instance(i).toDoubleArray)
           ';
17 end
18 index = W_obj.classIndex + 1;
19 feature = cell(1,W_obj.numAttributes);
20 optstring = cell(1,W_obj.numAttributes);
21 for i=0:W_obj.numAttributes-1
22     feature{1,i+1} = char(W_obj.attribute(i).name);
23     attribute = W_obj.attribute(i);
24     nvals = attribute.numValues;
25     vals = cell(nvals,1);
26     for j=0:nvals-1
27         vals{j+1,1} = char(attribute.value(j));
28     end
29     optstring{1,i+1} = vals;
30 end
31 namestr = char(W_obj.relationName);
32 if(iscell(optcache))
33    celldata = num2cell(cache);
34    for i=1:numel(optstring)
35       vals = optstring{1,i};
36       if(not(isempty(vals)))
37          celldata(:,i) = vals(cache(:,i)+1)';
```

```
38          end
39      end
40      cache = celldata;
41  end
42  end
```

Listing B.12: Trains the classifier

```
1  function Classifier = train(data,type,classifier_opt
       )
2  % Trains the classifier
3   if(~validate)
4           W_obj = [];
5           return
6   end
7       Classifier = javaObject(['weka.classifiers.',
            type]); %Create weka classifier object
8       if(nargin == 3 && ~isempty(classifier_opt))
9           Classifier.setclassifier_opt(classifier_opt)
                ;
10      end
11      Classifier.buildClassifier(data);
12  end
```

Listing B.13: Classifies the new instances, then returns the predictions and probability distributions

```
1  function [prediction, probcalcs] = classify(
       test_data,classifier)
2  %Returns matrix of predicted classes and probability
       distributions of test instances
3  if(~validate)
```

```
4           W_obj = [];
5           return
6  end
7  for t=0:test_data.numInstances - 1
8          probcalcs(t+1,:) = (classifier.
               distributionForInstance(test_data.instance
               (t)))';
9      end
10     [prob,prediction] = max(probcalcs,[],2);
11     prediction = prediction - 1;
12 end
```

Listing B.14: Calls and passes instances to training and/or classifier functions, and outputs fault diagnosis

```
1  Function diagnosis = Test()
2  %Function to train Bayesian classifier using
       simulated data
3  %Function to test Bayesian classifier using
       simulated data
4  javaaddpath ('C:\Program␣Files␣(x86)\weka-3-6-10\
       weka-3-6-10\weka.jar');
5  diagnosis = 'Nothing␣diagnosed!';
6  %Trains the classfier (Done at start-up only or by
       user)
7  Train_data = load_instfile('
       Bayes_train_WEWS_new_exp_nl.arff');
8  Classifier_WEWS = train(Train_data,'bayes.
       NaiveBayesSimple');
9  %Classifies the current instance of the shaft
       voltage
10 Test_data = load_instfile('
       Bayes_test_WEWS_new_exp_nl.arff');
```

```
11 [predictedClass_test, classProbs_test] = classify(
       Test_data,Classifier_WEWS);
12 %Simple return of machine status
13 if predictedClass_test == 1
14     diagnosis = 'Healthy';          %Added security
           against false alarm
15 end
16 if predictedClass_test == 2
17     diagnosis = 'Eccentricity';
18 end
19 if predictedClass_test == 3
20     diagnosis = 'Rotor short';
21 end
22 end
```

B.2.3 Classifier Training Example and Output

The following code is an example of the format used to train the Naive-Bayes classifier. Thereafter, an example output of a trained classifier is listed. It should be noted that the test instances are formatted the same as the training examples - with the exception of the unknown class label.

Listing B.15: Example of the training format for the classifier, using experimental data without a load

```
1 @relation faultharmonic
2 @attribute first real
3 @attribute second real
4 @attribute third real
5 @attribute fourth real
6 @attribute fifth real
7 @attribute sixth real
8 @attribute seventh real
9 @attribute eighth real
```

```
10 @attribute ninth real
11 @attribute tenth real
12 @attribute fault {HEALTHY,ECCENTRICITY,ROTOR_SHORT}
13 @data
14 6.2548,0.017768,0.075349,0.055791,
       1.1384,0.045357,1.9662,0.015236,0.74545,0.00029078,
       HEALTHY
15 6.5309,0.016534,0.07292,0.051881,
       1.0989,0.039723,1.9298,0.016411,0.75776,0.00031138,
       HEALTHY
16 6.1943,0.018021,0.07601,0.057163,
       1.175,0.044911,1.8571,0.01369,0.7281,0.00027961,
       HEALTHY
17 6.2667,0.016947,0.076421,0.056017,
       1.1688,0.039288,1.8168,0.01556,0.7364,0.00032095,
       HEALTHY
18 6.4754,0.018305,0.074612,0.054175,
       1.1576,0.04129,1.9495,0.016247,0.75039,0.00029426,
       HEALTHY
19 6.1451,0.017112,0.077412,0.059602,
       1.2464,0.04399,1.9704,0.017033,0.77917,0.0002844,
       HEALTHY
20 6.2149,0.017935,0.077133,0.053647,
       1.269,0.047002,1.9958,0.018704,0.78345,0.00030273,
       HEALTHY
21 6.3275,0.041729,0.09853,0.01483,
       1.7661,1.6096,1.2526,0.10048,0.81312,0.020398,
       ECCENTRICITY
22 6.4177,0.039675,0.10511,0.01237,
       1.7352,1.599,1.3001,0.10189,0.82012,0.021007,
       ECCENTRICITY
```

```
23 6.1025,0.041922,0.09636,0.015711,
       1.7708,1.6414,1.1976,0.10955,0.81801,0.019991,
       ECCENTRICITY
24 6.6332,0.039924,0.098566,0.016076,
       1.7767,1.6863,1.2491,0.10211,0.8511,0.020865,
       ECCENTRICITY
25 6.7011,0.04206,0.095434,0.012506,
       1.7801,1.6095,1.1226,0.10665,0.84162,0.020944,
       ECCENTRICITY
26 4.8991,0.027791,0.98852,0.025825,
       1.3466,0.076144,1.552,0.02141,0.37992,0.0021064,
       ROTOR_SHORT
27 4.7903,0.025113,0.99027,0.024991,
       1.4191,0.080131,1.3398,0.023,0.35988,0.002099,
       ROTOR_SHORT
28 4.9294,0.029844,0.95911,0.027351,
       1.3108,0.07699,1.7014,0.02008,0.39221,0.002259,
       ROTOR_SHORT
29 4.5949,0.029087,0.98048,0.027078,
       1.5869,0.07567,1.7836,0.021079,0.35402,0.002339,
       ROTOR_SHORT
30 4.8003,0.02709,0.9767,0.028377,
       1.2998,0.071426,1.348,0.020079,0.37146,0.0019985,
       ROTOR_SHORT
```

Listing B.16: Example of an output from trained classifier

```
1 Naive Bayes Classifier
2                          Class
3 Attribute              HEALTHY ECCENTRICITY
      ROTOR_SHORT
```

```
4                              (0.4)          (0.3)
                                  (0.3)
5  ═══════════════════════════════════════════════════

6  first
7    mean                      6.3186         6.4239
         4.7653
8    std. dev.                 0.1407         0.2265
         0.0985
9    weight sum                   7              5
                    5
10   precision                 0.1316         0.1316
         0.1316
11 second
12   mean                      0.0173         0.0408
         0.0278
13   std. dev.                 0.0006         0.0008
         0.0016
14   weight sum                   7              5
                    5
15   precision                 0.0016         0.0016
         0.0016
16 third
17   mean                      0.0573         0.1147
         0.9747
18   std. dev.                 0.0096         0.0096
         0.0096
19   weight sum                   7              5
                    5
20   precision                 0.0573         0.0573
         0.0573
21 fourth
```

```
22    mean                0.0552        0.0136
          0.0266
23    std. dev.           0.0021        0.0014
          0.0019
24    weight sum             7             5
                    5
25    precision           0.003         0.003
          0.003
26  fifth
27    mean                1.1799        1.7711
          1.3965
28    std. dev.           0.0544        0.0209
          0.0948
29    weight sum             7             5
                    5
30    precision           0.0426        0.0426
          0.0426
31  sixth
32    mean                   0          1.647
          0.1029
33    std. dev.           0.0172        0.0172
          0.0172
34    weight sum             7             5
                    5
35    precision           0.1029        0.1029
          0.1029
36  seventh
37    mean                1.9257        1.2334
          1.5499
38    std. dev.           0.0697        0.0557
          0.1746
```

```
39    weight sum                7             5
                  5
40    precision            0.0546        0.0546
          0.0546
41  eighth
42    mean                 0.0171        0.1042
          0.0216
43    std. dev.            0.0021        0.0029
          0.0029
44    weight sum                7             5
                  5
45    precision             0.006         0.006
          0.006
46  ninth
47    mean                 0.7501        0.8202
          0.3728
48    std. dev.            0.0198        0.0152
          0.0196
49    weight sum                7             5
                  5
50    precision            0.0311        0.0311
          0.0311
51  tenth
52    mean                       0        0.0205
          0.0026
53    std. dev.            0.0002        0.0005
          0.0002
54    weight sum                7             5
                  5
55    precision            0.0013        0.0013
          0.0013
```

B.3 Main Function for Online Monitoring

The main function is converted into a Simulink block to directly interface with the dSpace ADC input block. The input block enables online communication with dSpace interface card and the experimental synchronous generator board. The main code is a simple list of calls to fault-detection and fault-diagnosis functions.

Listing B.17: Main function

```
1  function status = main(shaft_voltage)
2  %Main function continuous called for online
       monitoring
3  % Accepts input from dSpace ADC input block in
       simulink
4  status = 'No problem detected';
5  fault = PCA_compute(shaft_voltage); %Call PCA fault
       detection function
6  if (fault)          %Check if PCA detected an issue
7       status = 'Problem detected';
8  %If there is a fault detection, call Bayesian fault
       diagnosis functions
9       Rscript();      % Bayesian spectrum estimation
10      harmonic = Extract();      % Harmonic feature
            extraction
11      diagnosis = Test(harmonic);
12      errdlg(diagnosis);          % Throw out a dialog of
             the fault
13 end
```